Spring 2014

3D Aerodynamic Optimization of NREL VI Wind Turbine Blade for Increased Power Output and Visualization of Flow Characteristics

Tsewang Rabga Shrestha
Embry-Riddle Aeronautical University - Daytona Beach

3D AERODYNAMIC OPTIMIZATION OF NREL VI WIND TURBINE BLADE FOR INCREASED POWER OUTPUT AND VISUALIZATION OF FLOW CHARACTERISTICS

By

Tsewang Rabga Shrestha

A Thesis Submitted to the College of Engineering, Department of Aerospace Engineering

for the partial fulfillment of the requirements of the degree of

Master of Science in Aerospace Engineering

Embry-Riddle Aeronautical University

Daytona Beach, Florida

Spring 2014

3D AERODYNAMIC OPTIMIZATION OF NREL VI WIND TURBINE BLADE FOR INCREASED POWER OUTPUT AND VISUALIZATION OF FLOW CHARACTERISTICS

By

Tsewang Rabga Shrestha

This thesis was prepared under the direction of the candidate's Thesis Committee Chair, Dr. Sathya Gangadharan, Professor, Daytona Beach Campus, and Thesis Committee Members Dr. William Engblom, Professor, Daytona Beach Campus, and Dr. R. Mankbadi, Professor, Daytona Beach Campus, and has been approved by the Thesis Committee. It was submitted to the Department of Aerospace Engineering in partial fulfillment of the requirements for the degree of Master of Science in Aerospace Engineering.

Thesis Review Committee:

Dr. Sathya Gangadharan
Committee Chair

Dr. Reda Mankbadi
Committee Member

Dr. William Engblom
Committee Member

Dr. Yi Zhao
Graduate Program Chair

Dr. Robert Oxley
Associate Vice President of Academics

4-24-2014

Date

Date

Acknowledgement

I would like to thank Dr. Sathya Gangadharan for his advice and guidance thorough the thesis work. It has been a long and challenging task, and I deeply appreciate his guidance and patience.

On the same note, I would like to express my gratitude to Dr. Reda Mankbadi and Dr. William Engblom, for taking time off their busy schedule to serve as committee members. Their suggestions and help, provided more insight to the work for which I am really grateful.

Abstract

Author	Tsewang Rabga Shrestha
Title	3D Aerodynamic Optimization of NREL VI Wind Turbine Blade for Increased Power Output and Visualization of Flow Characteristics
Institution	Embry-Riddle Aeronautical University
Degree	Master of Science in Aerospace Engineering
Year	2014

The thesis focuses on the aspect of optimization of NREL VI wind turbine blade for increased power output using commercial solver ANSYS 14.5. The power curve obtained from BEMT, Baseline NREL VI CFD Simulations and Optimized Blade Simulations are compared with experimental results. Over prediction is observed in the theoretical result while computational analysis under predicts power produced at post stall region. Parameter correlation and sensitivity analysis study relates the effectiveness of design parameters on the objective outcome. Scatter plots and Determination Matrix indicate the problem setup as non-linear quadratic. Adaptive Single Objective Optimization algorithm is used for the optimization process where an intelligent auto refinement of domain spaces searches for a global optimum. Large domain reduction and limited evaluation space due to computational burden restricts the finding of global optimum but 5 best local optimum results are still yielded. Flow visualization and characteristic study display attached flow through the blade span till 7 m/s wind speed. Flow separation at 10 m/s and above is well captured by the boundary layer and pressure coefficient plots agree well with the transition location.

Contents

List of Figures

List of Tables

Nomenclature

a	axial induction factor
a’	angular induction factor
B	number of blades
c	chord length
c_l	lift coefficient
c_d	drag coefficient
C_p	power coefficient
D	drag
F_x	axial force
F_Θ	tangential force
L	Lift
N	number of blade elements
p	pressure
P	power
Q	tip loss correction factor
r	radial direction and radius
R	blade radius at tip

T	torque
V	absolute velocity
W	relative velocity
X	axial coordinate
β	relative flow angle toward blade
λ	tip speed ratio
λ_r	local tip speed ratio
σ'	blade solidity
ρ	density
Ω	angular velocity

1. Introduction

The difference in the atmospheric pressure from solar radiation, due to differential heating of the poles and equator causes the movement of air from a high pressure zone to a low pressure zone, commonly termed as wind. Only a small part of the solar radiation (2% approximately) is responsible for the flow of air.

For generations, wind has been utilized for various purposes ranging from transportation to harnessing electricity. Wind turbine generators are responsible for extracting kinetic energy from the wind to electrical energy with aid of the generators. Wind turbine blade can only extract a limited amount of kinetic energy from the fluid stream and not all of it. Extracting it would mean a decrease in the fluid velocity and the fluid velocity cannot reach zero, because the fluid should continue to flow. Since the fluid flow is subsonic, and turbine blade acts as an obstruction to the flow, not all of the flow passes through the rotating turbine blade, some pass around it. Thus, contributing to reduced energy extraction.

Wind turbines are classified generally into two type, lift type and drag type. Most common lift type wind turbine is the horizontal axis wind turbine shortly abbreviated as HWAT. Drag type wind turbine generally constitute the Vertical Axis Wind Turbine (VAWT). Some new lift type wind turbines also fall under the VAWT.

HAWT have higher efficiency than VAWT and is commonly used in large scale production of electricity in land or offshore in an array forming a wind farm. Increase in energy demand, has shifted the focus of many government to rely on renewable sources of energy rather than depending on the fossil fuels. As such, the rotor diameter of HWAT

increased from 10 m from the past few decades to well over 75 m successfully implemented for power generation and research are being conducted for over 100m blade span. Thus arises the question, How optimized is the blade for aerodynamic performance? How much of computing time does it take for convergence to an optimum design? Could the design variable be optimized in the BEMT phase? , etc.

Optimization involves defining the geometry of the specimen to satisfy certain objective requirements when subjected to some constraints. Aerodynamic optimization conducted generally describe the optimum angle of attack required for maximum lift coefficient and minimum drag coefficient for a wide range of flow velocity in 2D case. While, structural optimization manipulates the object dimensions within a set constraint to maximize product life, minimize von misses stresses around a specified factor of safety.

Traditional method of optimization for engineering design process represents a reverse design procedure, because of the reverse nature of most engineering calculation method. Aerodynamic performance is calculated from prescribed geometric shape that is often changed in a trial and error manner. Another method is the inverse design method where the optimum geometric shape is determined from a prescribed target distribution of some aerodynamic quantity. The ultimate goal is a direct design process, where the design space is searched for the optimum design in an automatic and systematic way. This allows design that is beyond the experience and intuition of the designer, thus allowing technological jumps and the initiation of new concepts. The use of numerical optimization facilitates direct design methods. The change in geometry is systematized so that the objective is fulfilled to the requirement of specified constraints.

Regarding aerodynamics the necessity of optimization is clear, given even very small improvements in the performance can yield large reductions in operating costs, lowering of undesirable environmental pollution, shorten travel times, improve payload capacity and improve performance. Renewable energy source are currently dependent on Wind Generators and research and manufacture of blade with longer span is conducted, any improvements regarding aerodynamic aspects achieved during the design and development stage are rewarded with larger gains.

1.1 Objectives

The aim is to achieve an optimum design of NREL VI blade geometry to increase power output at a prescribed wind speed. Such that the methodology could be applied to other 3D aerodynamic optimization.

- Provide c_l and c_d results of S 809
- Predict theoretical power from Blade Element Momentum Theory
- Perform mathematical optimization on BEMT
- Validate original model and simulation configuration with experimental results
- Conduct correlation study between pairs of design input variable and its influence on the output function
- Optimize blade geometry using Adaptive Single Objective algorithm to search for a global optimum or a local optimum
- Analyze optimum blade for varying wind speed
- Compare the optimum results with theoretical and experimental results

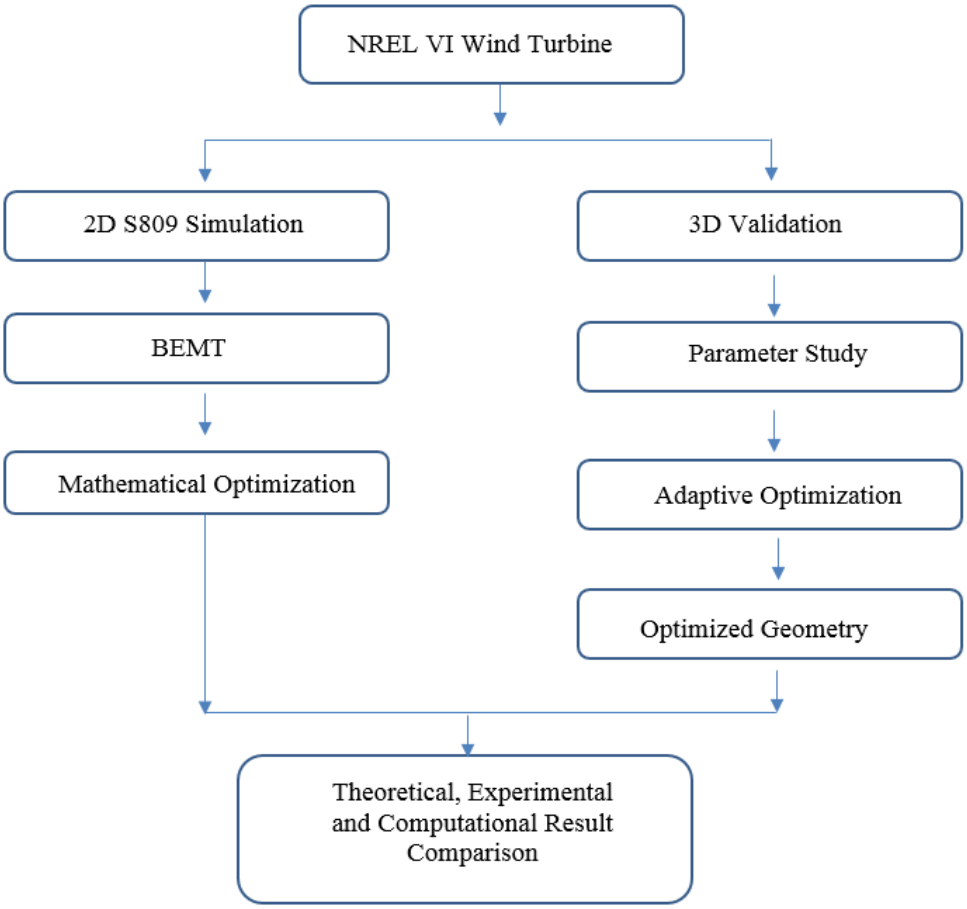

Figure 1: Objective Road Map

2. National Renewable Energy Laboratory

NREL VI wind turbine blade uses the S809 airfoil section exclusively. The blade design was optimized on the annual energy capture subject to the design constraints imposed for the instrumentation. The blade chord at 90% span was specified to be 0.457m to correspond to the constant chord blades tested in Phases I – V. Extensive study and data trade off with previous blade model resulted in a linear taper and a nonlinear twist distribution using the S809 from root to tip.

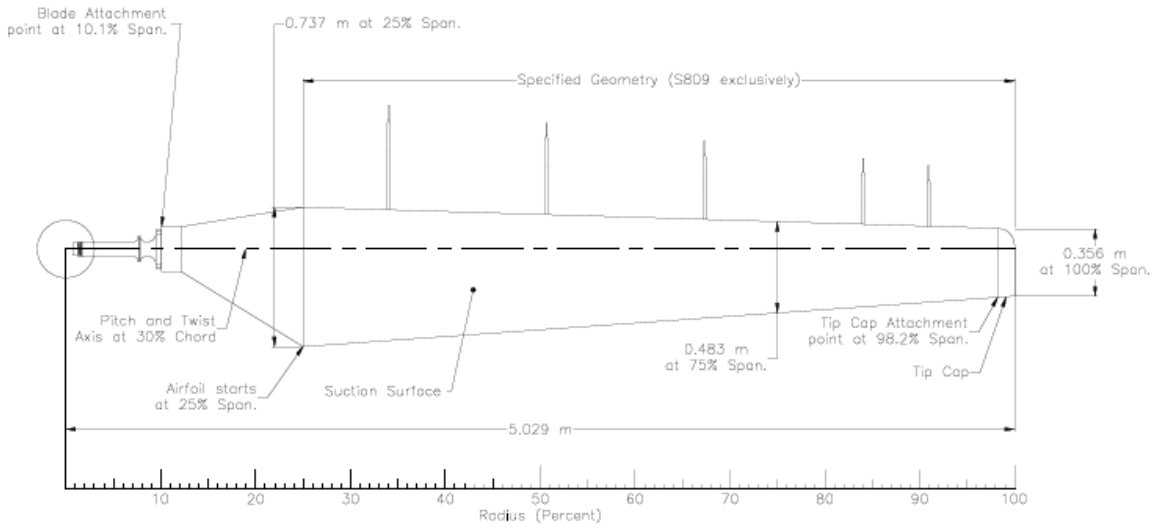

Figure 2: NREL VI Plan Form View

The characteristic of the turbine blade are stated below:

- The rotor diameter is 11 m.
- The turbine is 2 bladed (unlike conventional 3 blades).
- The blades have a linear taper with maximum chord of 0.737 m at 25% span and 0.356 m at 100% span.

- The blades have a nonlinear twist of 22.5 degree over the blade span.
- S809 airfoil used over the entire span.
- Rated rotor speed is 72 rpm.

Table 1: Chord and Twist Distribution

Radial Distance (m)	Span Station r/5.532	Span Station r/5.029	Chord (m)	Twist (degrees)
0	0	0	Hub	Hub
0.508	0.092	0.101	0.218	0
0.660	0.120	0.131	0.218	0
0.883	0.160	0.176	0.183	0
1.008	0.183	0.200	0.349	6.7
1.067	0.193	0.212	0.441	9.9
1.133	0.205	0.225	0.544	13.4
1.257	0.227	0.250	0.737	20.040
1.343	0.243	0.267	0.728	18.074
1.510	0.273	0.300	0.711	14.292
1.648	0.298	0.328	0.697	11.909
1.952	0.353	0.388	0.666	7.979
2.257	0.408	0.449	0.636	5.308
2.343	0.424	0.466	0.627	4.715
2.562	0.463	0.509	0.605	3.425
2.867	0.518	0.570	0.574	2.083
3.172	0.573	0.631	0.543	1.150

3.185	0.576	0.633	0.542	1.115
3.476	0.628	0.691	0.512	0.494
3.781	0.683	0.752	0.482	-0.015
4.023	0.727	0.800	0.457	-0.381
4.086	0.739	0.812	0.451	-0.475
4.391	0.794	0.873	0.420	-0.920
4.696	0.849	0.934	0.389	-1.352
4.780	0.864	0.950	0.381	-1.469
5.00	0.904	0.994	0.358	-1.775
5.305	0.959	1.055	0.328	-2.191
5.532	1.000	1.100	0.305	-2.500

2.1 Airfoil Characteristics

The main component of a wind driven generator is its wind turbine blade, which in turn depend on the characteristic shape of its airfoil. An airfoil, is a geometrical shape which utilizes the fluid flow over its surfaces to generate a favorable lift to drag ratio, as per the function requirement.

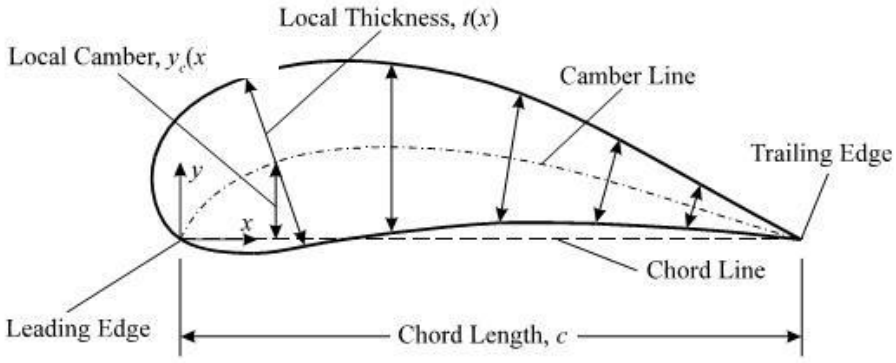

Figure 3: Airfoil Cross Section & Nomenclature

Over the decades, many HAWTs have employed the NACA series airfoil, but due to the deteriorate functionality of the leading edge and lack of sufficient thickness around quarter chord to allow spar strength to withstand load distribution, the dependency of airfoil shape has inclined towards the NREL developed wind turbine specific shapes.

A collaboration between National Renewable Energy Laboratory (NREL) and Airfoils Inc. in 1984 lead to the development of series of airfoils for wind turbine generators with aid of Eppler Airfoil Design and Analysis. These airfoil series met the requirement of stall regulation, variable pitch and rpm of wind turbine generators. The 25 airfoils so designed were represented with range from S801 to S828, and were segregated into root, primary and tip airfoil sections. Except for the root airfoil all others were designed to achieve maximum coefficient of lift with insensitiveness to roughness effect with direct proportion to the moment coefficient.

2.2 S809 Wind Turbine Airfoil

S809 airfoil was designed in 1986 for HAWT application, and was experimentally tested against NACA design airfoils. The theoretical design and analysis of the airfoil was experimentally verified in the low turbulence wind turbine of Delft University of Technology Low Speed Laboratory, in Netherlands. The objective of a restrained maximum lift, insensitive to roughness and low profile drag were achieved and also exhibited docile stall. Eppler Design tool was implemented in the design of the airfoil.

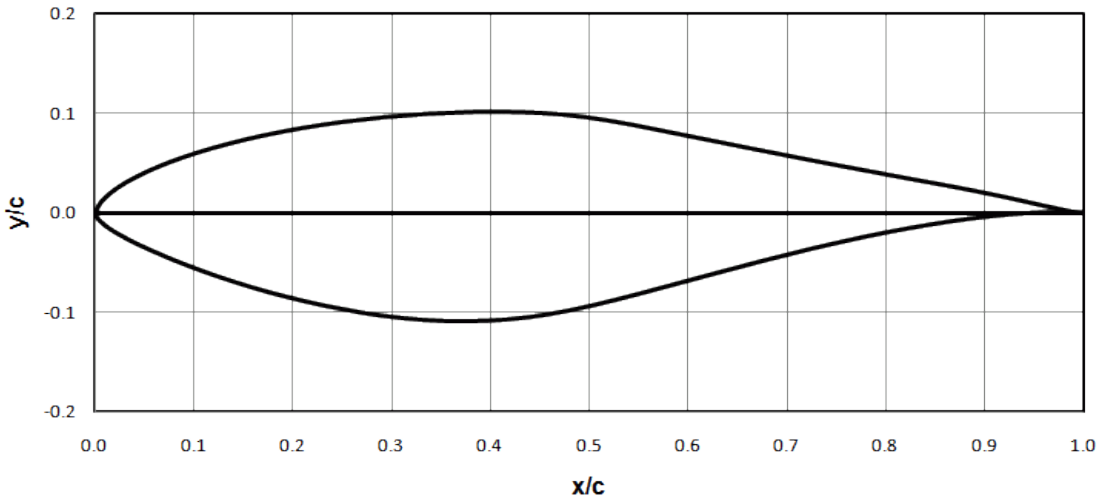

Figure 4: S809 Airfoil

Specifications:

Thickness: 21%

Maximum lift coefficient: 1.01

Design lift coefficient: 0.5

Zero lift pitching moment coefficient- > -0.05

Reynolds number: 2×10^6

3. Computational Analysis – S809

3.1 Computational Domain

The C Grid boundary is sketched using the 2 point curve and curve command tab in POINTWISE. The semicircle boundary is sketched at a radius of 12.5 times the chord length of the airfoil with the tip of leading edge as the center and the posterior border is set to 20 times the chord length from the tip of trailing edge of the airfoil. The upper and lower boundary of the C Grid is measured to be at 12.5 times the chord from the chord line, as seen in Figure 1.

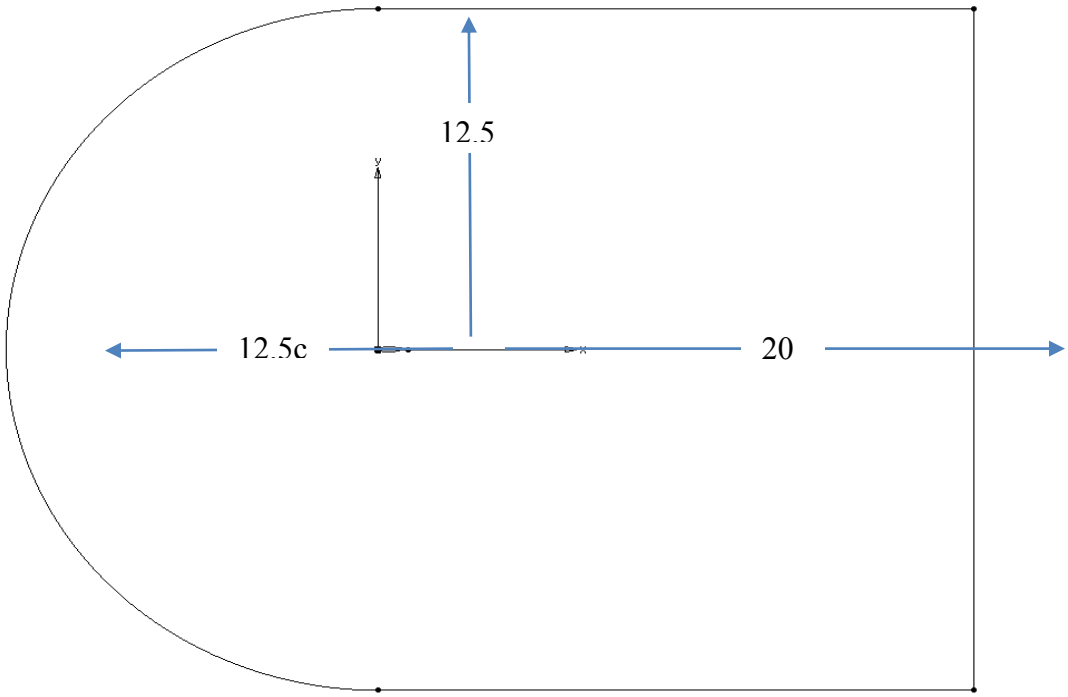

Figure 5: C - Grid Enclosure

The enclosure is a wireframe which must be set prior to meshing the domain. The domain set up for 2D analysis is a hybrid domain i.e., composed of both structured and unstructured mesh. The structured mesh is created using the "Extrude- Normal" tab, after selecting the airfoil surface. The orientation is set as plane under "Attributes", if the direction vector is outward normal to airfoil surface, no flipping is necessary. For smooth transition between elements, a growth rate of 1.1 is specified with 75 run steps, allowing sufficient layer thickness to capture flow separation. The remaining domain space is then meshed with unstructured grid; to avoid overlapping of mesh, the domain is created via "Assemble Special- Domain" tab, instead of direct domain tool. Inner and outer domain should have reversed edge direction to subtract the structured domain from consideration, thus eliminating the need to perform Boolean operation later.

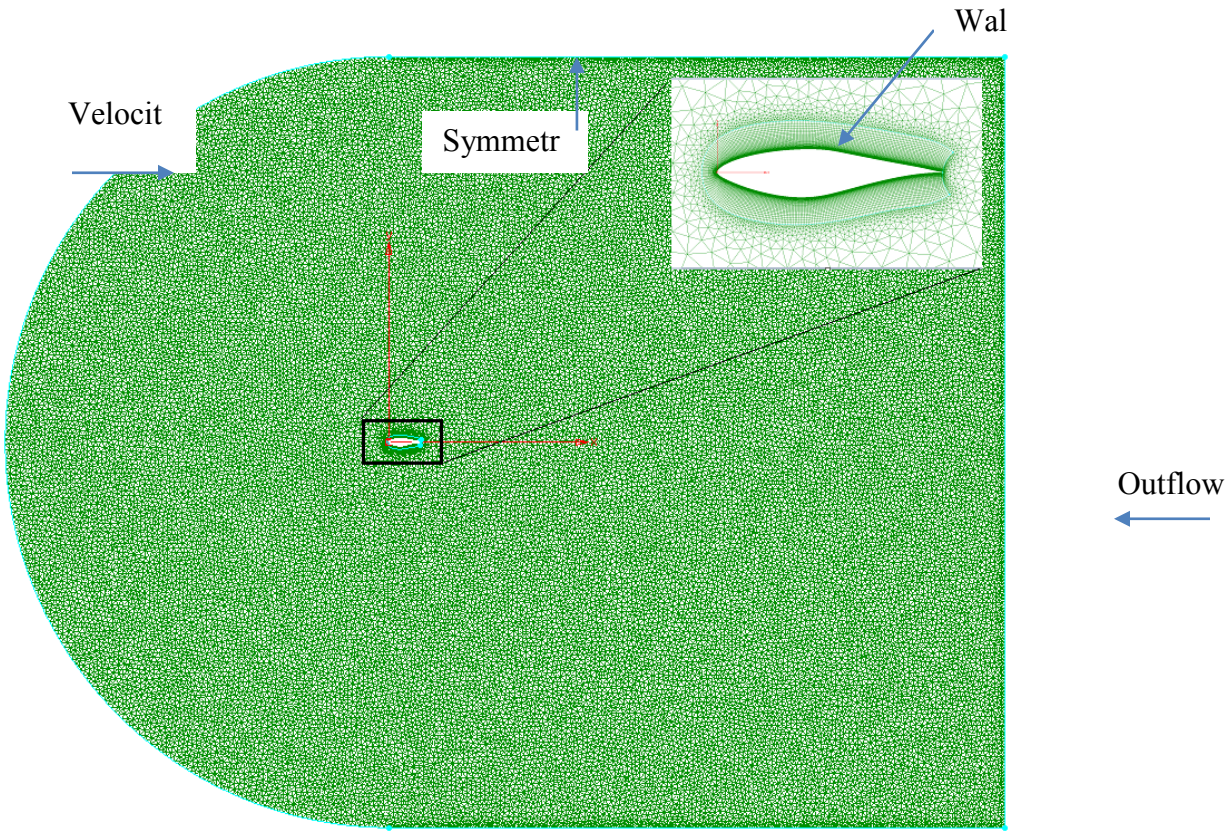

Figure 6: Hybrid Mesh and Boundary Conditions

3.2 Boundary Setup:

Fluid domain boundary conditions can be preset in POINTWISE itself, eliminating the need to redefine in FLUENT solver. Under the "CAE" tab in POINTWISE, select the solver to be used. Since the mesh is generated on a 2D plane, the solver is also selected for 2D. The "Set Boundary Conditions" tab highlights the unspecified boundary. The semicircle edge is set as "Velocity Inlet", upper and lower edge of C Grid is set as "Symmetry" and the edge opposite the semicircle as "Outflow". The upper and lower surfaces of the airfoil are termed as "Wall", as shown in Fig. 2.

Statistics:

- Structured Mesh
    - Points - 299 x 76
    - Cell – 22,350
    - Growth Rate – 1.1
    - Step – 75

- Unstructured Mesh
    - Points – 38,067
    - Cell - 74,689

- Connector Dimension
    - C Grid Enclosure – 4 x 250
    - Upper airfoil – 150
    - Lower airfoil – 150

3.3 FLUENT Simulation

The mesh setup from POINTWISE is imported into FLUENT as .cas file, with the boundary conditions predefined. The system properties are set to "Double Precision" to ensure adequate accuracy, since good solutions are needed. Before starting a simulation in FLUENT, the mesh has to be scaled, as different dimension measurement were used in POINTWISE, and checked for quality. Not every mesh created in different software is readily accepted by FLUENT. Build errors are often displayed in FLUENT which needs rectification. The mesh quality and errors can be easily rectified by running the FLUENT "mesh/repair-improve/repair" command. Occasionally, additional command may be required to further refine the mesh. After mesh improvement, the desired operating conditions and parameters can be defined. These parameters include compressibility, viscosity, turbulence model, steady state or transient flows, etc. The max iteration count is then set, and if lift coefficient and drag coefficient seems to have stabilized properly, then the interactions can be stopped to save computing time or wait for the solution to converge completely.

The "Check Case" tab in the run calculation window checks the mesh set up again, to ensure corrective set up of the simulation to be conducted. The following values are set:

- Number of interval = 1000
- Reporting Interval = 1
- Profile Update Interval = 1

A steady state, in viscid simulation with default convergence criteria does not require large number of intervals, since the solution converges rather quickly. Post processing of the results conducted in FLUENT saves time.

3.3 Results and Discussion

Present results depict the lift coefficient changing with the angle of attack. The computational results show the trend line of lift coefficient similar to experimental results. The simulation underestimated the lift coefficient by marginal error from 1.02 degrees to 13.24 degrees. However, the lift was severely over predicted at 0 degrees. The flow field around the airfoil responsible for build of forces acting on the airfoil has been presented by the pressure and the velocity contours in Table 2. The computational analysis of the flow over airfoil of a simplified section gave relatively good agreement with the experiments.

Table 2: Coefficient of Lift

a.o.a	Experimental	Inviscid	Error %
	cl	cl	
-0.01	0.143	0.2140	-49.6503
1.02	0.264	0.2810	-6.43939
2.05	0.386	0.3513	8.989637
3.08	0.507	0.4260	15.97633
4.1	0.627	0.5100	18.66029
5.13	0.742	0.6338	14.58221
6.16	0.82	0.7450	9.146341

7.17	0.892	0.7630	14.46188
9.22	1.013	0.9130	9.871668
10.21	1.004	0.8605	14.29482
11.21	0.975	0.9240	5.230769
12.22	1.008	0.9733	3.44246
13.24	1.052	1.0340	1.711027
14.24	1.081	1.0833	-0.21277
15.24	1.097	1.1340	-3.37284
16.24	1.061	1.1600	-9.33082
17.23	0.999	1.0350	-3.6036

Table 3: Velocity and Pressure Contours

a.o.a	Pressure Contours	Velocity Contours
1.02	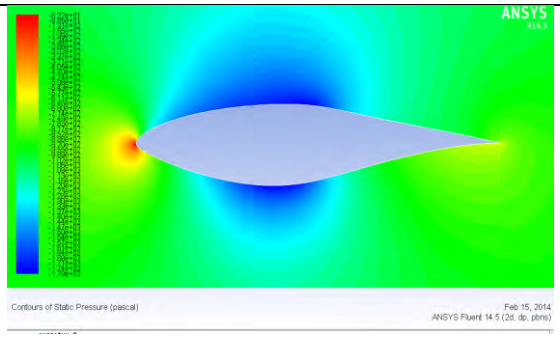	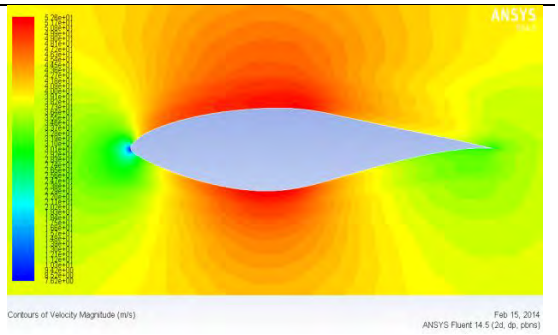
5.13	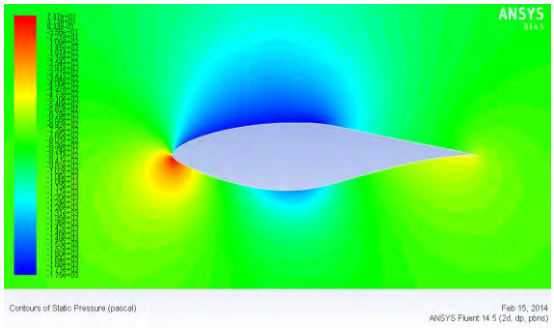	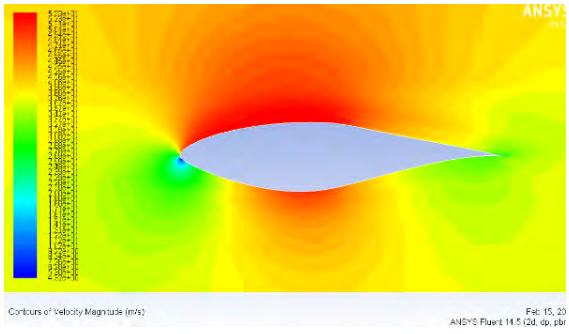

9.22	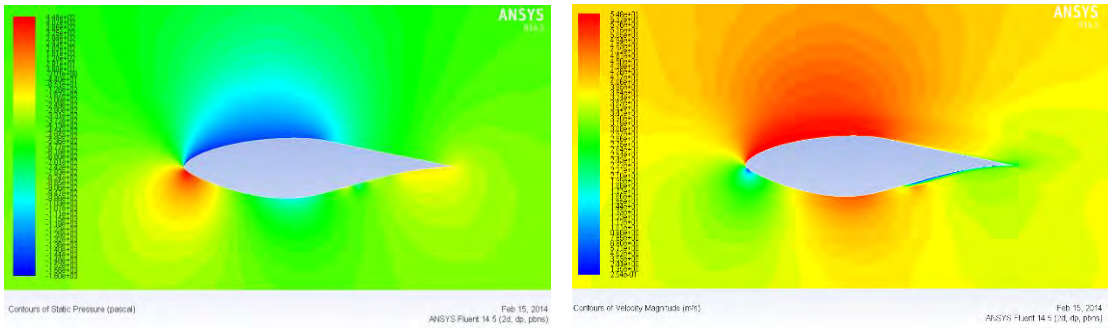
14.24	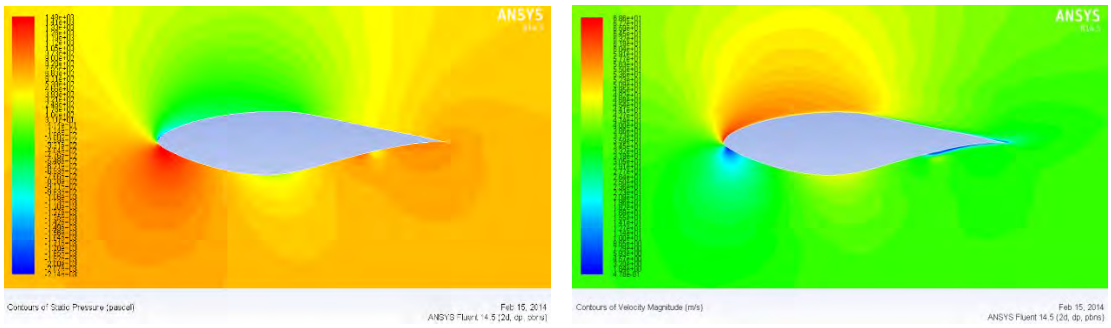

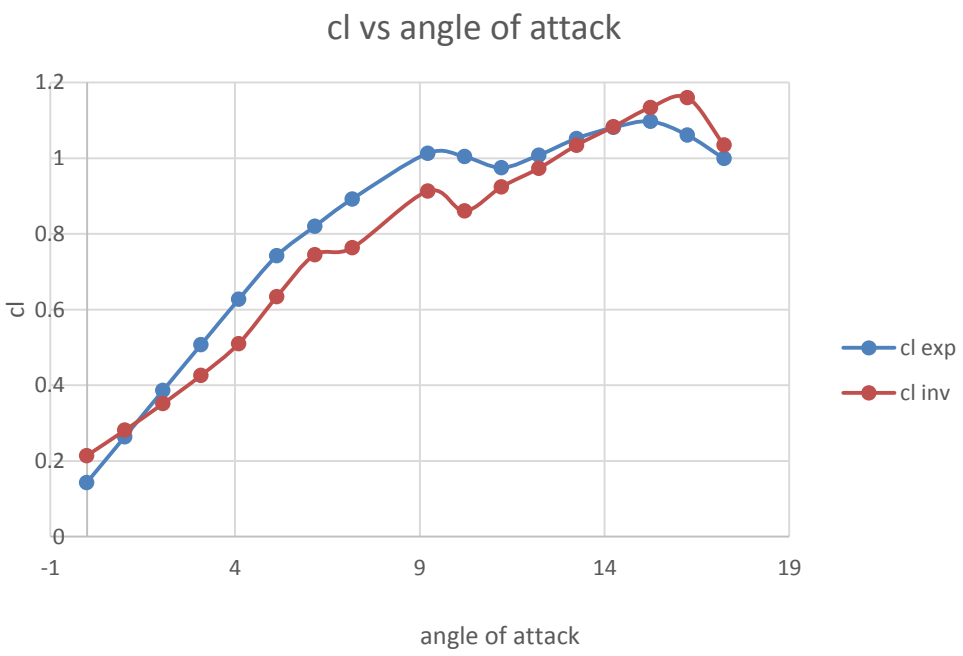

Figure 7: Coefficient of lift vs angle of attack

It is observed that the most effective angle of attack for the S809 is at 14 degrees, and for the range of angle between 9^0 and 17^0, the coefficient of lift is approximately 1. Higher model especially k-ω may more accurately predict the lift coefficient, but satisfactory results are none the less obtained through the current model. The lift data so generated are supplemented into the blade element momentum theory to predict the NREL VI rotor power, to achieve a theoretical higher degree of accuracy.

4. Blade Element Momentum Theory

Blade Element Momentum Theory (BEMT) equates two methods of examining how a wind turbine operates. The first method is to use a momentum balance on a rotating annular stream tube passing through a turbine. The second is to examine the forces generated by the airfoil lift and drag coefficients at various sections along the blade span. These two methods give a series of equations that can be solved iteratively.

4.1 Momentum Theory

4.1.1 Axial Force

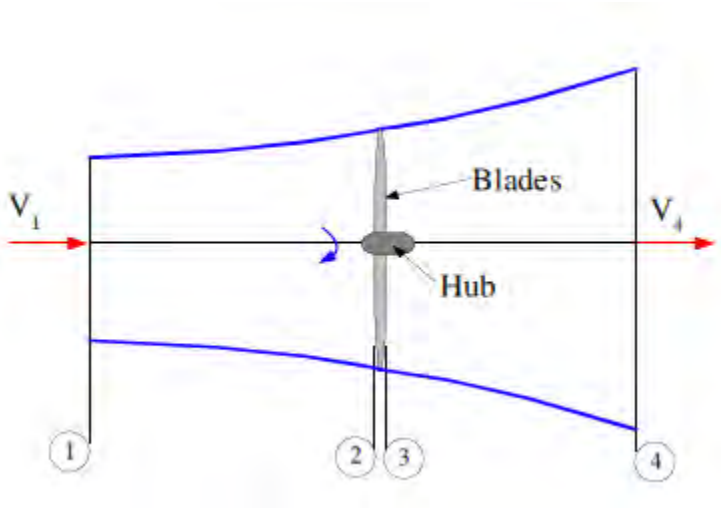

Figure 8: Axial Stream Tube around Wind Turbine

Figure 7 shows the stream tube around a wind turbine. Station 1 is upstream of wind turbine, 2 is just before the wind turbine blade, 3 just after the blade and 4 is downstream of wind turbine. In between section 2 and 3, energy is extracted from wind and results in

pressure gradient. Assume the flow is frictionless in between 1-2 and 3-4, also p1 = p4 and v2 = v3. From Bernoulli's equation,

$$p_2 - p_3 = \frac{1}{2}\rho\,({v_1}^2 - {v_2}^2) \tag{1}$$

Since force is product of pressure and area then, the differential force

$$dF_x = \frac{1}{2}\rho\,({v_1}^2 - {v_2}^2)dA \tag{2}$$

And the axial induction factor, the fractional decrease in the wind velocity between the free stream and the energy extraction device (wind turbine), is defined to be

$$a = \frac{v_1 - v_2}{v_1} \tag{3}$$

Substituting yields

$$dF_x = \frac{1}{2}\rho {v_1}^2[4a(1-a)]2\pi r dr \tag{4}$$

4.1.2 Rotating Annular Stream Tube

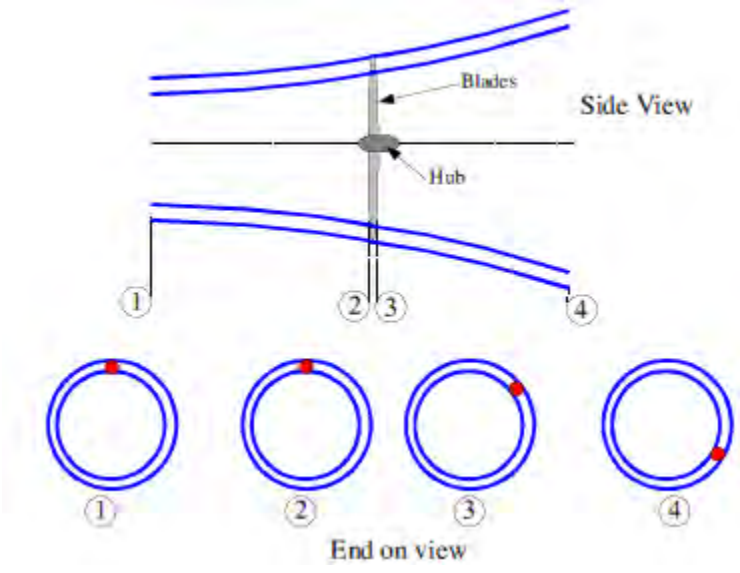

Figure 9: Rotating Annular Stream Tube

In between section 2 and 3, the rotation of the turbine blade imparts rotation into the blade wake. The blade has an angular velocity of Ω, imparting wake in the flow rotating at an angular velocity of ω.

For a small element the corresponding torque is

$$dT = dm\omega r^2 \tag{5}$$

For a rotating annular element

$$dT = 2\pi\rho v_2 \omega r^2 dr \tag{6}$$

The angular induction factor is

$$a' = {}^{\omega}/_{2\Omega} \tag{7}$$

Thus,

$$dT = 4a'(1-a)\rho\pi r^3 v dr \tag{8}$$

The momentum theory thus resulted in formulation of the axial force (eq.4) and tangential force (eq.8) on an annular element of fluid.

4.2 Blade Element Theory

The theory consists of two key assumptions. One, there are no aerodynamic interaction between blade elements and secondly, lift and drag forces determine the forces on the blade.

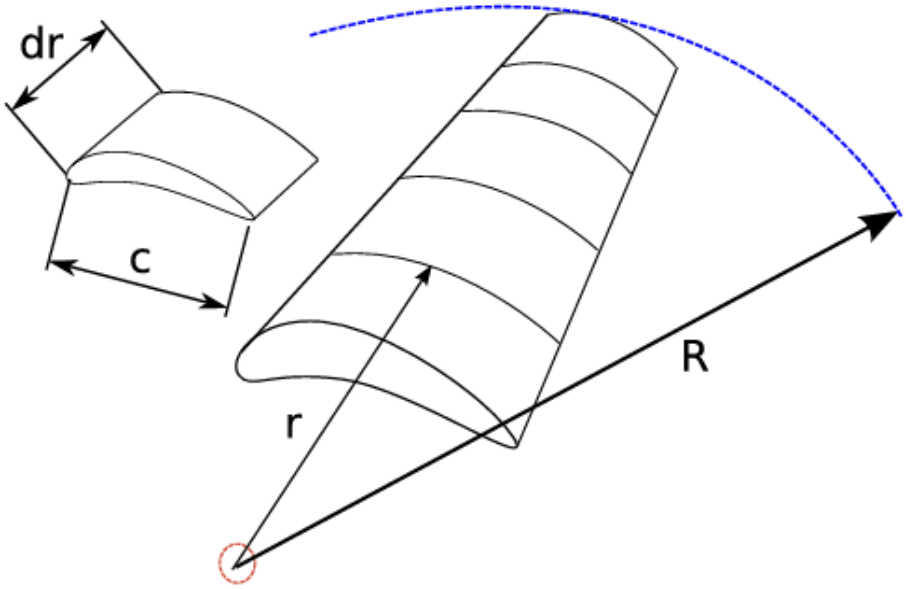

Figure 10: Blade Element

Each of the blade elements will experience a slightly different flow as they have a different rotational speed (Ωr), a different chord length (c) and a different twist angle (θ). Blade element theory involves dividing up the blade into a sufficient number of elements and calculating the flow at each one. Overall performance characteristics are determined by numerical integration along the blade span.

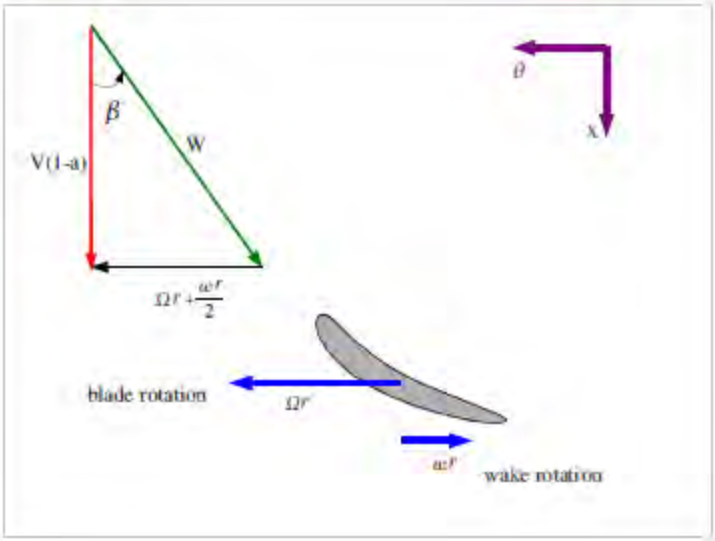

Figure 11: Flow Into Blade

The airflow experience wake rotation after leaving the trailing edge. No rotation is imparted when flow approaches the leading edge. The blade wake rotates with speed ω. The average tangential velocity is

$$\Omega r + \frac{\omega r}{2} = \Omega r(1 + a') \tag{9}$$

$$tan\beta = \Omega r(1 + a')/(v(1 - a)) \tag{10}$$

The local tip speed ratio and relative velocity are given by,

$$\lambda_r = \Omega r/v \tag{11}$$

$$w = v(1 - a)/cos\beta \tag{12}$$

The local blade solidity,

$$\sigma' = Bc/(2\pi r) \tag{13}$$

By definition the lift and drag are perpendicular to the incoming flow. For each blade element the tangential and axial components of forces are

$$dF_\theta = dLcos\beta - dDsin\beta \tag{14}$$

$$dF_x = dLsin\beta + dDcos\beta \tag{15}$$

The torque on the element is the tangential force times the radius. Substituting the basic definition of lift and drag in terms of their respective coefficients results in

$$dF_x = \frac{\sigma'\pi\rho v^2(1-a)^2(c_L \sin\beta + c_D cos\beta)rdr}{cos^2\beta} \tag{16}$$

$$dT = \frac{\sigma'\pi\rho v^2(1-a)^2(c_L \cos\beta - c_D sin\beta)rdr}{cos^2\beta} \tag{17}$$

A correction factor is introduced in the BEMT to account for the losses occurred due to wind tip vortices on turbine blade. The factor ranges from 0~1 and characterizes the reduction in forces.

$$Q = \frac{2}{\pi}\text{acos}\left[exp\left\{-B/2(1-\frac{r}{R})/\left(\frac{r}{R}\right)cos\beta\right\}\right] \tag{18}$$

The power output can finally computed as,

$$dP = \Omega dT \tag{19}$$

$$P = \int_r^R dPdr$$

$$P = \int_r^R \Omega dTdr \tag{20}$$

The power coefficient is given by

$$C_p = \frac{8}{\lambda^2}\int_{\lambda_h}^{\lambda} Q{\lambda_r}^3 a'(1-a)[1 - c_D/c_L \tan\beta]d\,\lambda_r \tag{21}$$

The entire process of BEMT is an iterative process. It is also the first process to be looked into in the design of wind turbine blade, propeller blades, rotor blade, etc.

4.3 Result and Discussion

NREL VI wind turbine blade, unlike others, has a linear change in the chord of the blade as the span increases. Using the initial blade geometry and setting up a linear change in chord, the NREL VI power was simulated in a matlab generated code. The lift coefficient and drag coefficient for Re = 2 x $(10)^6$ was used in calculating the tangential and axial forces.

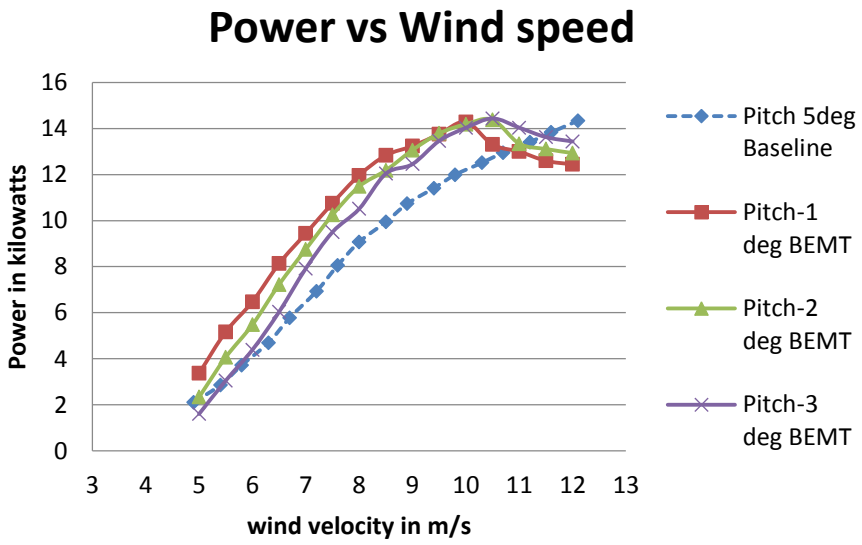

Figure 12: Power vs Wind Speed

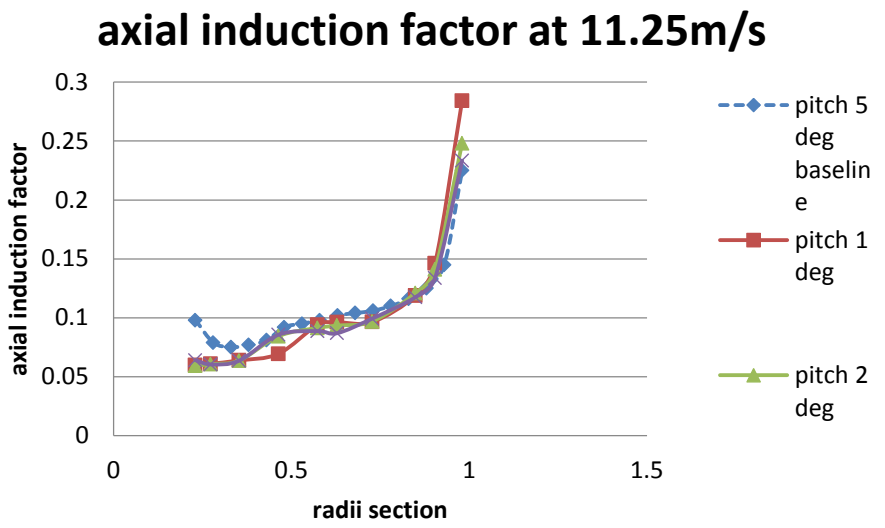

Figure 13: Axial induction factor

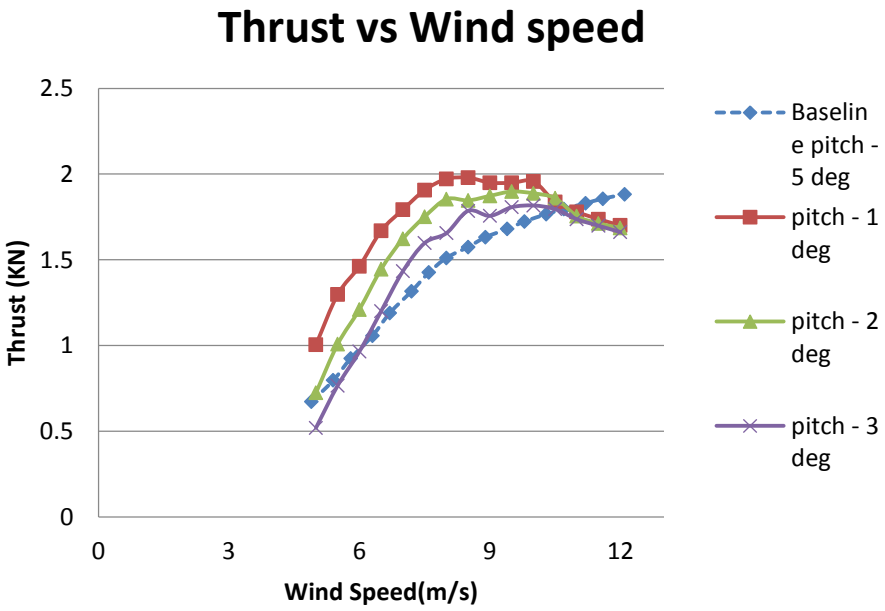

Figure 14: Thrust vs Wind Speed

Numerical iteration from BEMT with varying pitch angle from 1^0 to 3^0 predicted reduces error percentage as the pitch of the turbine blade was increased. Clearly as seen from

Figure 11, 12 and 13, the BEMT approximation of the power and thrust curves approach more towards the baseline pitch of 5^0. When the pitch angle was increased to a higher increment, it lead to an increased inflow angle causing the angle of attack of the local blade element to reach a value higher than the max angle of attack available in the data of lift coefficient and drag coefficient generated from CFD simulations. Thus effective results could not be attained at higher pitch. In theoretical practice, a lifting line theory approximates the lift coefficient for BEMT, but the data so generated fails to apply for higher angle of attack, because the drop in lift coefficient due to stalling cannot be visualized or computed. As seen from the plots, at low pitch angle the BEMT over predicts the power and thrust, but the experimental set up data is unavailable for corresponding pitch. Increase in pitch of the turbine blade for experimental analysis, results in an increased turbulence downstream of the blade, at some angle higher turbulence wake causes incremental change in the axial and tangential induction factor, resulting in power loss.

In short, BEMT as stated earlier is an iterative process. Initial guesses of axial induction factor and tangential induction factor defines the speed of convergence of the computation. The parameters are updated in every single iteration loop, and the variables are directly or indirectly dependent on other function which in turn depends on another.

Overall accuracy of the BEMT is fairly good but its assumptions when the rotor disk is yawed and when rotor wake influence most of the aerodynamic characteristic is questionable. Although a corrected BEMT method is being researched into and applied, the trend to achieve better results still depend on implementation of computational fluid dynamics analysis.

4.4 Failure Implementing Conventional Optimization Model in BEMT

As far as literature review was conducted, certain available journals explained in brief about optimization of a wind turbine blade but, the objective of the optimization was on weight and dimensional effect on stresses produced from the pressure load from reacting flows.

During the preliminary design of a wind turbine blade, BEMT is the first available tool readily used. If accurate C_L and C_D data are available for the airfoil sections to be used in the code, then fairly accurate results can be achieved. Variables like chord and twist of the blade at different radii section will be responsible for the actual design of the blade. If within the BEMT a mathematical optimization tool could be implemented resulting in an optimized chord and twist distribution on the blade for a wide range of wind speed, with an objective function as maximum power output, then the need to conduct CFD analysis over the blade design frequently to achieve a better design could be reduced. With that in view, several attempts made to successfully implement the mathematical code with the BEMT resulted in failure.

Mathematical optimization requires the need to compute derivatives of a function and its higher derivatives. For a polynomial equation, simple model of a heat exchanger or even structural problem, computing the derivatives and finding a local minimum or maximum dimension for satisfactory convergence to objective function is fairly simple. Provided the necessary conditions for optimization is satisfied, like the first order necessity condition, second order necessity condition, etc.

In BEMT, most variable are dependent on another variable resulting in a loop. The design variable was chord and twist of blade at different radii section and the objective function was maximizing coefficient of power. Initially, the derivatives of the objective function were derived, and search direction for the roots provided, but complication arose when constraints for the design variable were added for optimization.

Unconstrained optimization resulted in divergence of the solution, however when the equation 21 was used holding most variable other than chord constant, the resulting power coefficient exceeded the betz limit which is the theoretical maximum. For proper convergence for an optimum all variables has to be constrained and should not be held constant.

5. Validation: NREL-VI CFD Simulation

5.1 Sequence S Test Configuration

NREL VI wind turbine blade is equipped with electronic pressure transducers connected to pressure orifices located at 5 separate location along the blade span at r/R = 0.3, 0.47, 0.63, 0.8, 0.95. Since only upstream operating conditions are being considered, and influences of tower and nacelle on solution are assumed to be negligible, the blade is modeled without the tower and nacelle. Moreover, to further reduce the complexity of meshing, the existences of pressure orifices are negated in blade model. The blade is designed in "ANSYS Component System – Geometry" as per blade specifics provided in Table 1. Modeling in "Component System – Geometry" as opposed to modeling in other CAD software is mainly for flexibility reasons because the same baseline design is later used for optimization purpose. The rotor cone angle is 0^o and pitch is set at 3^o to model the Sequence S Unsteady Aerodynamics Experiment conducted with following operating conditions:

Table 4: Sequence S Operating Conditions

Serial	Wind Speed (m/s)	Density(kg/m^3)	Rotational Speed(rad/s)
1	5.03	1.243	7.53
2	7.016	1.245	7.539
3	10.051	1.2458	7.555
4	13.071	1.2266	7.554
5	15.096	1.2240	7.550

5.2 NREL VI Wind Turbine Geometry Model

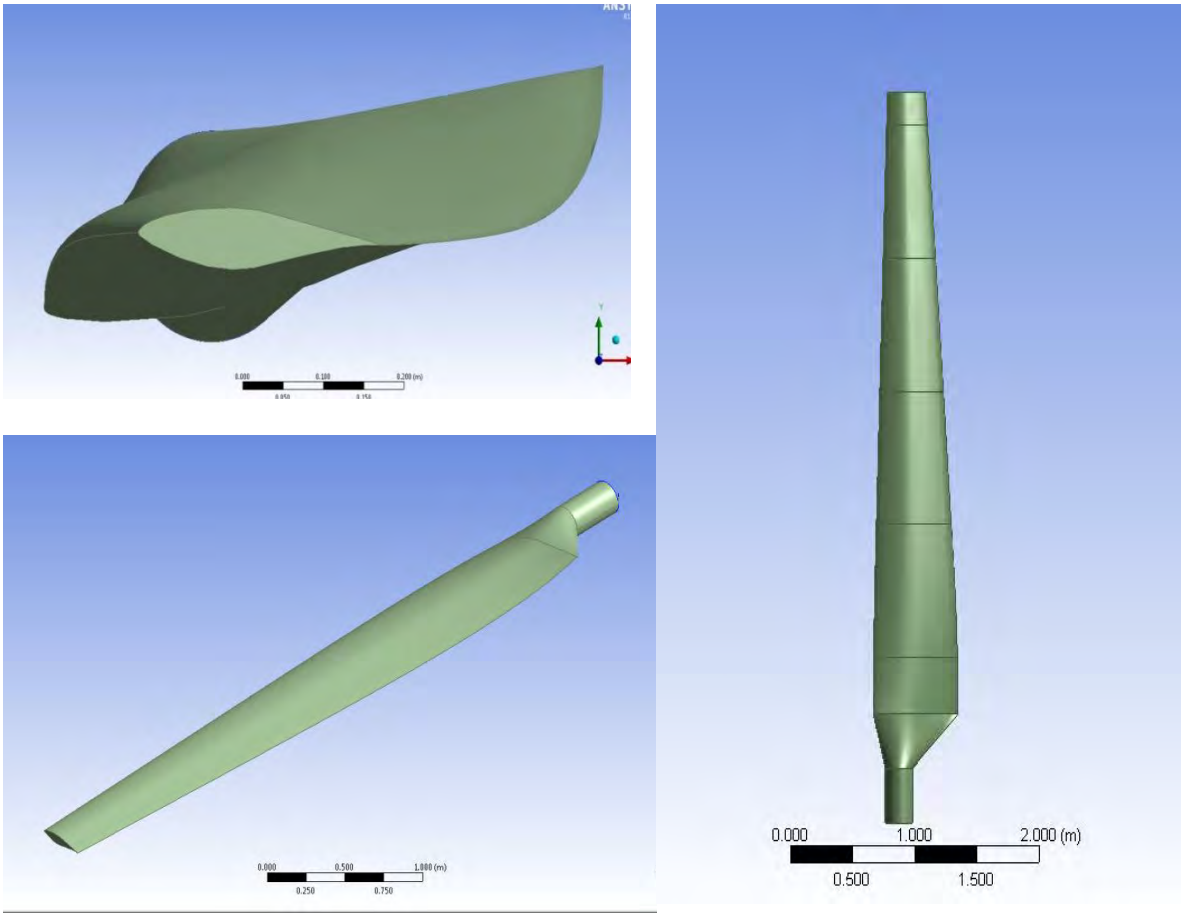

Figure 15: NREL VI Blade Model

The original definition of NREL S809 is characterized by a sharp trailing edge which has been thickened to 0.001 m in the manufactured experimental blade. Also in construction of the grid around sharp trailing edge, mesh skew was extremely high and resulted in poor structured mesh. Thus, blade geometry model had its trailing edge rounded by a thickness of 0.001 m following experimental example. Slight modification as such does not have drastic impact on the numerical scheme since even the experimental blade could not be manufactured with precise definition. Table 1 clearly defines the blade but the

transition from the cylindrical hub attachment to root section at 1.257 m is partially defined. Thus, a smooth transition connecting the two sections was drawn for simplification.

5.3 Computational Domain and Grid

Literature survey has shown a varying length of computational domain, cell count and also has mostly used the non-yawed case of Sequence S U.A.E. test. The non-yawed case allowed for rotationally periodic conditions to be applied reducing to a single blade and half cylinder computational domain. POINTWISE V17 was used to generate the numerical grid for computation.

The length of the domain is 30 times the blade radius with blade placed at 10 times the radius from the inlet of the domain, and downstream of the domain is 20 times radius leading to outlet. Semi-circle enclosure contributes as far field is at 10 times radius.

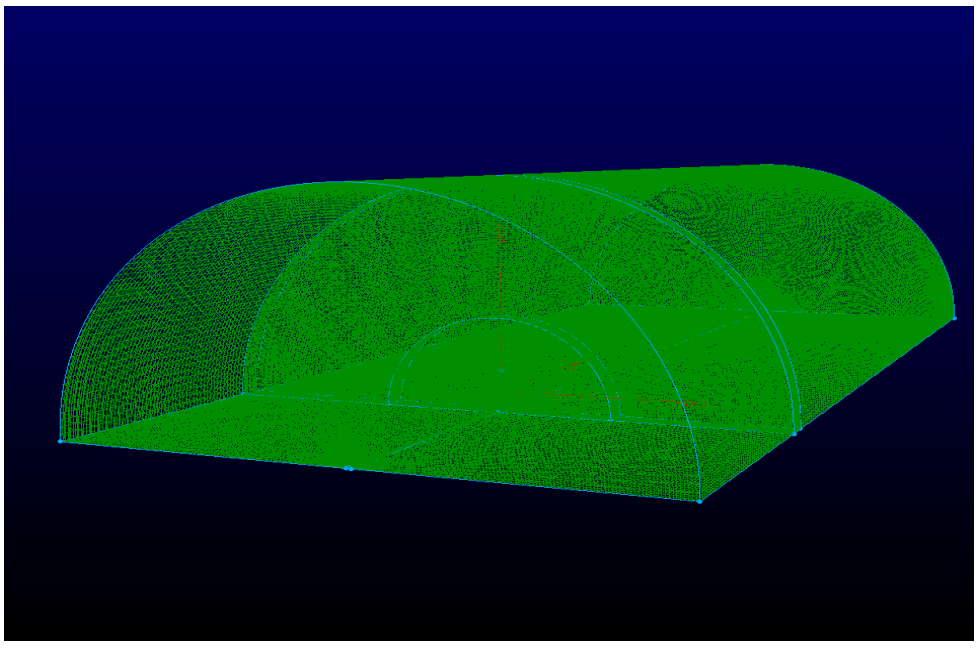

Figure 16: Computational Domain

Computational domain was segregated into 4 blocks with the upstream and downstream of the block composed of a structured mesh. T-Rex command is used to form an unstructured mesh in the block surrounding the blade. This domain extends to 4 times the blade radius. The remaining block lying above unstructured block is a composed of structured mesh. Figure 17 displays the cut section view of the internal computational domain and the blade boundary layer extrusion.

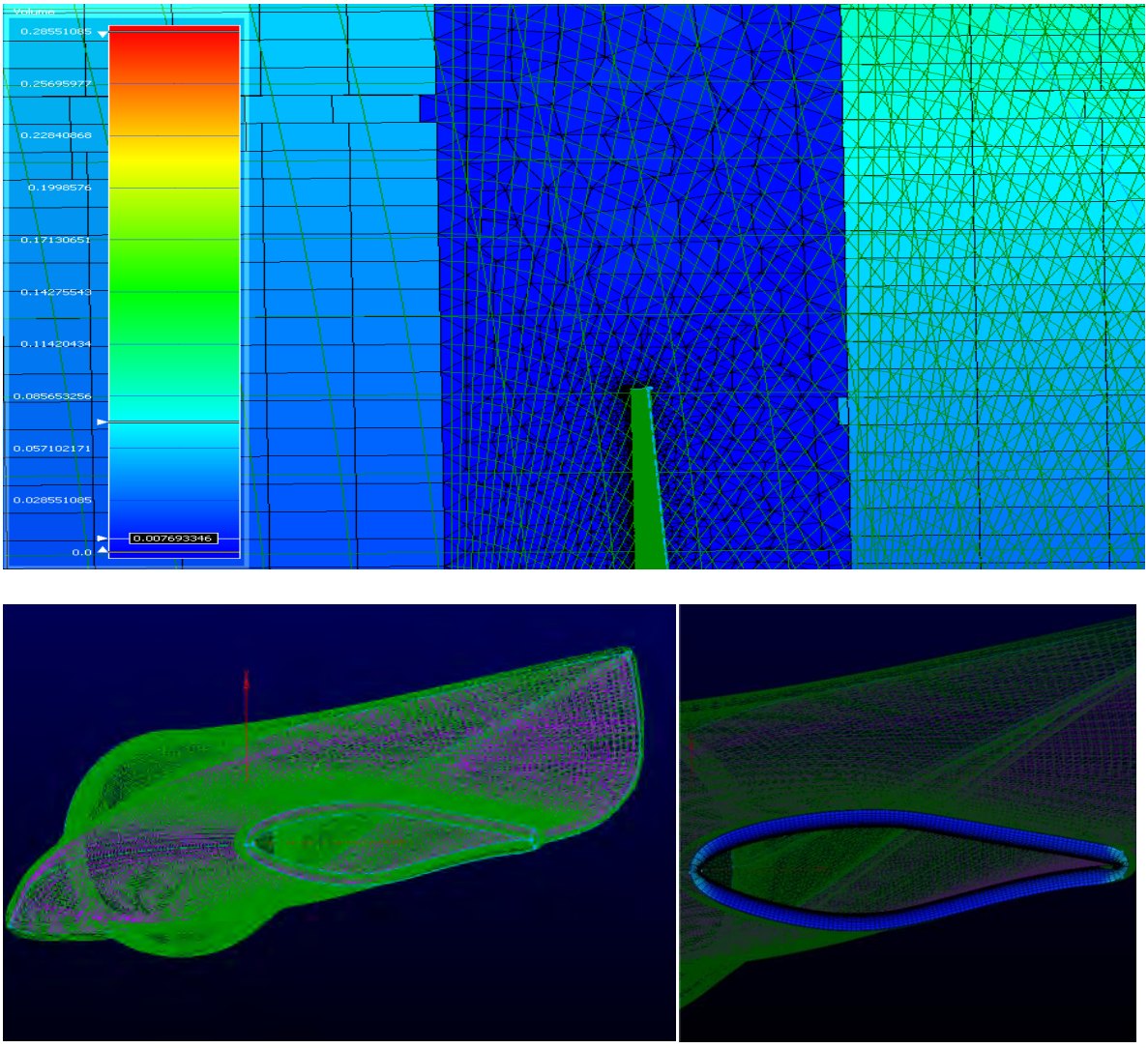

Figure 17: Top: Section View of Domain; Bottom: Boundary Layer

The blade consist of 198 circumferential division while along the span has 198 divisions. To maintain a y^+ approximate to 1, the first layer of cell extrusion has a height of 4.53 x 10^{-5} m, over 20 layers with a specified growth rate of 1.2.

5.4 FLUENT Simulation

The blade is modeled as a frozen rotor, while the fluid is specified to be the rotating reference frame. This prevents the need for sliding mesh where the reliability and the accuracy is questionable, unless a user defined function is specified for a sudden transition of flow between the interfaces. Upstream of the blade in the domain the wind speed is specified and the inlet is treated as a velocity inlet since the flow speed is known. The posterior of the flow domain is specified to be a pressure outlet. The blade is specified as a wall with no slip condition specified and the domain around the rotational axis is labeled as symmetry. The rotationally periodic boundary condition used in FLUENT allows the simulation of only one blade provided the flow field is uniform and aligned with the axis of rotation. The rotation is simulated with the moving reference frame, the entire flow domain is considered to be rotating with the blade and absolute velocity formulation is a must.

Literature survey conducted suggested the use of k-ω SST turbulence model. Although higher numerical scheme are readily available, this 2 equation model captures transition from laminar to turbulent to a higher accuracy provided y^+ is maintained less than 2.

All simulations were computed in steady state solver until convergence or till the end of prescribed iterations to allow developed flows in the domain. Then in order to maintain computational stability, the simulations were switched to transient solver.

5.5 Results

5.5.1 Comparison of Power Output

The use of k-ω SST turbulence model predicts the power generated at up to 10 m/s with high degree accuracy. However, at higher wind speed the model fails to accurately predict the torque obtained. Figure 17, displays the curve of power thorough experimental, BEMT and the computational analysis. The power obtained is calculated from the product of torque and angular velocity. As expected, BEMT over predicted the power even though the lift coefficient and drag coefficient were provided through 2D CFD simulations. Failure to obtain agreeable accuracy above 10 m/s of wind speed may be related to the turbulence model used or varying the solver scheme for pressure might result in better accuracy since, rotation of the fluid does provide a steep pressure gradient at high wind speed.

Table 5: Tabulation of Power at Various Wind Speed

Serial	Wind Speed (m/s)	Torque (N-m)	Power (KW)
1	5	257.64	1.942
2	7	756.864	5.707
3	10	1361.47	10.265
4	13.1	899.96	6.785
5	15.1	701.35	5.288

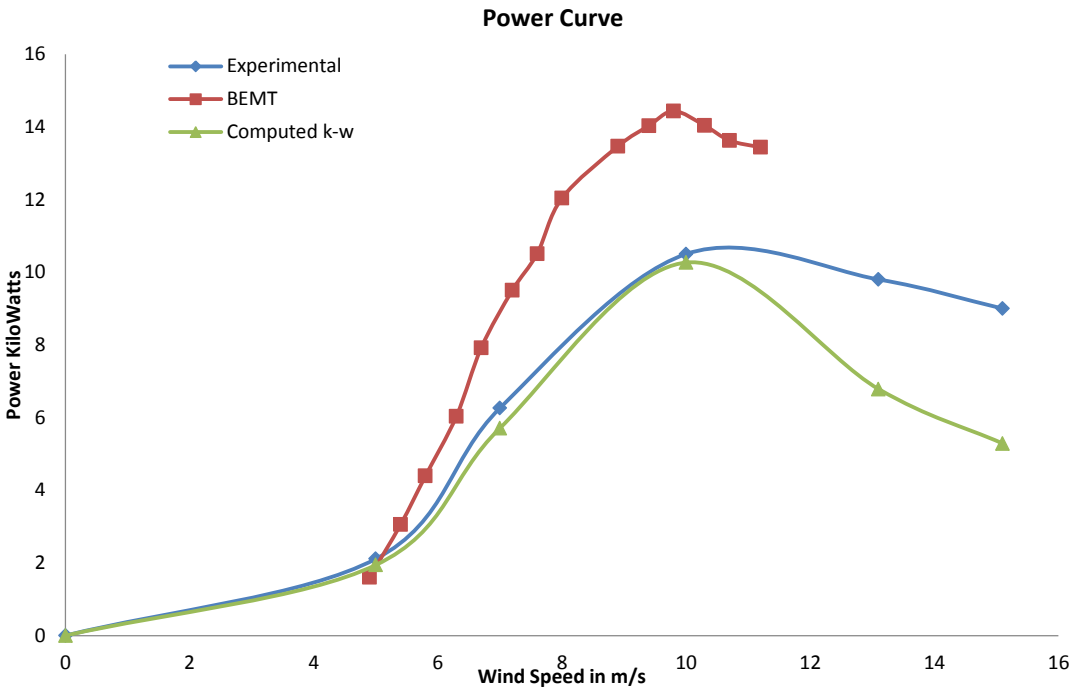

Figure 18: Power Curve Comparison

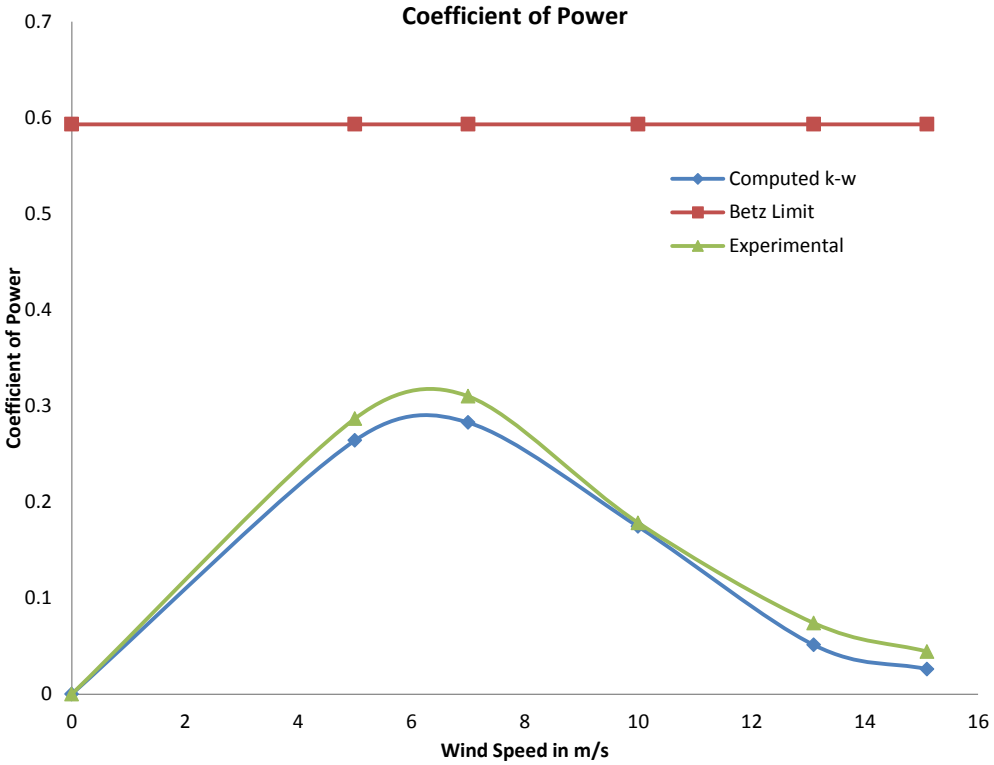

Figure 19: Coefficient of Power

The theoretical limit of efficiency of a wind turbine is termed as the Betz Limit at 59.3 %. Comparison of Coefficient of Power, a measure of how efficiently a wind turbine converts the energy available in the wind to electricity, is defined by Figure 18.

5.5.2 Flow Visualization and Pressure Coefficient Distribution

Velocity streamlines, Pressure Contours, Turbulent Intensity and Coefficient of Pressure distribution on both the pressure side and the suction side of a wind turbine is clearly displayed in the upcoming figures. Like, other literature review, it is interesting to see how at low wind speed up to 7 m/s, the flow is laminar and attached through most of the span of the blade except for the cylinder section at the blade base where it is generally connected to the Hub. No visible transition is observant up to 7 m/s. However, with increasing wind speeds the transition moves outboard from the root section towards the tip. The stagnation point dynamic pressure are used to render the coefficient of pressure dimensionless.

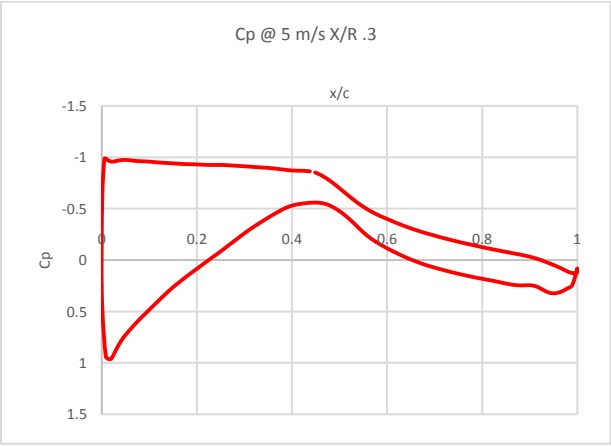

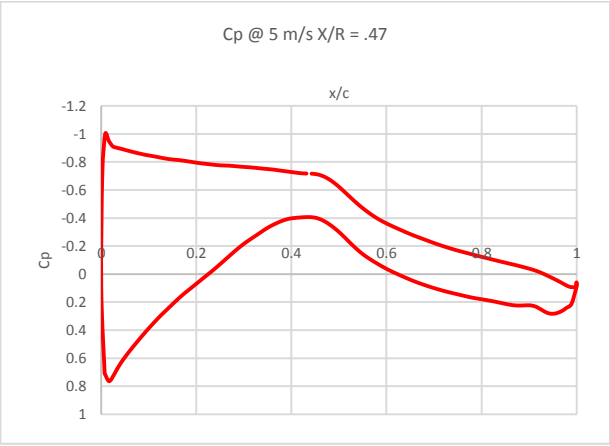

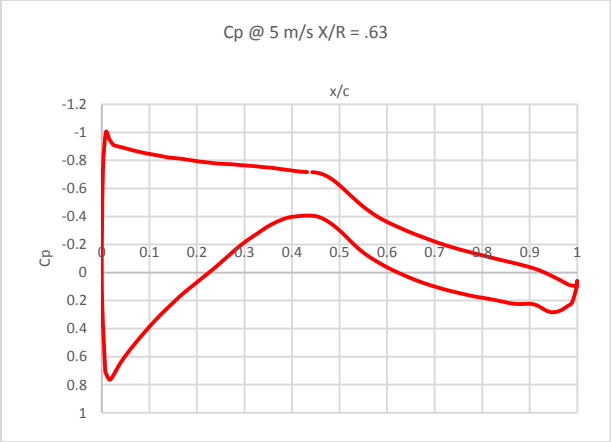

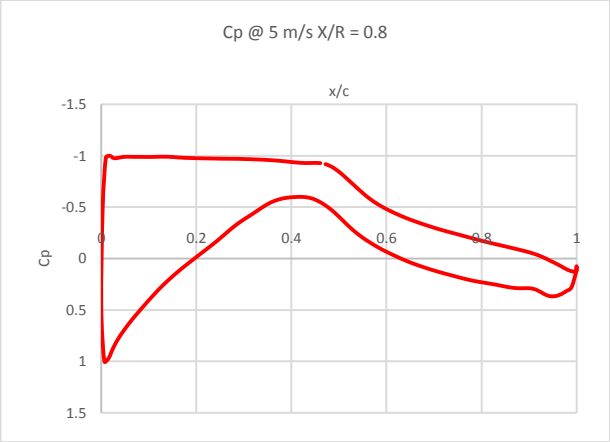

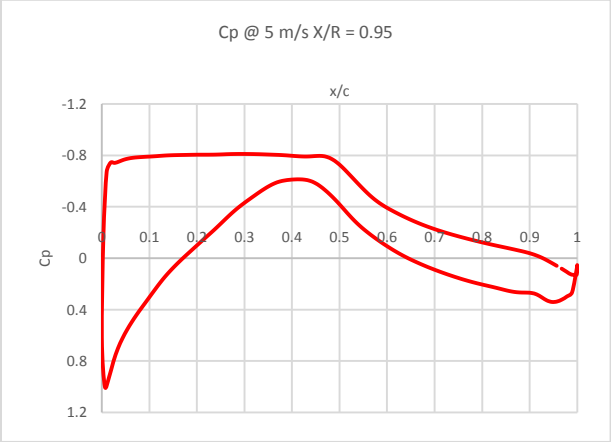

Figure 20: Coefficient of pressure distribution at 5 m/s

Pressure coefficient over a dimensionless x/c represents the characteristics of the flow over the region. As represented by the above plots for 5 m/s and upcoming plots at 7 m/s, the pressure gradient observed display the characteristic of an attached flow. Along with the pressure contour below, the plots portrays a large pressure difference along the primary of the blade. That contributes most of the lifting force for power production. When compared with literature survey and benchmark validation, the plots are in good agreement. Velocity streamlines for both 5 m/s and 7 m/s show fully attached lines, with flow separation towards the hub where the cylinder extrusion connecting the blade to the hub is noticeable.

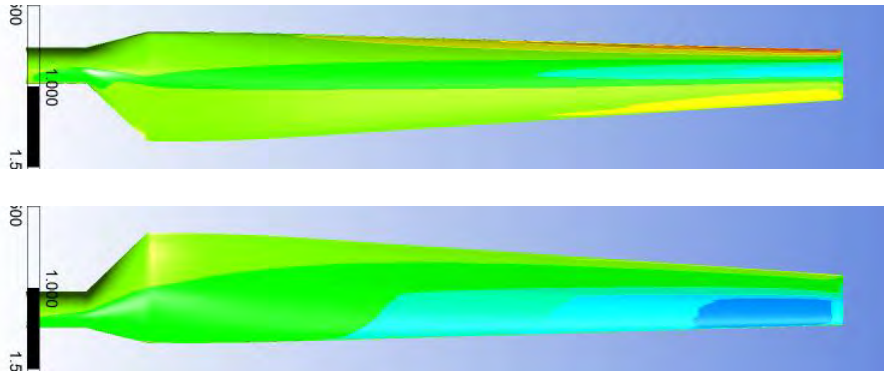

Figure 21: Pressure Contours, Top- Pressure, Bottom - Suction

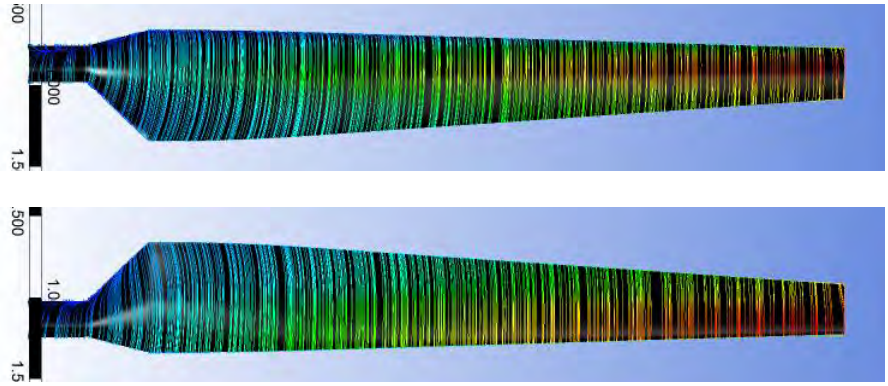

Figure 22: Velocity Stream lines, Top - Pressure side, Bottom Suction Side

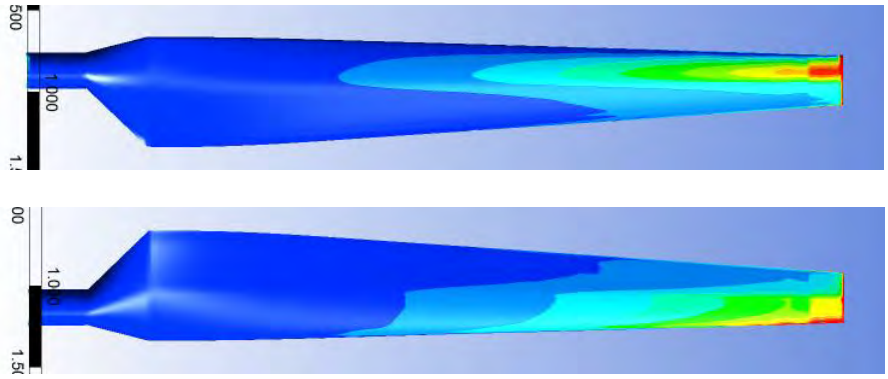

Figure 23: Turbulent Intensity, Top- Pressure, Bottom - Suction

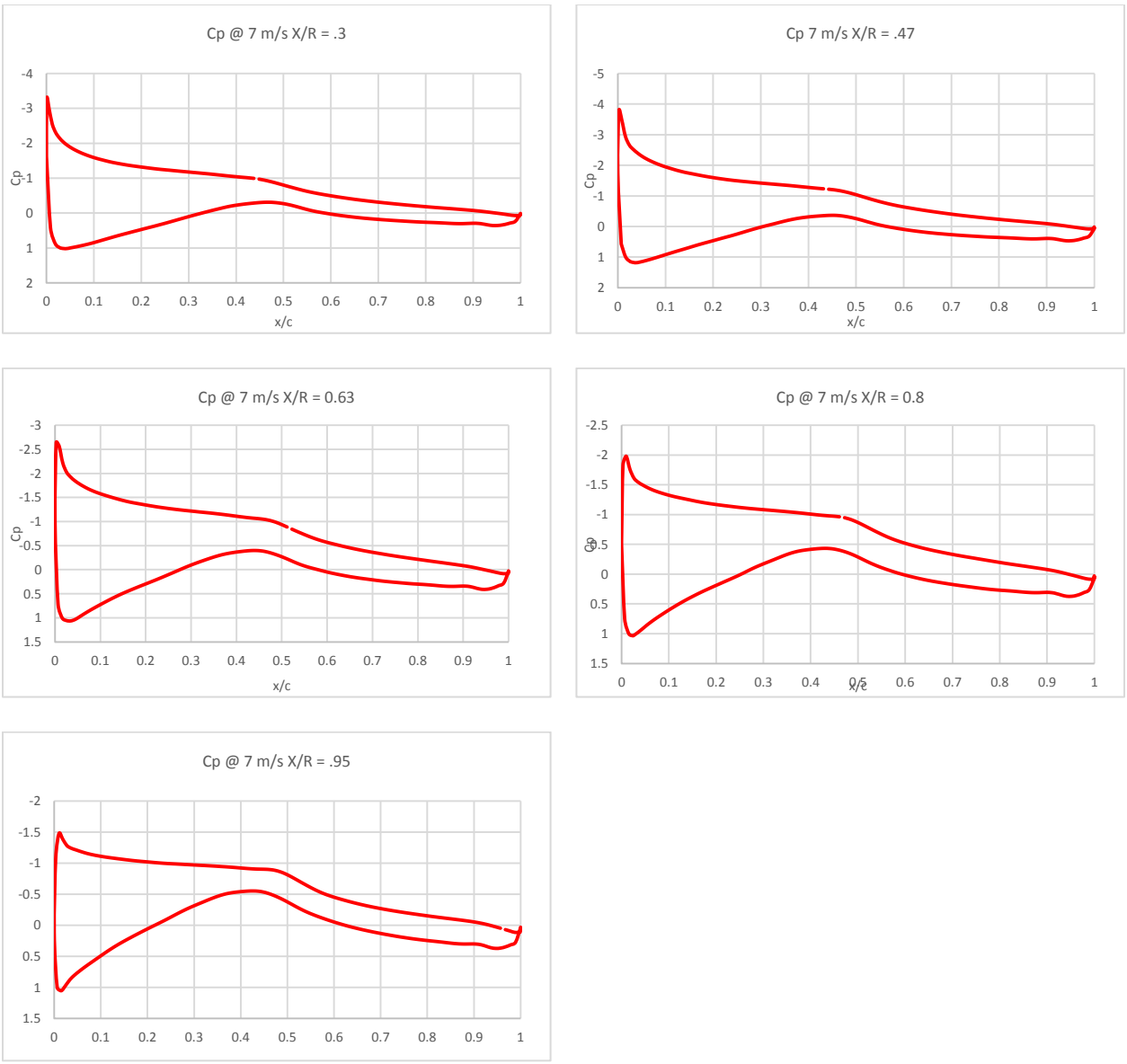

Figure 24: Coefficient of Pressure Distribution at 7 m/s

Pressure coefficient distribution remains similar to 5m/s case with no visible flow separation on the blade surfaces.

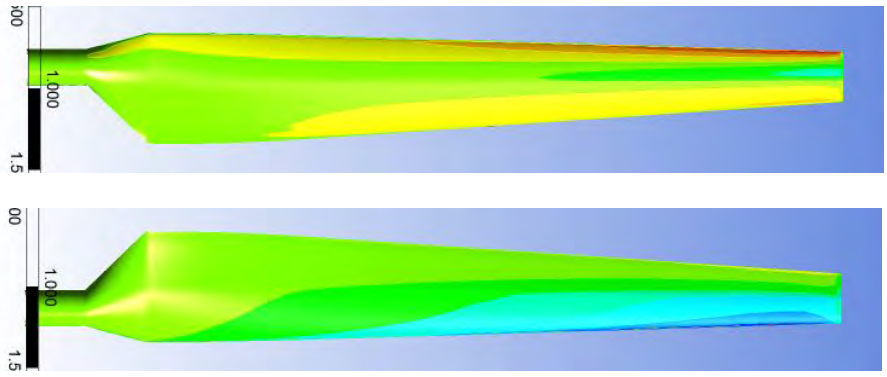

Figure 25: Pressure Contours, Top - Pressure, Bottom -Suction

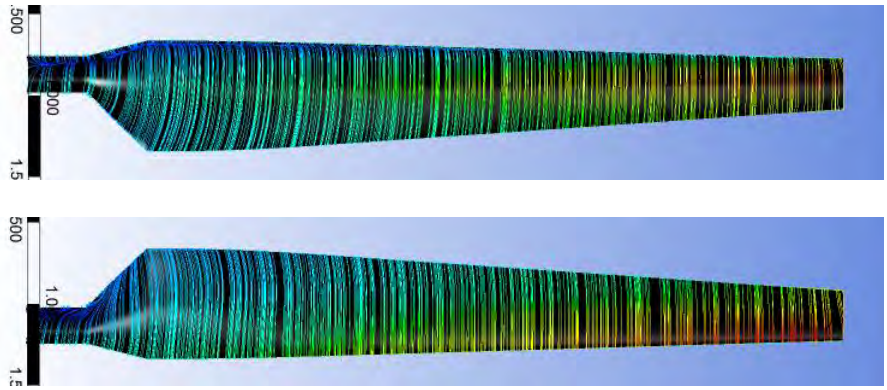

Figure 26: Velocity Streamlines, Top -Pressure, Bottom -Suction

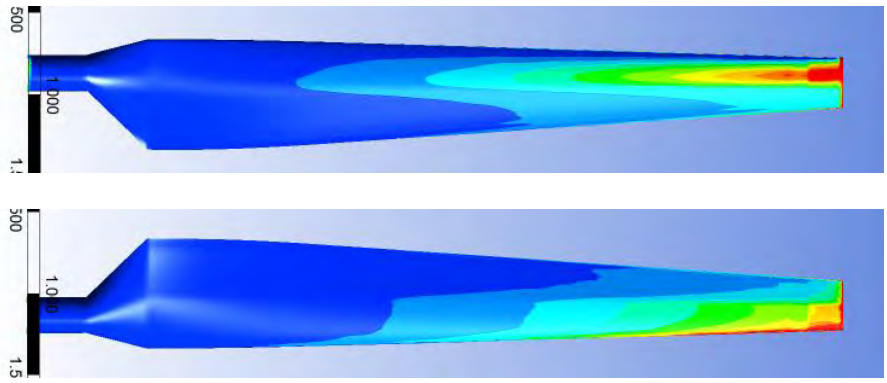

Figure 27: Turbulent Intensity, Top - Pressure, Bottom - Suction

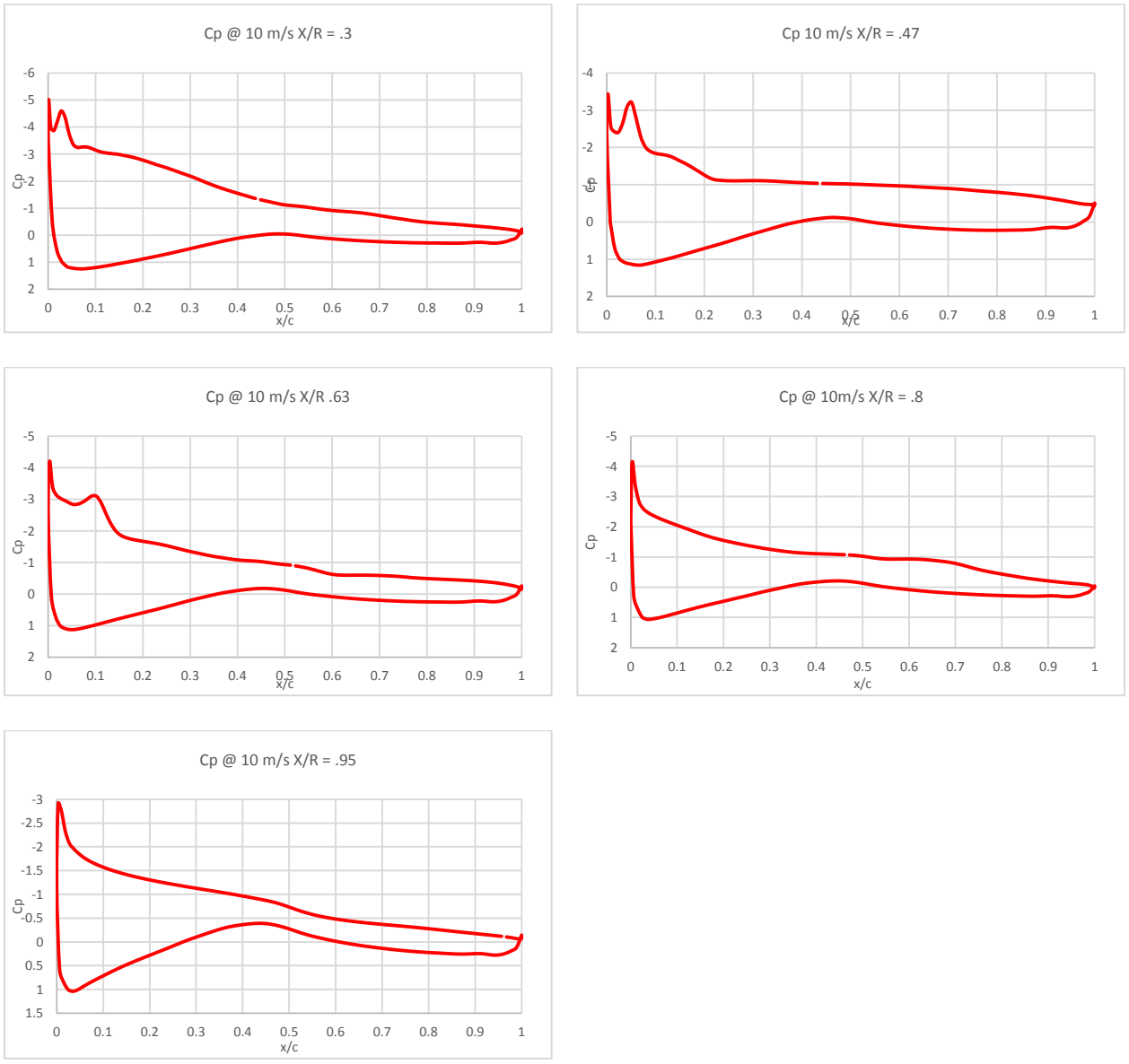

Figure 28: Coefficient of Pressure Distribution at 10 m/s

Unlike the low wind speed cases, 10 m/s marks the onset of stall. The pressure coefficient distributions highlights the peak of adverse pressure gradients towards the suction side of the leading edge, flow separation is well observed at 30% span moving outboard to 63 % span location. The turbulent separation also moves from the leading edge progressively towards the trailing edge as the transition moves outboard along the blade span. At

roughly about 75% the transition moves towards the trailing edge and at 85% span location upwards the flow is again attached. From 30% to 63% the second half of suction side of the blade displays a constant pressure gradient, marking the stall onset in the local vicinity and also a region of separated flows. Although, a slight decreasing pressure gradient on the suction side can be observed just after the separation, it is caused mainly due to cross flow of the wind due to rotational effect. The streamlines on the suction side from the figure below shows oblique vortex flows on the blade surface originating from flow separation and cross flows from rotation starting at the blade root and progressively moving outboard and towards the trailing edge, just as depicted by the pressure coefficient plots.

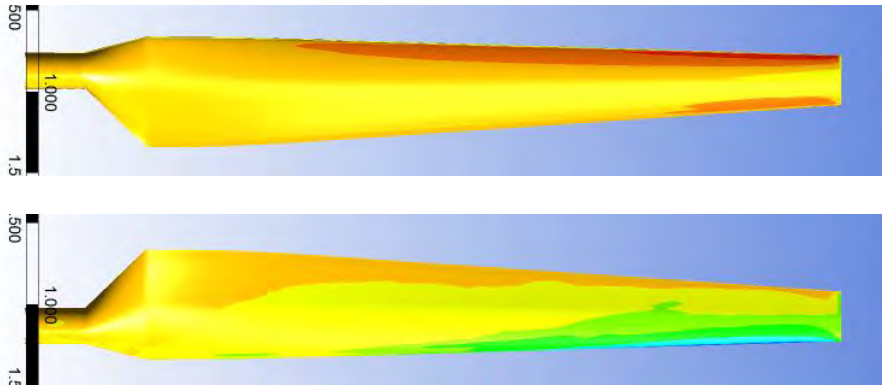

Figure 29: Pressure Contour, Top - Pressure, Bottom - Suction

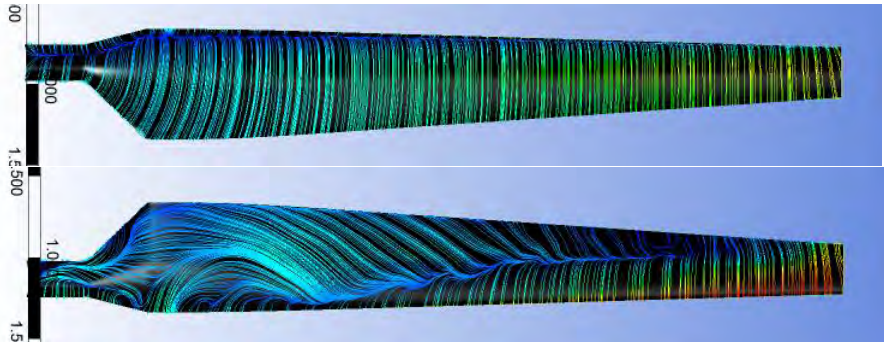

Figure 30: Velocity Streamlines, Top- Pressure, Bottom - Suction

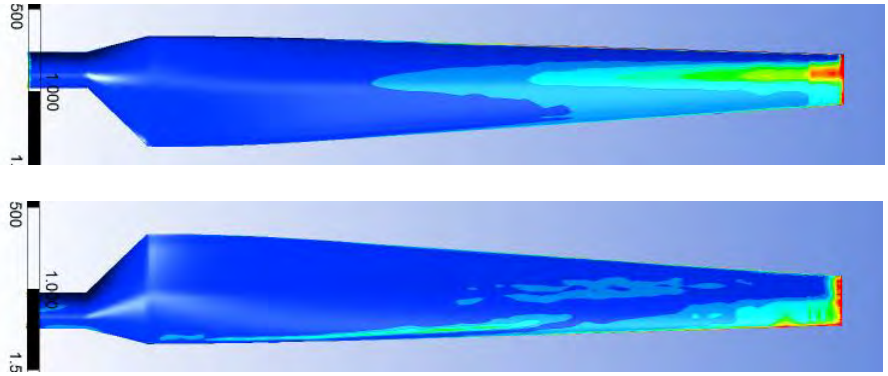

Figure 31: Turbulent Intensity, Top - Pressure, Bottom - Suction

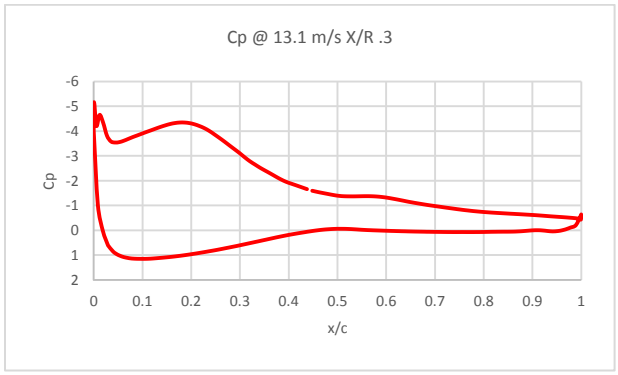

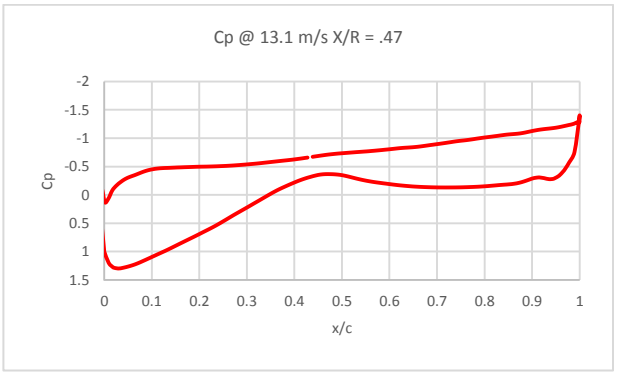

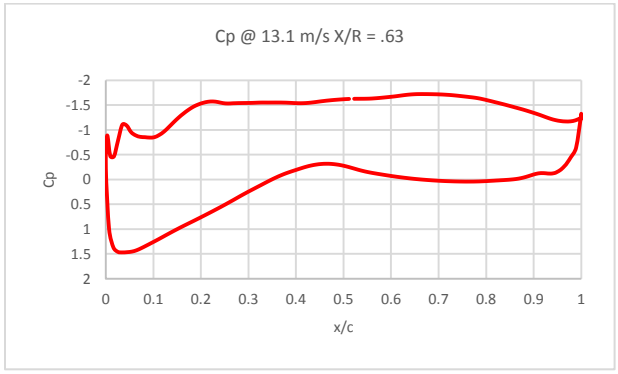

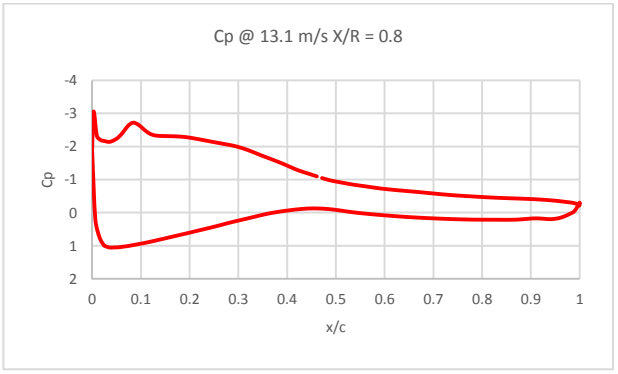

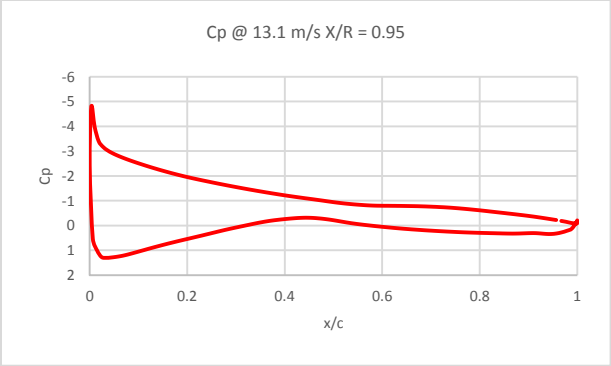

Figure 32: Coefficient of Pressure Distribution at 13.1 m/s

At 13.1 m/s wind speed, turbulent flow is well observed from the plots above up to 80% span. The flow separation has moved upward toward the leading edge from the suction side. At radial span of 47% and 63%, there is a positive pressure gradient towards the trailing edge. Highly separated turbulent flows creates an adverse pressure gradient which contributes to improper approximation of the aerodynamic forces. The pressure coefficient plot at 95% has the characteristics of an attached flow which is very well confirmed by the velocity streamlines portrayed in the figure below.

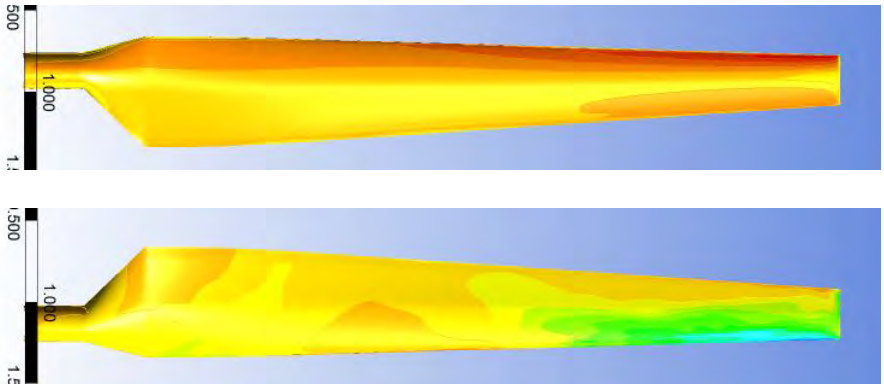

Figure 33: Pressure Contour, Top - Pressure, Bottom - Suction

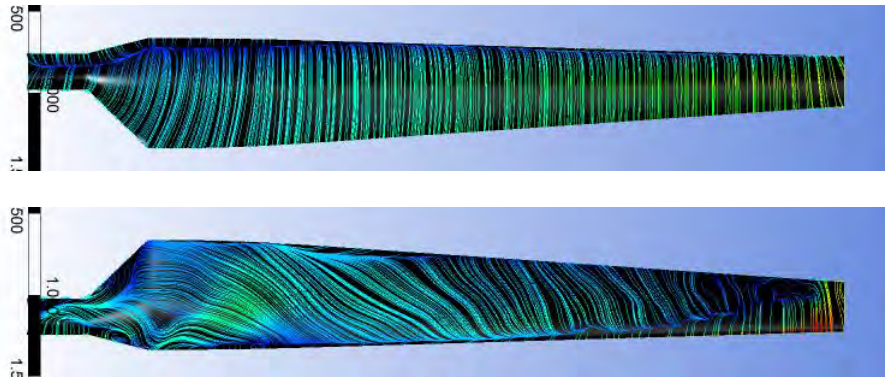

Figure 34: Velocity Streamlines, Top - Pressure, Bottom - Suction

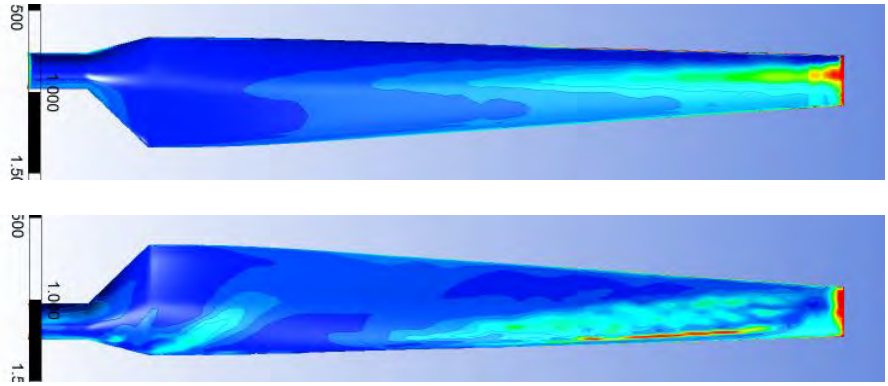

Figure 35: Turbulent Intensity, Top - Pressure, Bottom - Suction

6. Aerodynamic Optimization

6.1 Introduction

Although research are being conducted into an efficient and elaborate method for aerodynamic optimization, many still rely on the use of conventional tool of trial and error. For an expert in aerodynamics with years of experience in design and analysis, constructing a geometry for optimum aerodynamic performance may be easy but still has to rely on CFD and experimental analysis to further fine tune the geometry. These conventional techniques fall under a number of categories:

- Trade studies: A large number of configurations is proposed from among which the best are selected, the results of selection is normally based on screening conducted by CFD analysis. The best of these are then later tested in wind tunnel.
- Conventional optimizers: It works on the mathematical principles of optimization which are derived from numerical analysis, where derivatives estimation exist by use of various solver schemes.
- Ad-joint method: It is derived from control theory and is also extensively being researched into. It allows a deterministic type optimization using a very few iterations of the flow analysis code. It often requires very few iterations provided a good starting point is provided.

Many aerodynamic optimization require a large bound of constraints which prohibits the use of conventional optimizers. As such a use of evolutionary optimization results in favorable outcome but in a longer period of time when compared to conventional

optimizers. However, on exploring the configurations and trade off of the sample space, the answer is straight forward where conventional optimizer fails to respond.

6.2 Modern Theories and Extension

These allow the algorithm to utilize a cheap, readily available parallel processing capability running variable time iterative solvers on desktop computers, through asynchronous solution.

Allow for the exploitation of variable fidelity or multi-physics solvers through a hierarchical population topology.

Be applied to more varied types of engineering problems in one or many objectives through Pareto tournament selection.

6.2.1 Game Theory

Aerodynamic optimization cannot be posed as an unconstrained optimization problem and is mostly posed as a multi-objective function. To this end a number of approaches have been developed for use in evolutionary algorithms, and the two considered are:

- Pareto Fronts: Proposed by Vilfredo Pareto, a solution to a problem is found as an optimal set, called the Pareto set, using a cooperative game spanning over the range of designs.
- Nash equilibria: Proposed by John F. Nash, a Nash equilibrium point is the position in a competitive (or non-cooperative) game whereby no player can improve his position at the expense of the other, which each player optimizing one fitness function over a subset of the objective variables.

6.1.1.1 Pareto Front

The Pareto Front is applicable to a wide range of objective functions and provides great insight in the variation of the design for each design objective. A Paerto Optimal Set is a set of solution which are not influenced by corresponding points in a search space or they influence every solutions except other Pareto Optimal Set.

The non-dominated approach is comparatively versatile as it is equally applicable to both single and multi-objective optimization. The problem with sorting approaches is that the method is not a fully integrated one. Briefly, a sorting method works by computing the set of non-dominated solutions amongst a large statistical sampling either a large population or previous data and assigning these solutions rank 1. Then ignoring these points, the process is repeated until a 'second' Pareto front is found, and this is assigned rank 2. This process continues until all points are ranked and then the value of the rank is assigned to the individual as a now single objective fitness.

6.3 Problem Formulation

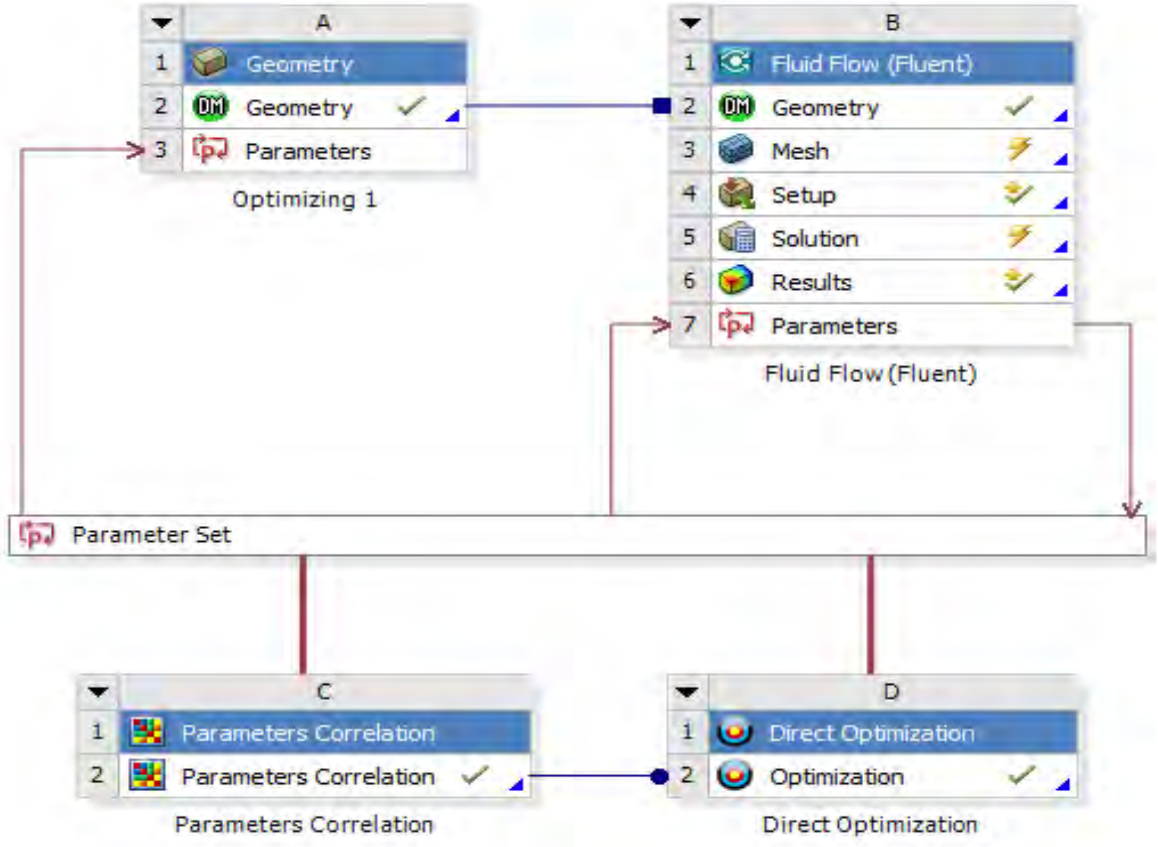

Figure 36: Parameter Correlation and Optimization Schematics

Figure 35 above represents a schematic view of how the parameter correlation and optimization process is conducted. To reduce the number of design of experiments, 14 design variables are considered which are constrained to 10% increment and decrement from its norm. The chord and twist at 7 different radial span location is considered for design variable with the torque subjected as objective output function. The study is conducted at the cut in wind speed of 5 m/s. Wind speed is maintained constant thorough out the correlation study and optimization. However, optimum blade is tested at different wind conditions as per Sequence S test series.

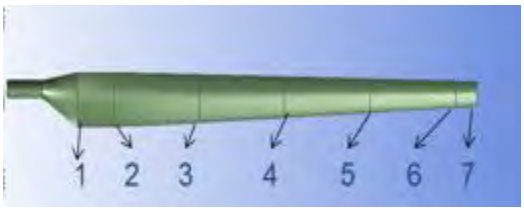

	A	B
1		Enabled
2	Parameters Correlation	
3	Input Parameters	
4	Optimizing 1 (A1)	
5	P1 - Scale_1	☑
6	P2 - Twist1	☑
7	P3 - Scale2	☑
8	P4 - Twist2	☑
9	P5 - Scale3	☑
10	P6 - Twist3	☑
11	P7 - Scale4	☑
12	P8 - Twist4	☑
13	P9 - Scale5	☑
14	P10 - Twist5	☑
15	P11 - Scale6	☑
16	P12 - Twist6	☑
17	P13 - Scale7	☑
18	P14 - Twist7	☑
19	Output Parameters	
20	Fluid Flow (Fluent) (B1)	
21	P15 - Moment	

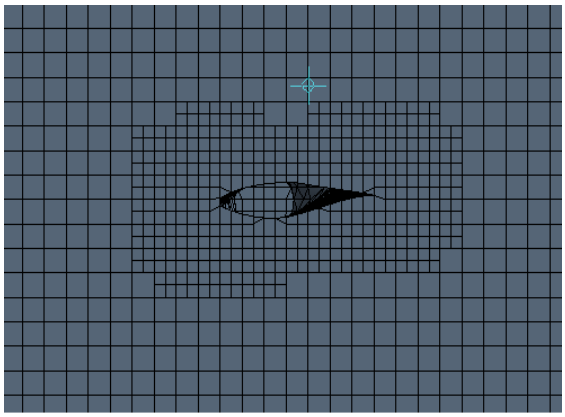

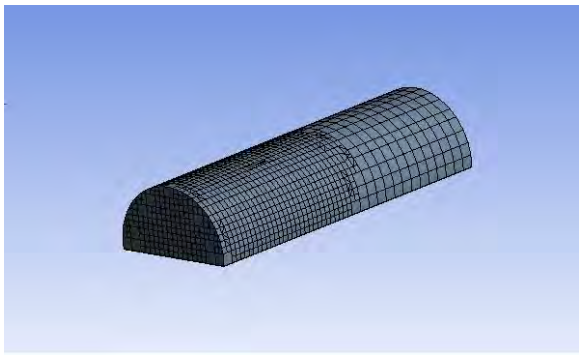

Figure 37: Design Variables and Automated Mesh for Optimization

7. Parameter Correlation

An increase in the assigned design variables decreases the overall efficiency of optimizing analysis process but under uncertainty conditions, the effects of individual design variable on overall analysis cannot be ascertained. Focusing on the more important variable and excluding the lesser important ones reduce the generation of unwanted sampling space without much effect on the objective outcome. Parameter correlation thus helps in identifying the effect of input variables to the outcome and also determines how sensitive these variables are which govern the objective function.

The parameter correlation study was conducted with the following schematics:

Correlation type	= Spearman
Number of Samples	= 100
Mean Value Accuracy	= 0.1
Standard Deviation Accuracy	= 0.2
Convergence Check Frequency	= 15

The sample space converged at 4^{th} frequency check, which corresponds to 60 complete fluid simulations. Parametric correlation highlighted the optimization process to be quadratic rather than being linear.

7.1 Correlation Matrix and its Coefficient of Determination

Correlation Matrix defines the relation between variables and their effectiveness. The problem formulation defines whether the relation is quadratic or linear.

7.1.1 Linear Correlation Matrix:

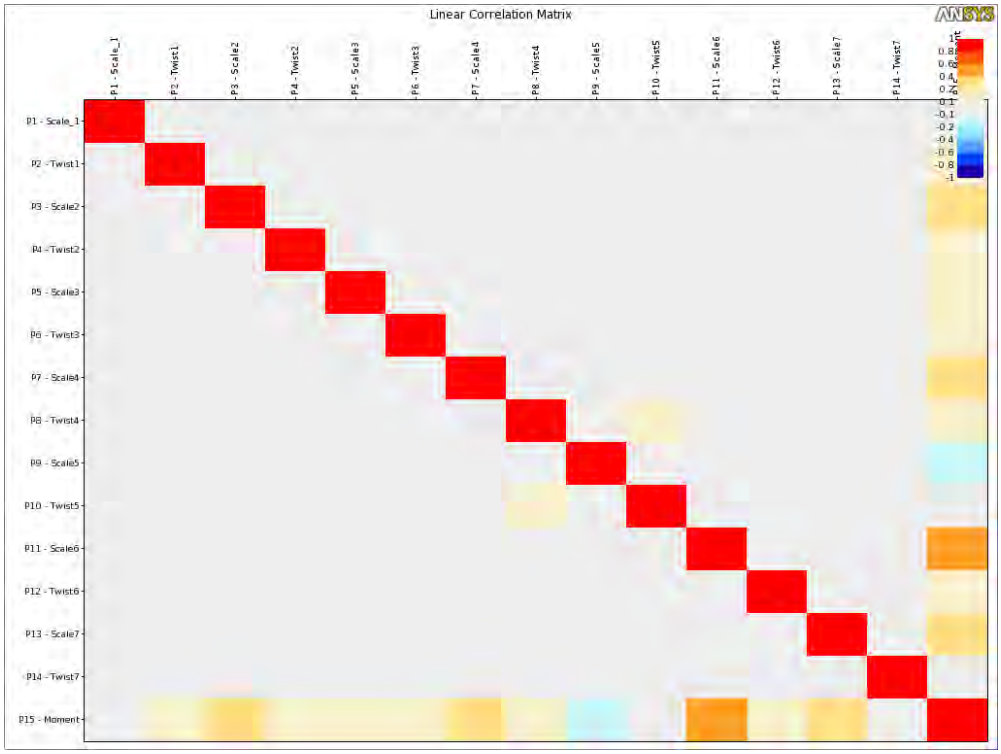

Figure 38: Linear Correlation Matrix

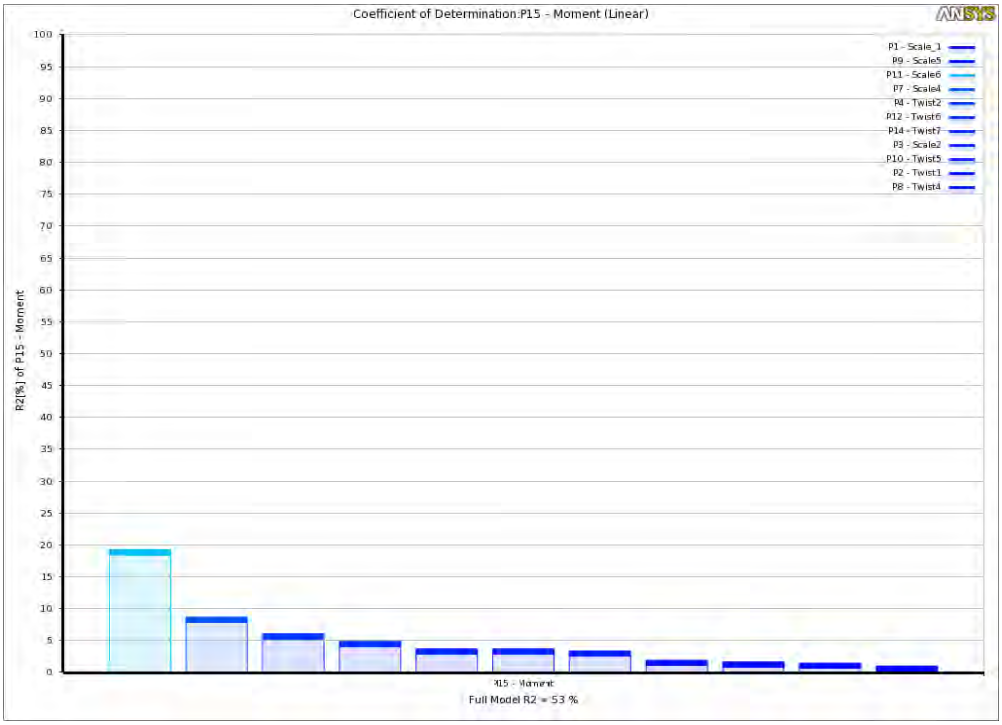

Figure 39: Coefficient of Determination (Linear)

The linear correlation matrix indicates a strong relation along the diagonal and each of these is the major inputs that drive the outcome parameter. The visual rendering of the matrix display symmetry along the diagonal as well. Whereas, Determination of the matrix indicates that the relation of the design variable only contributes to 53.177 % of the outcome function. This is well explained with the use of linear scatter graph displayed in section 8.3. The linear trend line of the scatter plots shows a very few design variables lying around or on the line. These scatter of variable around the trend line displays the optimum design variables. Thus, dictating that the parametric relation between the variables and their objective function is least linear.

7.1.2 Quadratic Correlation Matrix

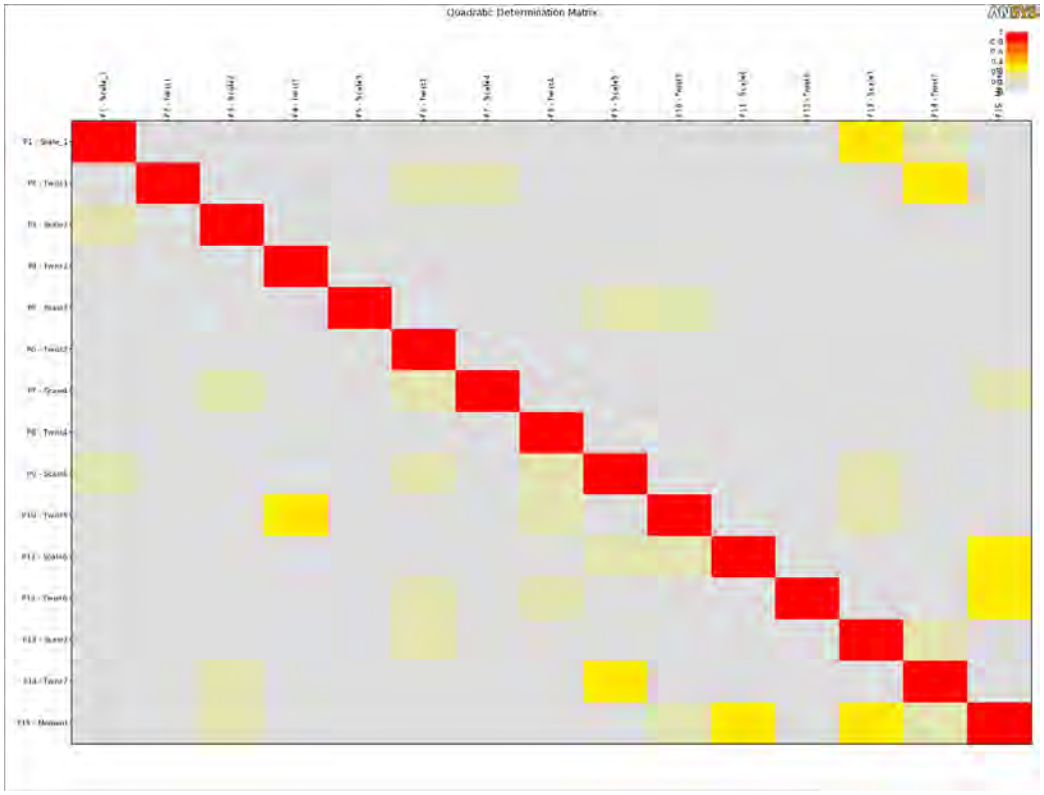

Figure 40: Quadratic Determination Matrix

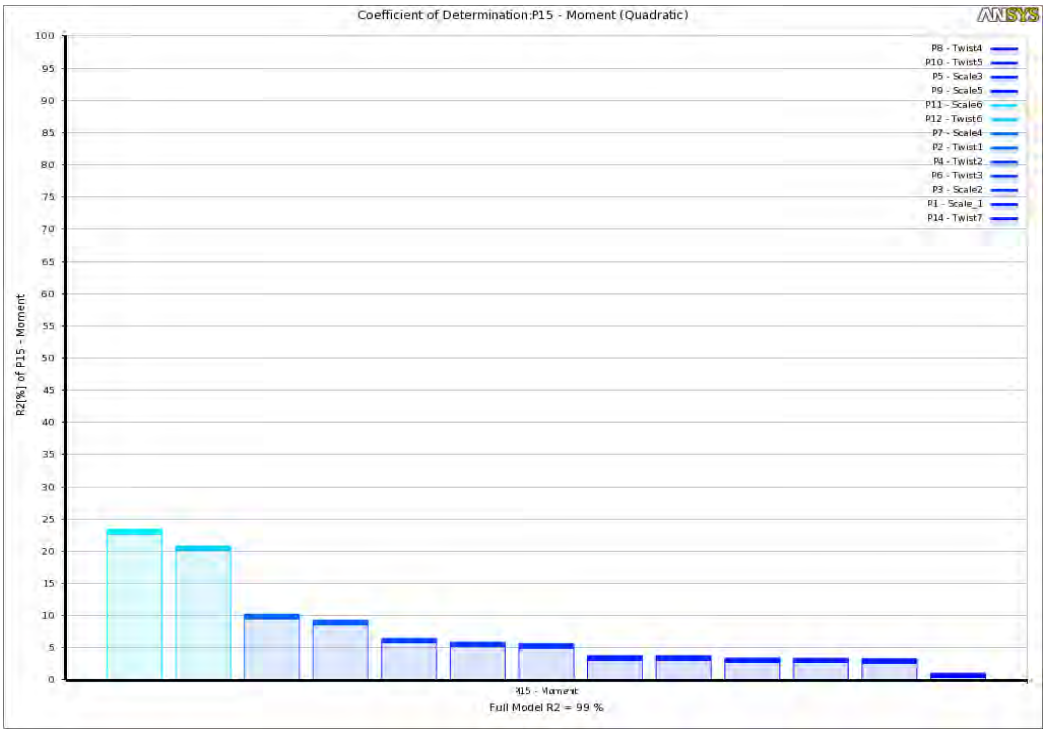

Figure 41: Coefficient of Determination (Quadratic)

Unlike the Linear Correlation, the Quadratic Correlation indicates the problem statement as more quadratic. Determination histogram strongly influence that objective function is greatly dependent on the design variables and correlation scatter of the variable parameters in section 8.3 supports this claim with more number of optimum points along the quadratic trend line. Full model relation is at 99.136% indicating that the objective function is strongly influenced by the variations in input design variables.

7.2 Sensitivity Analysis

Sensitivity analysis shows how sensitive the objective function outcome is to variation to input design variables. Parameter P1 is least sensitive while, parameter P9 and P14 have negative sensitivity to objective function. The root chord, irrespective of changes in its dimension does not contribute to equivalent change in the torque generated while increase in chord at station 5 and twist angle at station 7 decreases the torque produced. However, chord at station 5 has a higher negative relation with the produced torque than twist at station 7.

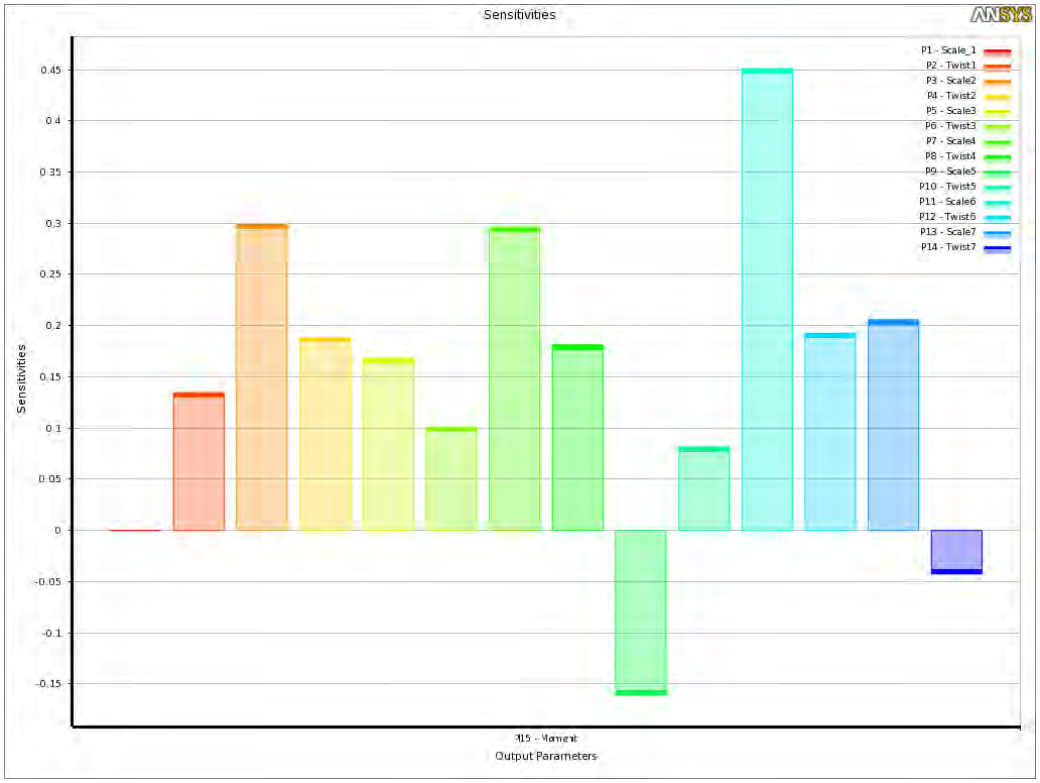

Figure 42: Sensitivities of Design Parameters to Torque

7.3 Graphs of Correlation Scatter

The Correlation Scatter plots individual design variable against torque. The optimum of these scatter points lay around the trend line. The following are the Correlation Scatter of parametric study;

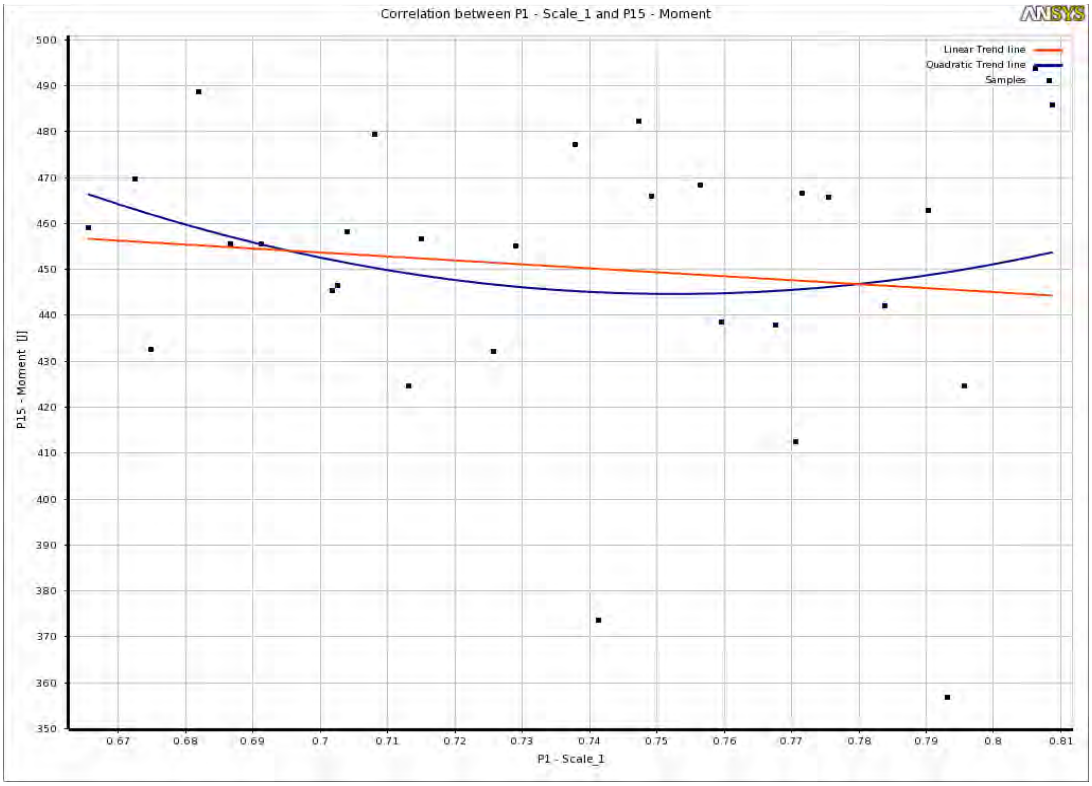

Figure 43: Correlation Scatter Scale 1

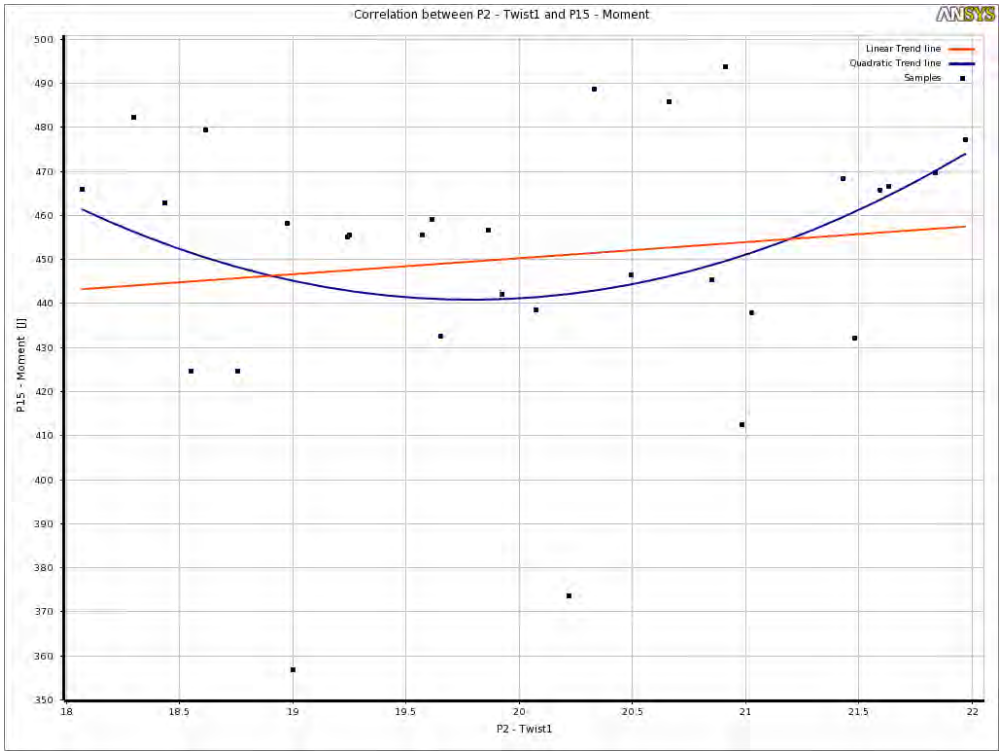

Figure 44: Correlation Scatter Twist 1

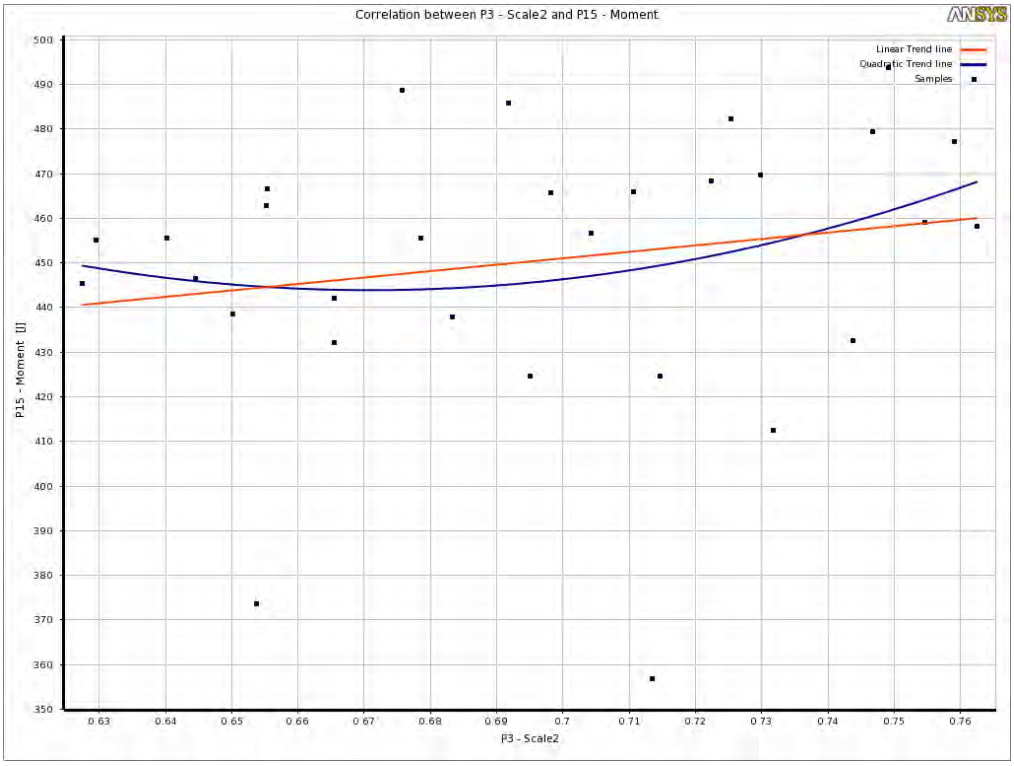

Figure 45: Correlation Scatter Scale 2

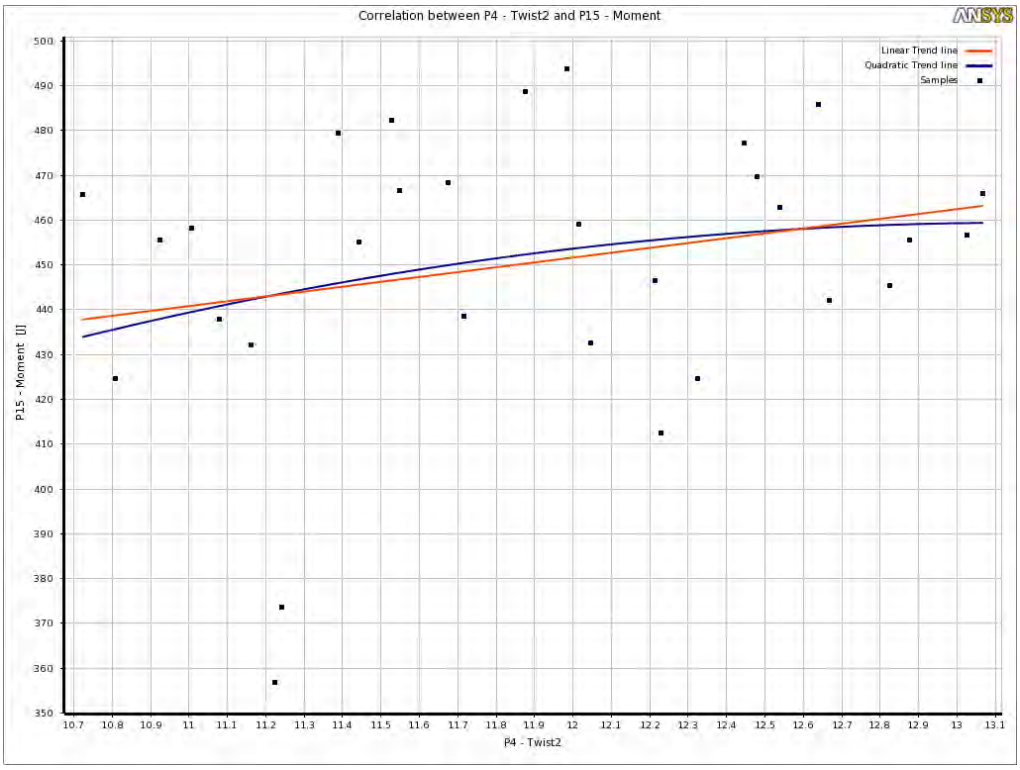

Figure 46: Correlation Scatter Twist 2

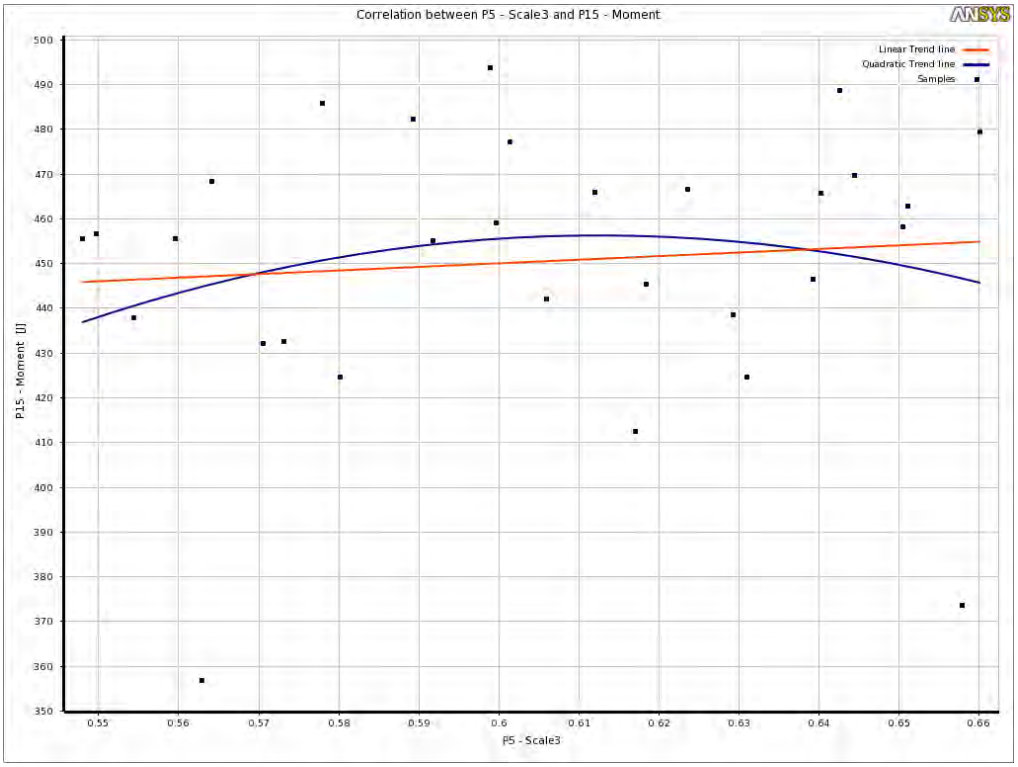

Figure 47: Correlation Scatter Scale 3

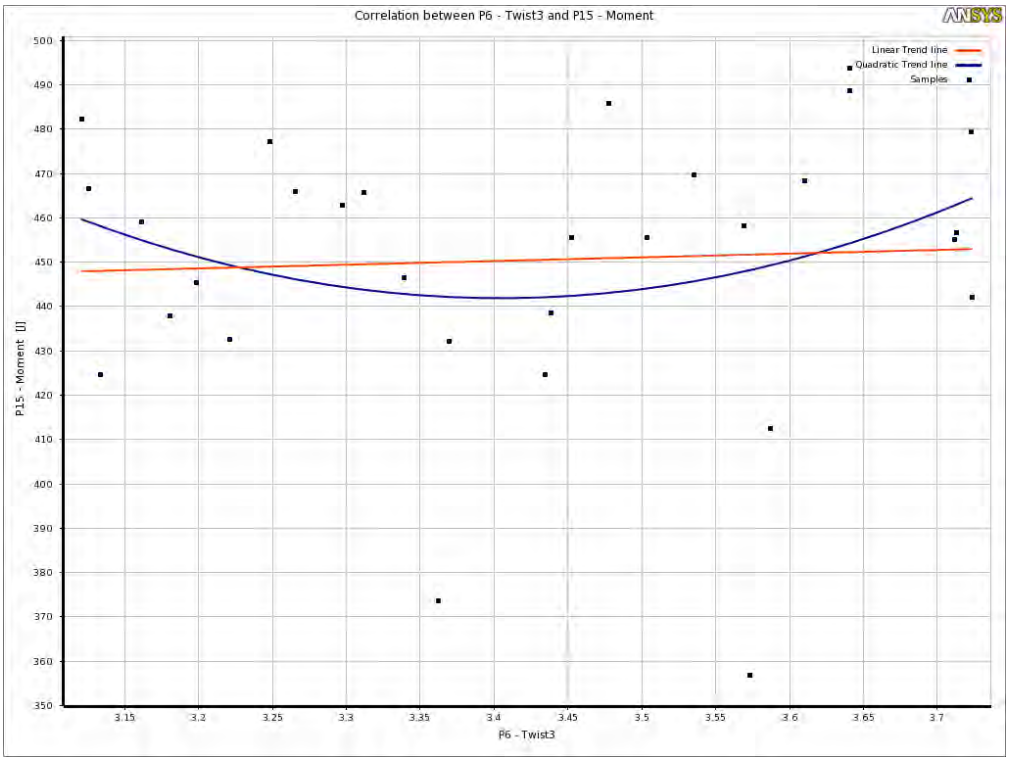

Figure 48: Correlation Scatter Twist 3

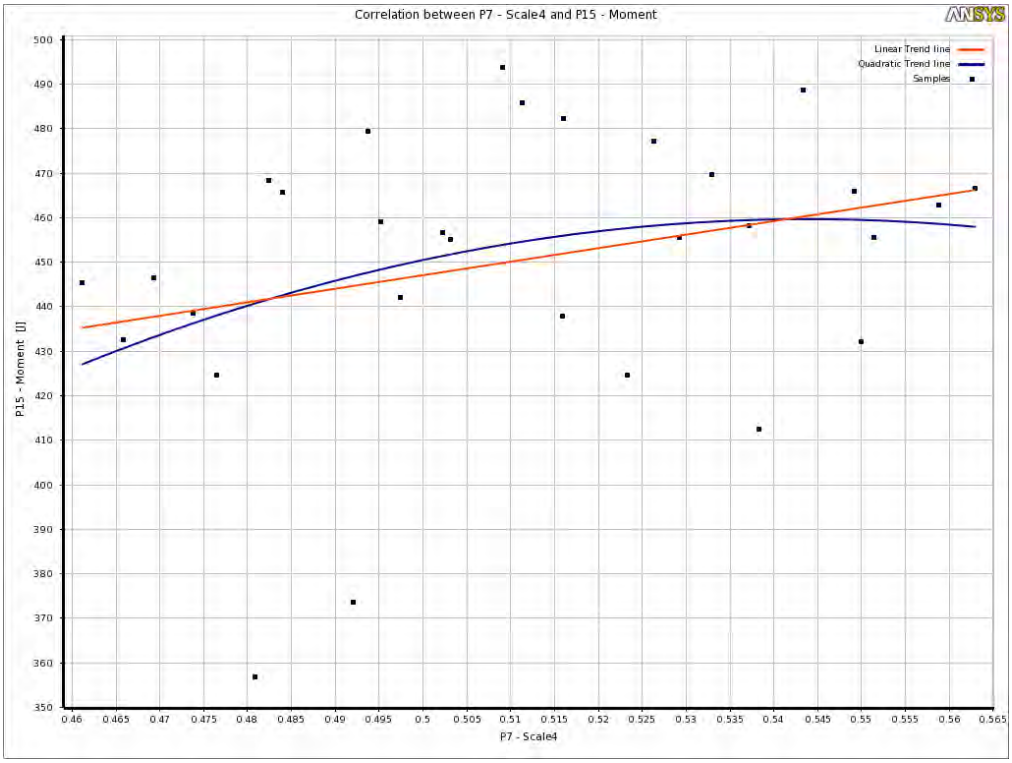

Figure 49: Correlation Scatter Scale 4

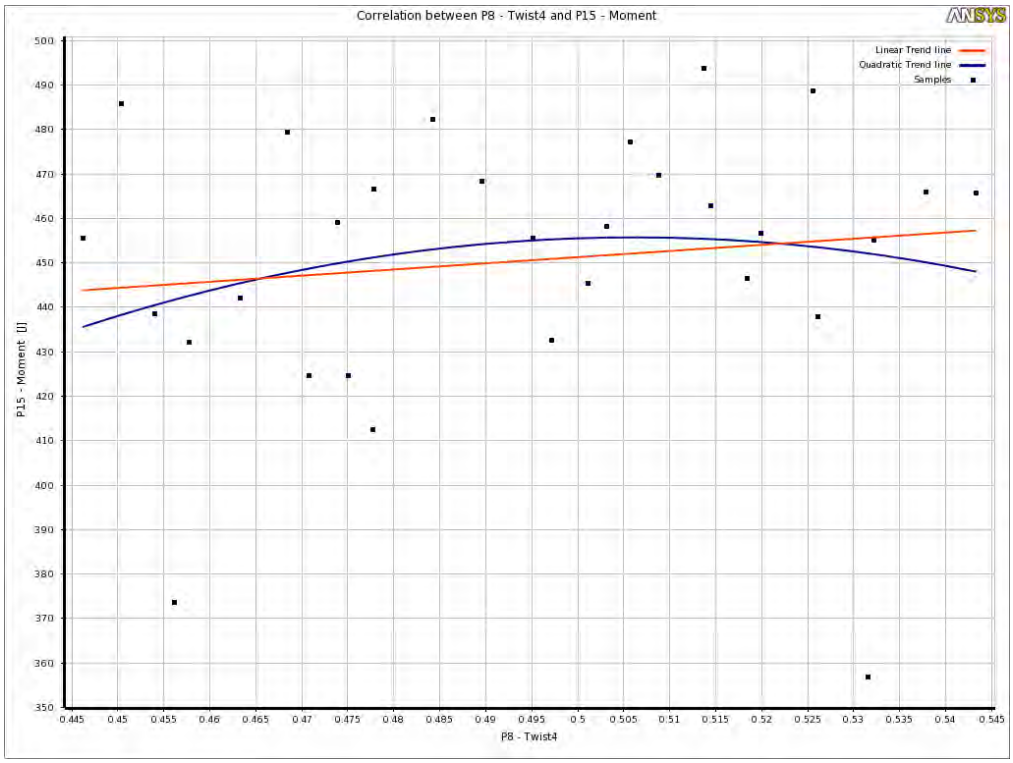

Figure 50: Correlation Scatter Twist 4

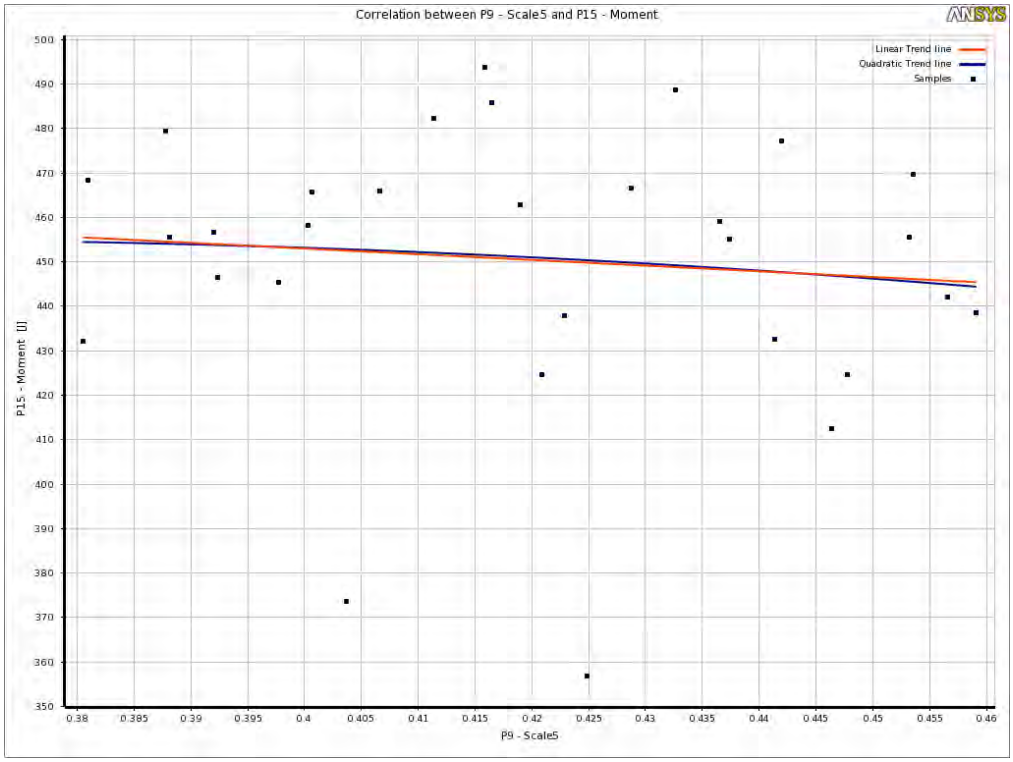

Figure 51: Correlation Scatter Scale 5

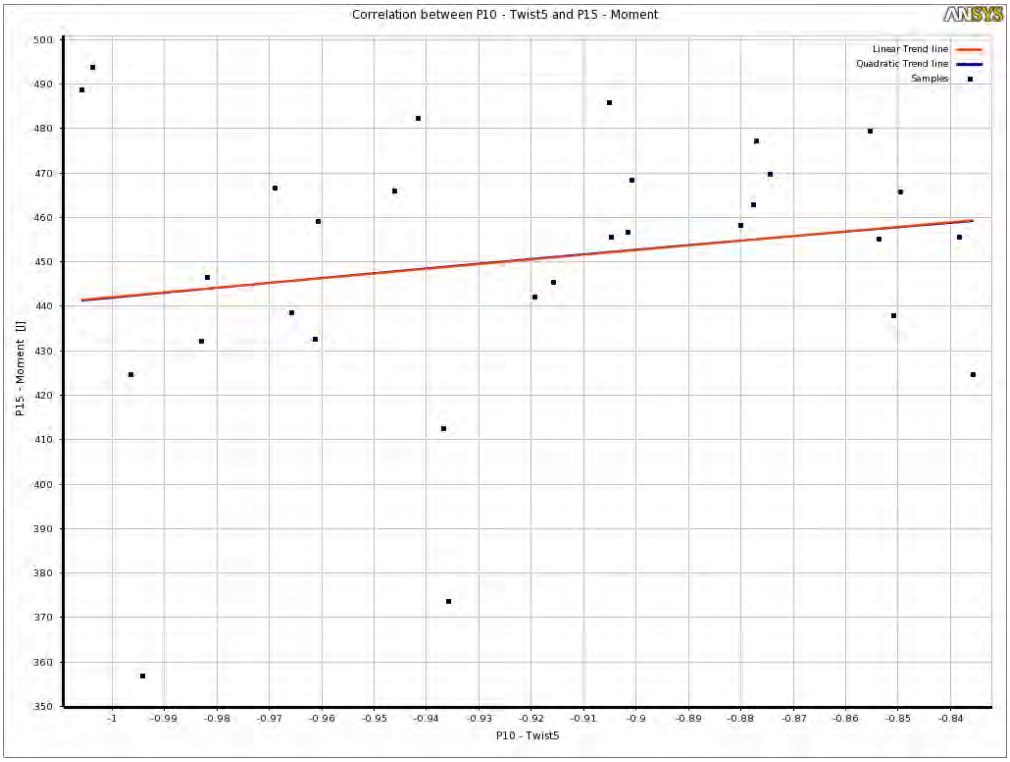

Figure 52: Correlation Scatter Twist 6

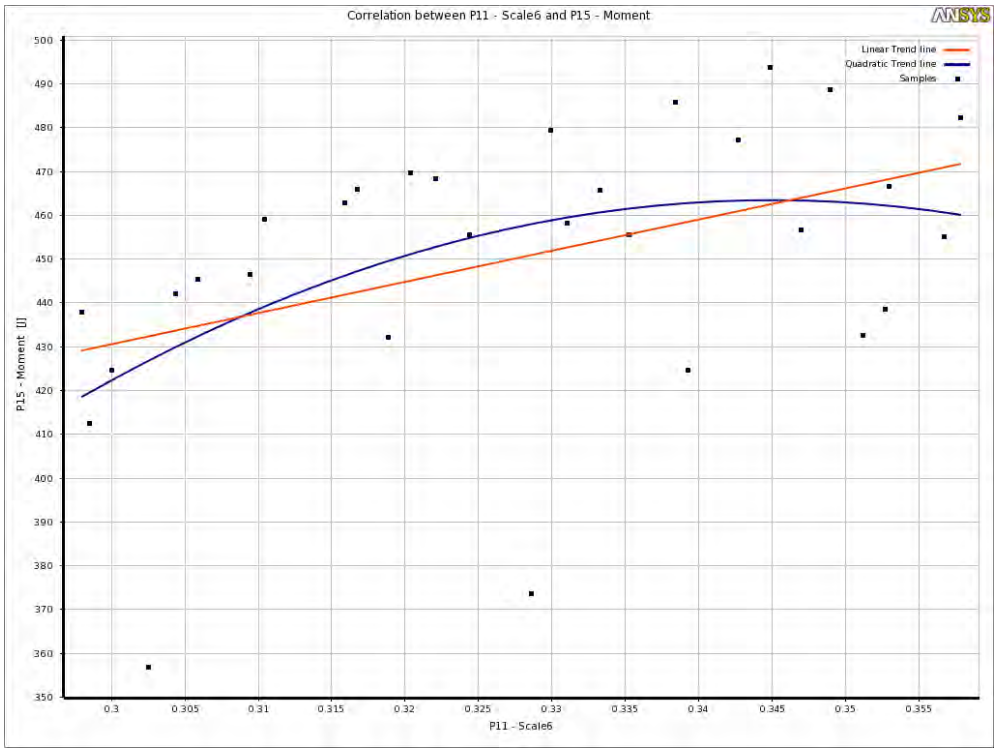

Figure 53: Correlation Scatter Scale 6

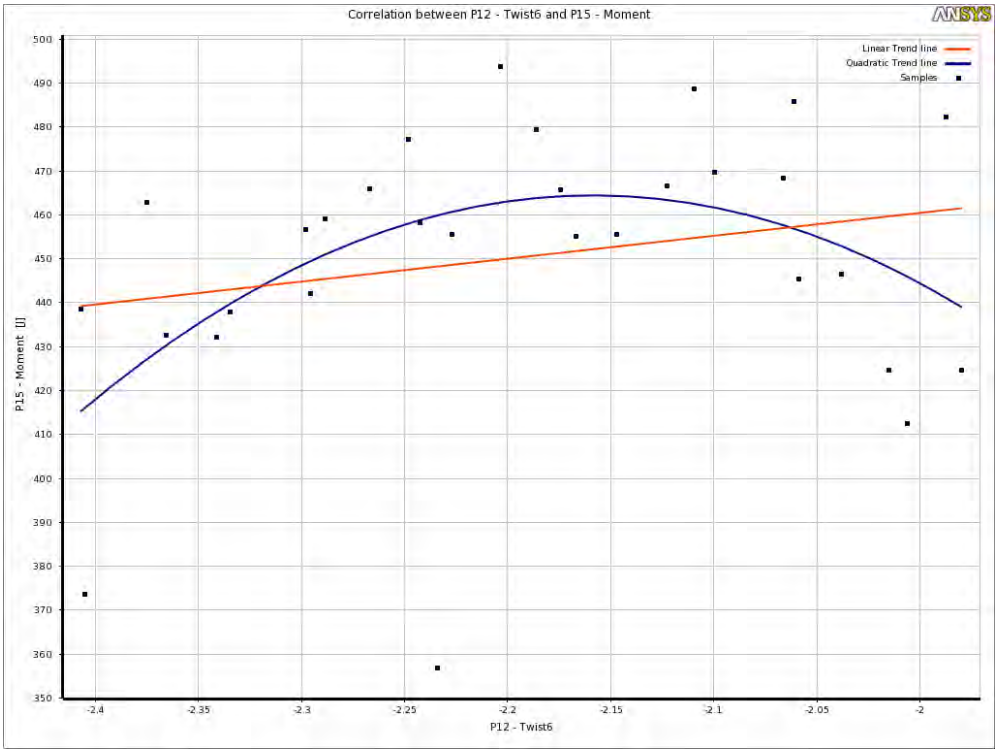

Figure 54: Correlation Scatter Twist 6

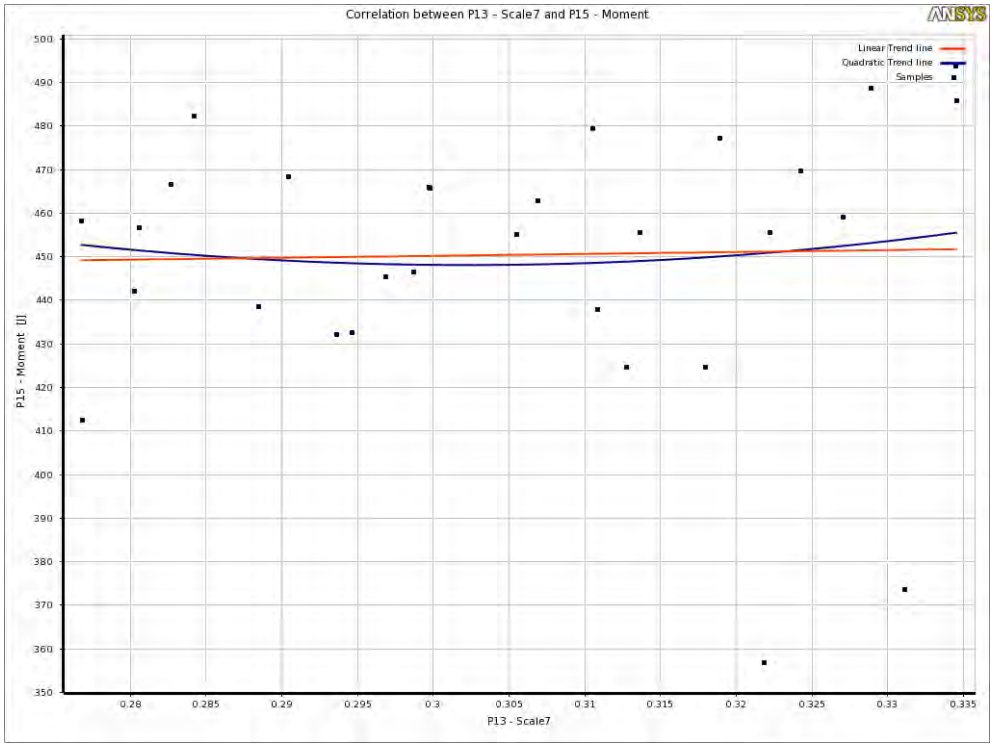

Figure 55: Correlation Scatter Scale 7

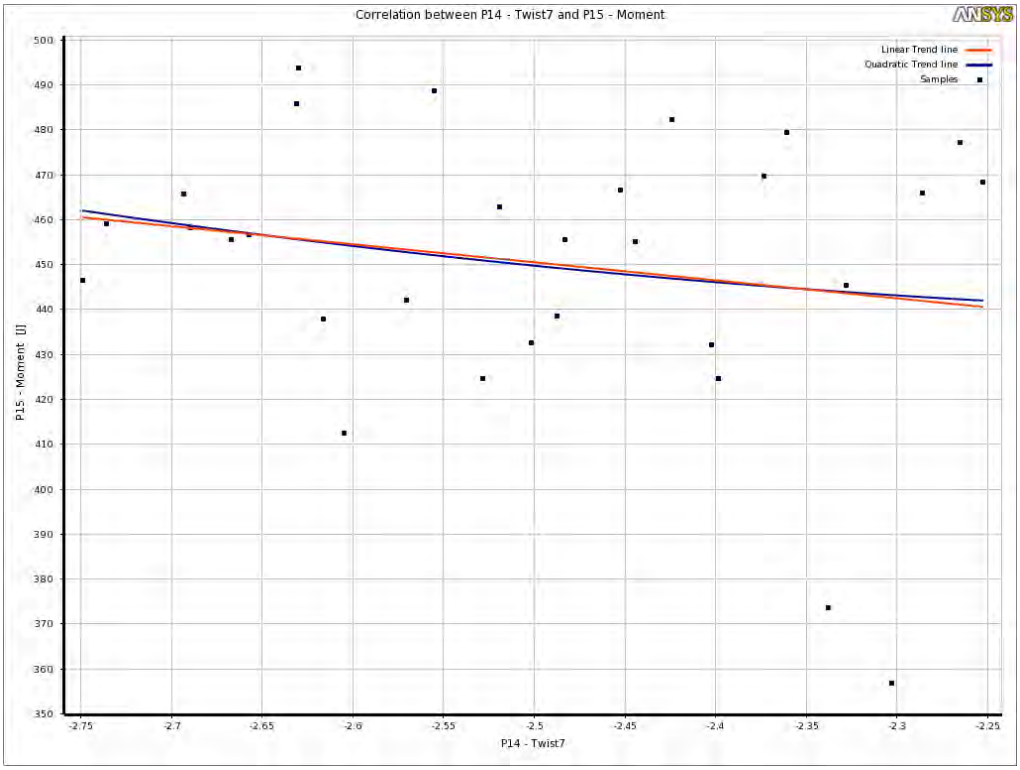

Figure 56: Correlation Scatter Twist 7

8. Optimization

The direct optimization method can extract information of design variables from component systems which contain these data points. Since the parametric correlation implied the lack of effectiveness of the root chord on the torque generated, it is appropriate not to consider it as a design variable. This considerably reduces the sample data design points generated, since the direct optimization relies on real solves. The problem statement comprises of a single objective function, thus Adaptive Single Objective Optimization method is employed. This method of optimization implements an automatic intelligent refinement of points to provide a global optimum and is a gradient based method. Table 7 shows the upper and lower bound of the design variable.

Table 6: Sample Point Domain Space

	Optimization Domain	Lower Bound	Upper Bound
1	Twist – 1	18.036	22.044
2	Chord – 2	0.6273	0.7667
3	Twist – 2	10.718	13.1
4	Chord – 3	0.5445	0.6655
5	Twist – 3	3.0825	3.7675
6	Chord – 4	0.4608	0.5632
7	Twist – 4	0.4446	0.5434
8	Chord – 5	0.378	0.462
9	Twist – 5	-1.012	-0.828
10	Chord – 6	0.2952	0.3608

11	Twist – 6	-2.4101	-1.9719
12	Chord – 7	0.2745	0.3355
13	Twist – 7	-2.75	-2.25

8.1 Statistics of Optimization

Optimization Method = Adaptive Single Objective Method

Number of LHS Initial Samples = 105

Number of Screening Samples = 105

Number of Starting Points = 105

Maximum Number of Evaluations = 300

Maximum Number of Domain Reduction = 20

Percentage of Domain Reduction = 0.25

Maximum Number of Candidates = 5

Lower and Upper bound = 430 and 550

8.2 Optimum Result through Pareto Front

A total of 105 design points were generated. After the end of 105 simulations, the automatic intelligence further refines the search to obtain the global optimum with domain reduction to a maximum of 300 simulations. If the optimization fails to find a

global optimum with the specified number of evaluations then a convergence to find that global optimum fails but a local optimum is still found. These species of sample points are classified as per the Pareto Front. Figure 39 displays the sample space using Pareto Front.

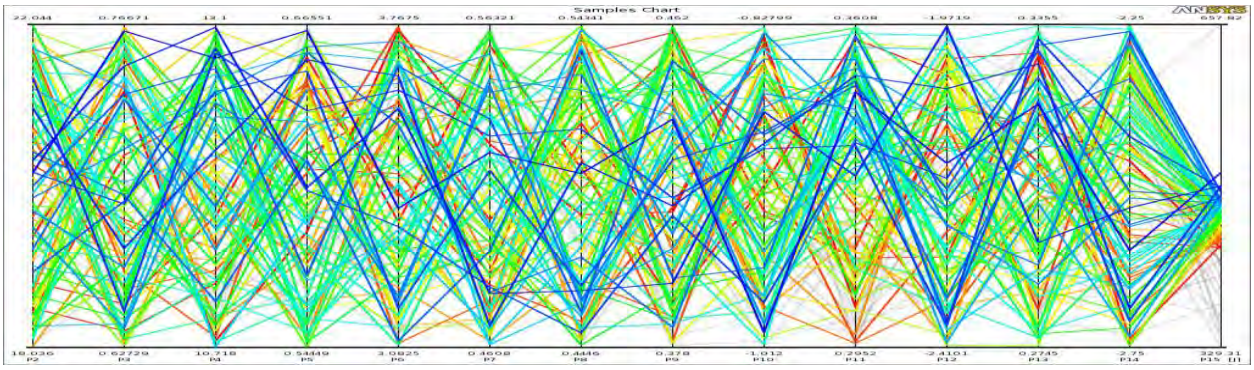

Figure 57: Sample Chart by Pareto Front

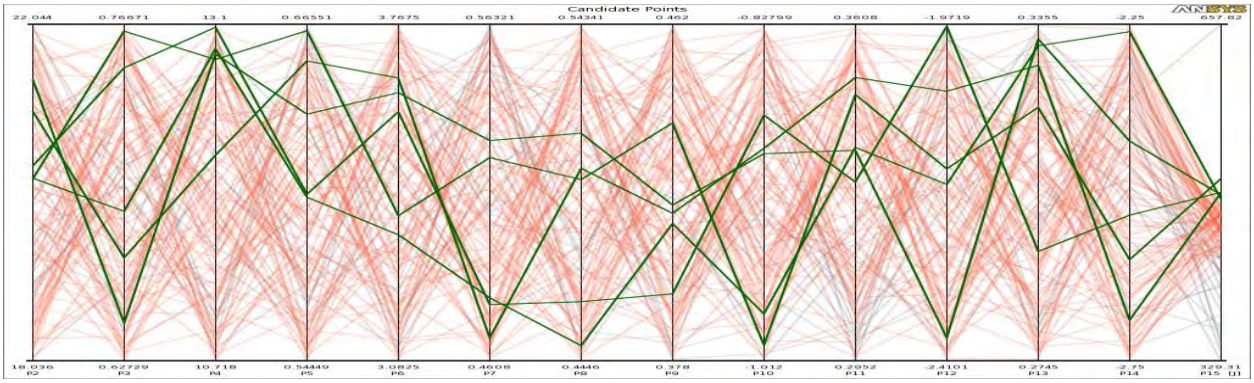

Figure 58: Candidate Points

Similar to Fig. 39, Fig. 40 highlights the best candidate points with a green line. Fig. 41 represents the distribution of the design points with respect to the torque produced. The dashed lines represent the upper and lower bound of the objective maximum and minimum respectively, while red scatter line shows the corresponding torque produced when geometry of blade was altered as per the sample design space.

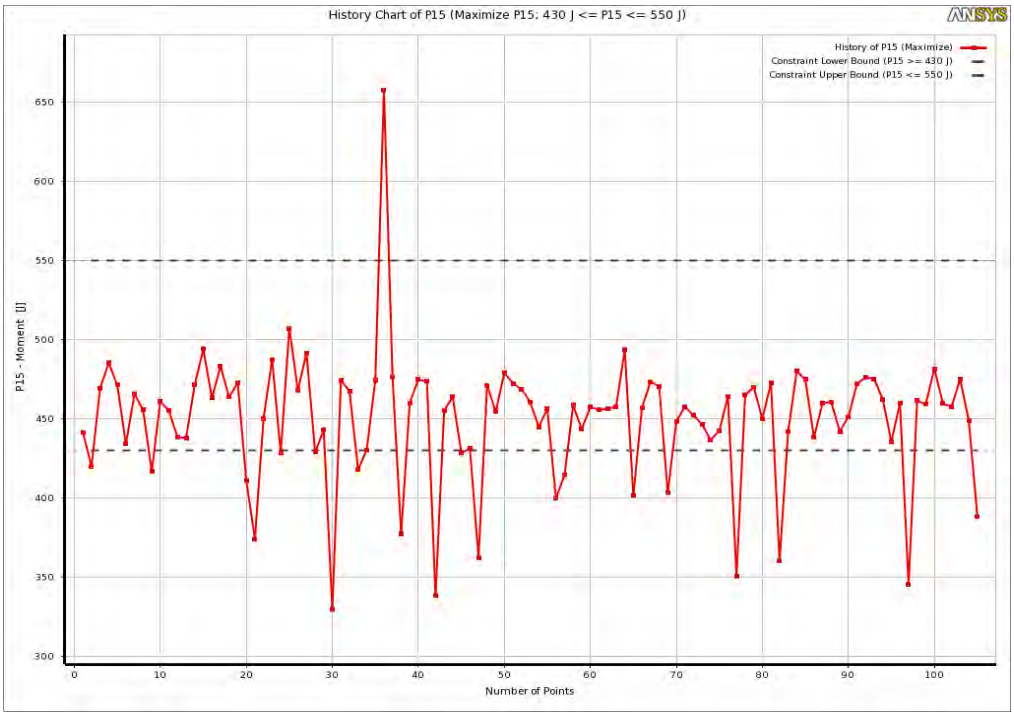

Figure 59: History of Torque

It is noticeable that a sample design variable produced torque well above the specified upper bound. This is due to an interruption during the optimizing phase. The solution of the specific sample space cannot be reiterated. Simulation conducted later for the sample space showed the torque to be average.

Table 7: Candidate Points

Optimization Domain	Best Candidate Points

		1	2	3	4	5
1	Twist – 1	20.205	20.36	21.013	21.391	20.216
2	Chord – 2	0.76406	0.74881	0.67001	0.64294	0.68929
3	Twist – 2	12.851	13.082	12.176	12.89	12.93
4	Chord – 3	0.66326	0.60448	0.65237	0.63323	0.6034
5	Twist – 3	3.3784	3.5904	3.6591	3.6288	3.3399
6	Chord – 4	0.52277	0.47801	0.46784	0.52785	0.48006
7	Twist – 4	0.4979	0.46198	0.50114	0.51145	0.44907
8	Chord – 5	0.43741	0.339476	0.41484	0.417	0.41237
9	Twist – 5	-1.0032	-0.87749	-0.89577	-0.89867	-0.98625
10	Chord – 6	0.34718	0.33007	0.35048	0.33632	0.33683
11	Twist – 6	-2.16	-1.9744	-2.0584	-2.3799	-2.1801
12	Chord – 7	0.32046	0.29439	0.32812	0.33286	0.33163
13	Twist – 7	-2.995	-2.5331	-2.6897	-2.4232	-2.2606

The optimization analysis concluded with a failure to obtain a global optimum with the maximum number of evaluations provided. However, best of 5 candidate points based on local optimum was found. Table 8, shows the 5 best candidate points which result in a significant higher torque generation, than the base line design. It would seem that, global optimum candidate could only be found if the percentage domain reduction was further reduced and when maximum numbers of evaluation points were to be increased. This would definitely increase the cost of computation and might only result in a slight improvement on the torque generated. Thereby, concluding that any further optimization

analysis by changing the evaluation parameter is unnecessary due to time restraint and heavy computational burden.

8.3 Tradeoff of Design Variables and its Plots

Tradeoff between torque and sample points of different design variables are displayed in the following scatter plots colored by Pareto Front. The hollow circle highlights infeasible points while, colored blocks signify the feasible region with darker shade of blue defining more suitable candidate points.

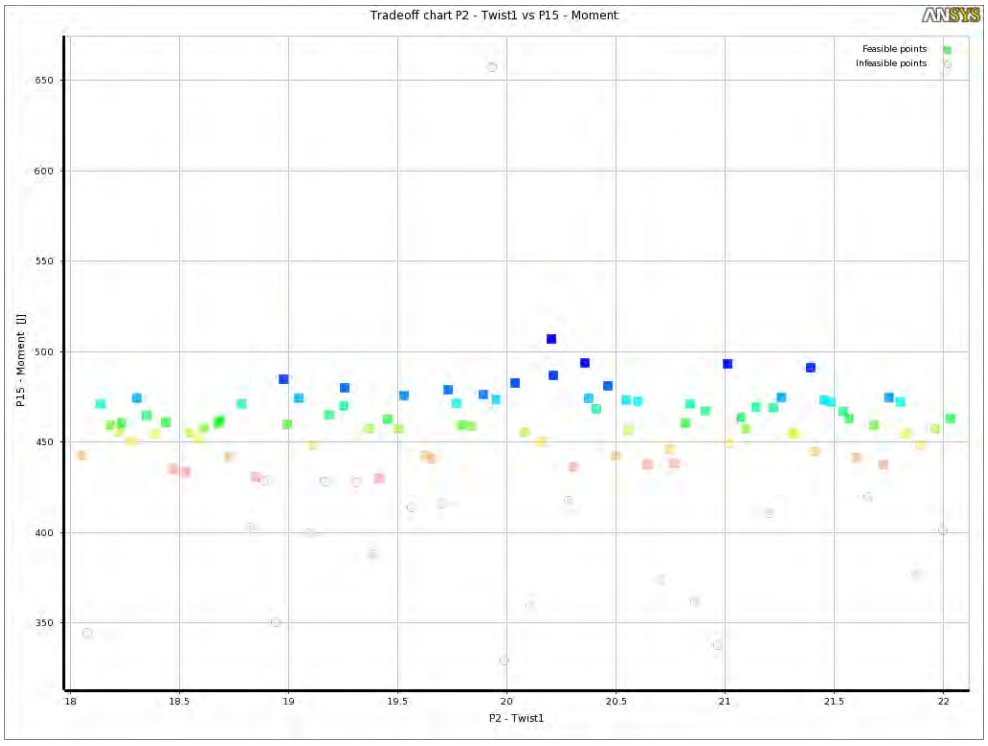

Figure 60: Tradeoff Twist 1

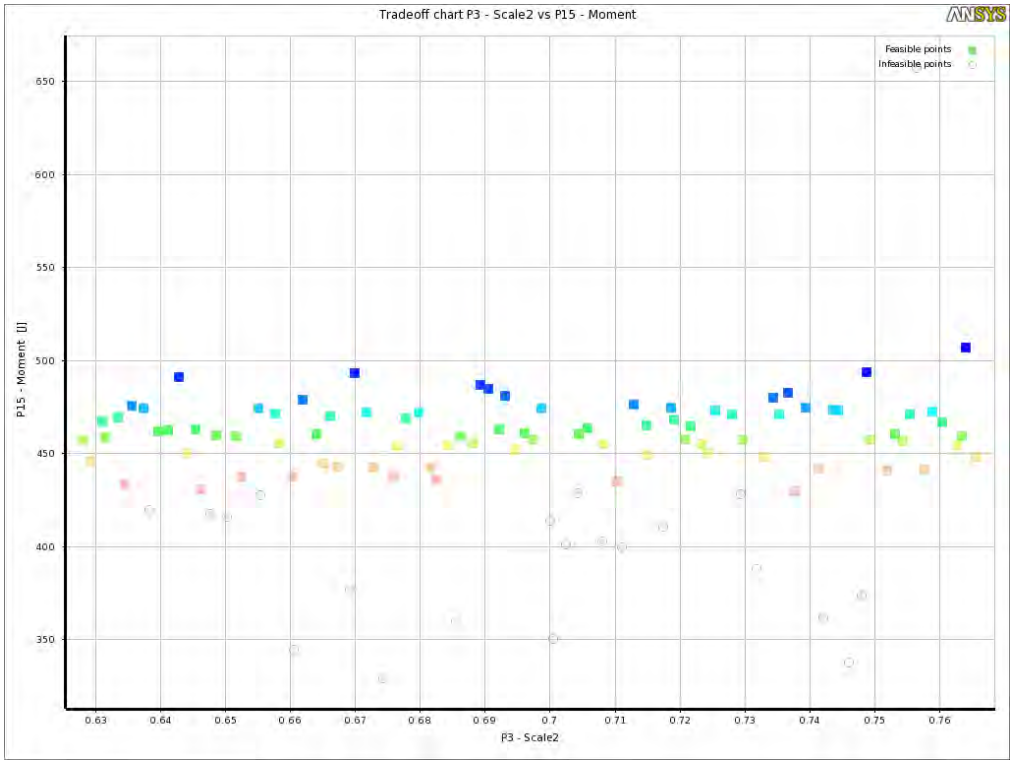

Figure 61: Tradeoff Scale 2

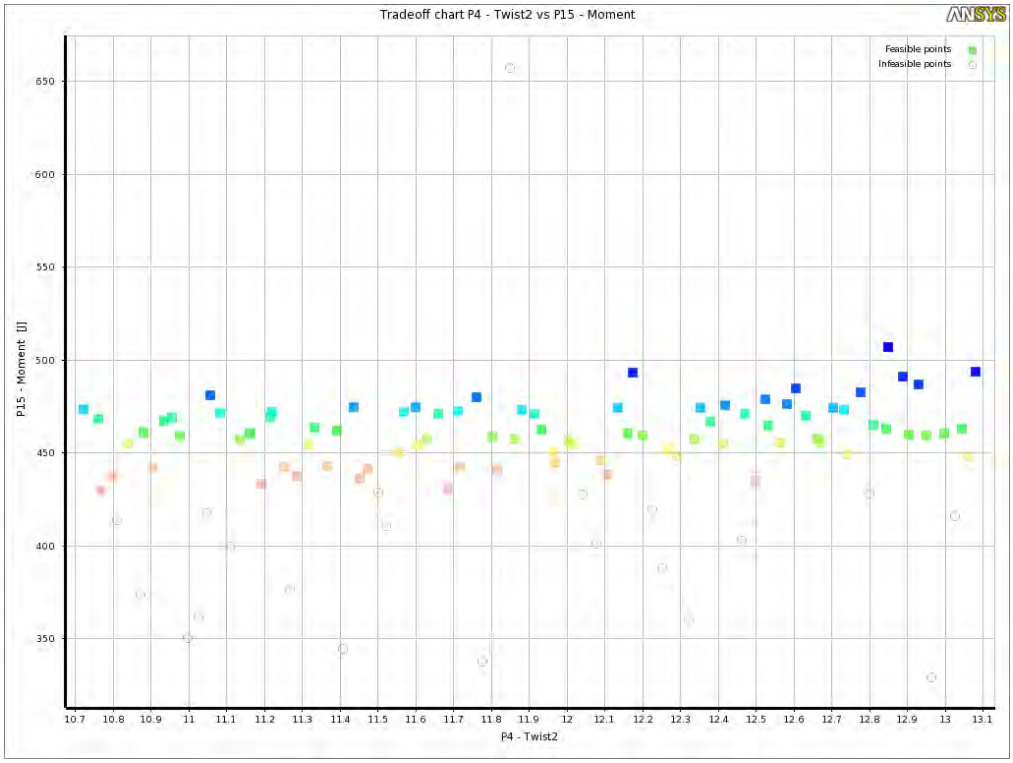

Figure 62: Tradeoff Twist 2

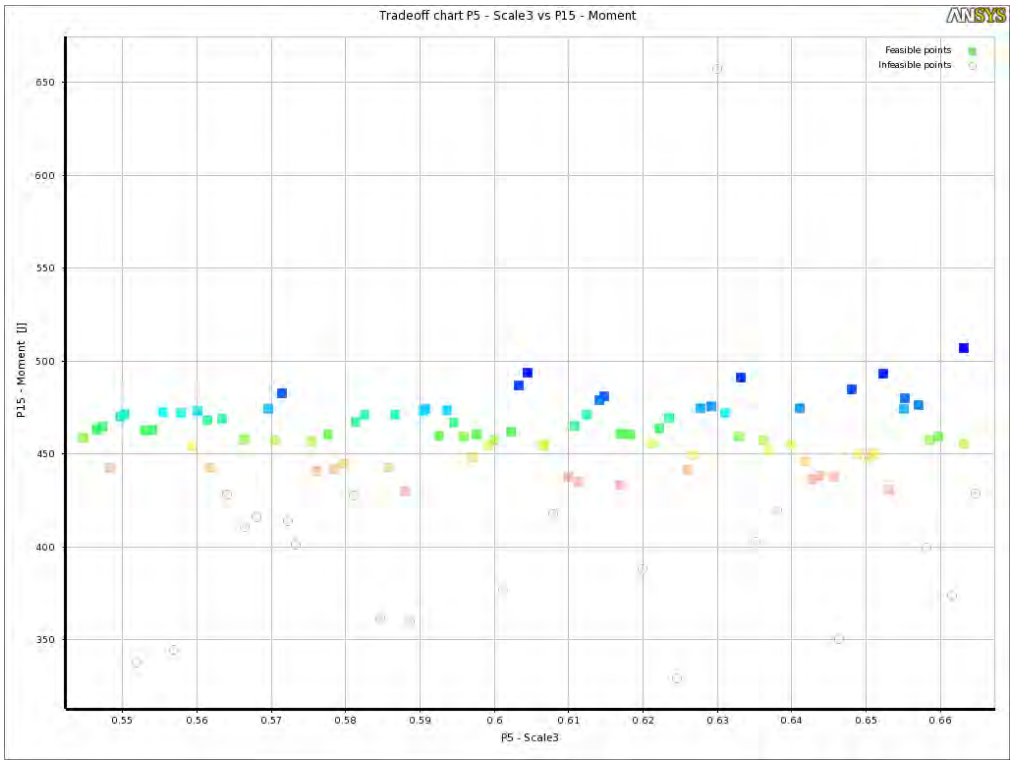

Figure 63: Tradeoff Scale 3

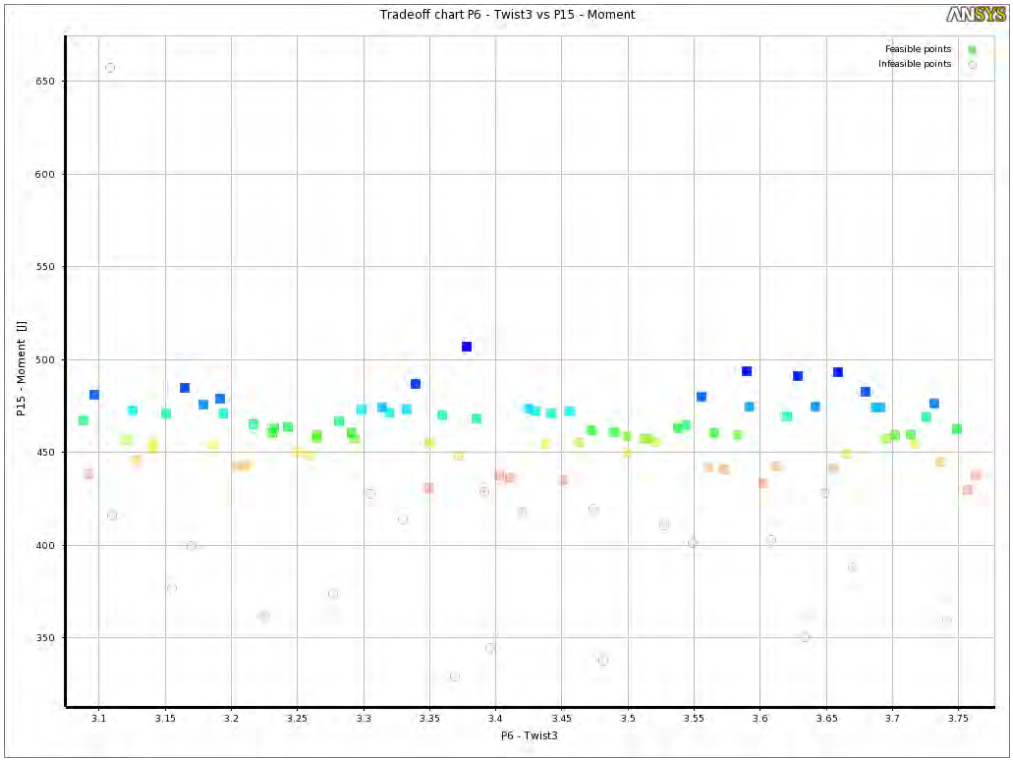

Figure 64: Tradeoff Twist 3

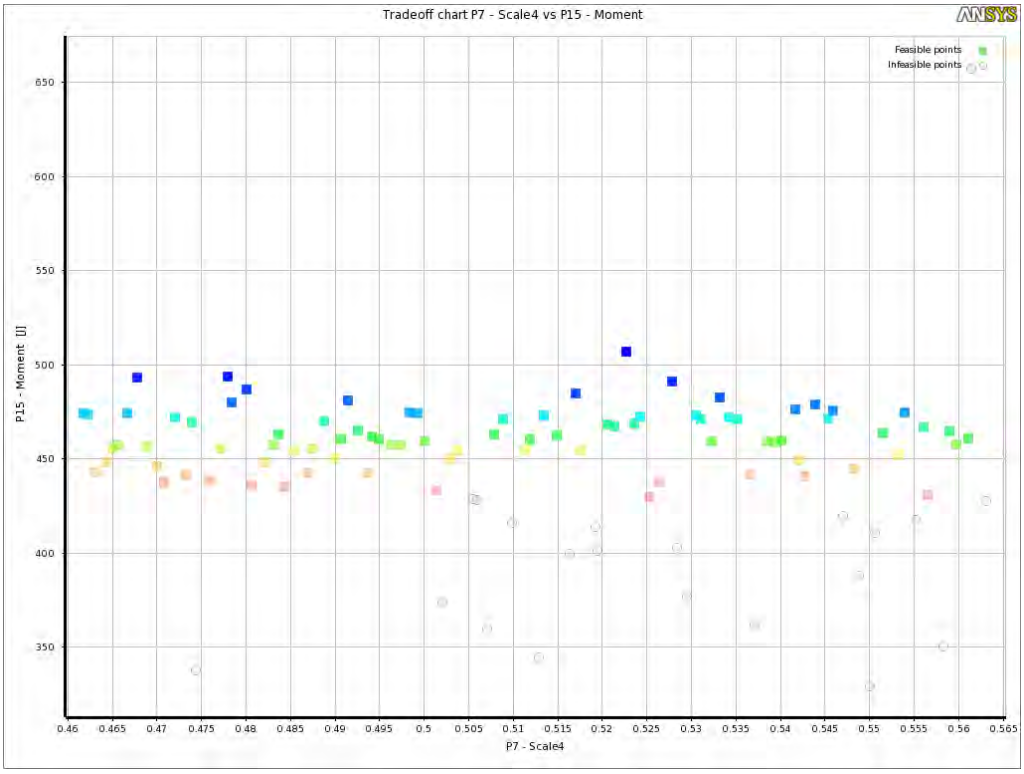

Figure 65: Tradeoff Scale 4

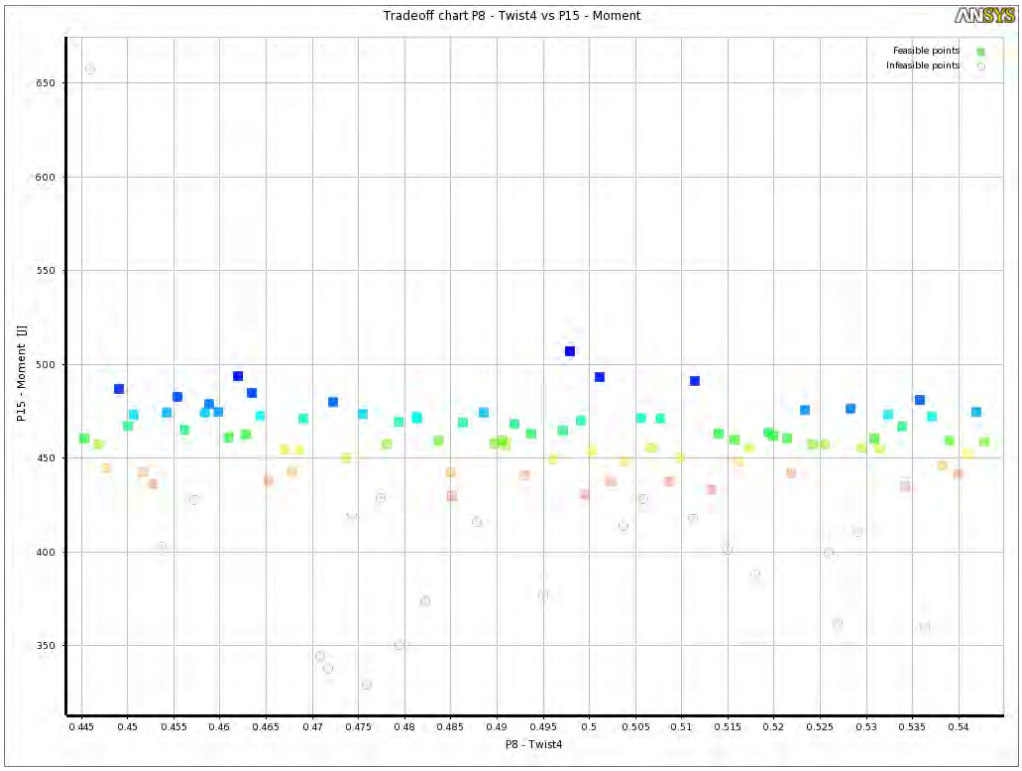

Figure 66: Tradeoff Twist 4

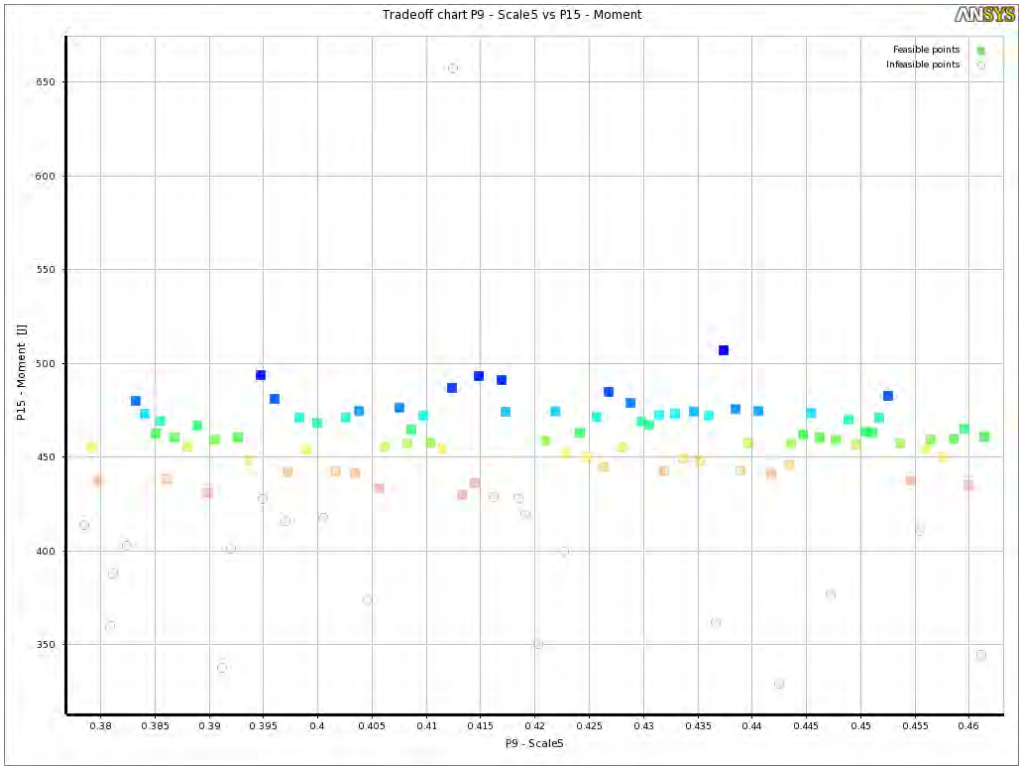

Figure 67: Tradeoff Scale 5

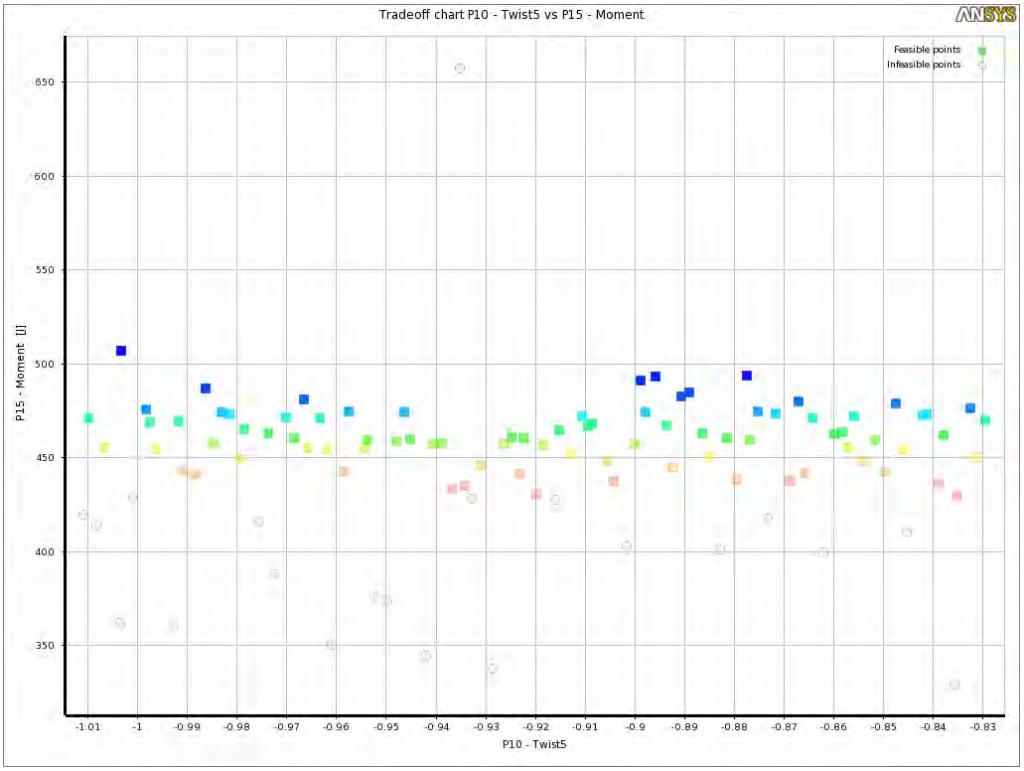

Figure 68: Tradeoff Twist 5

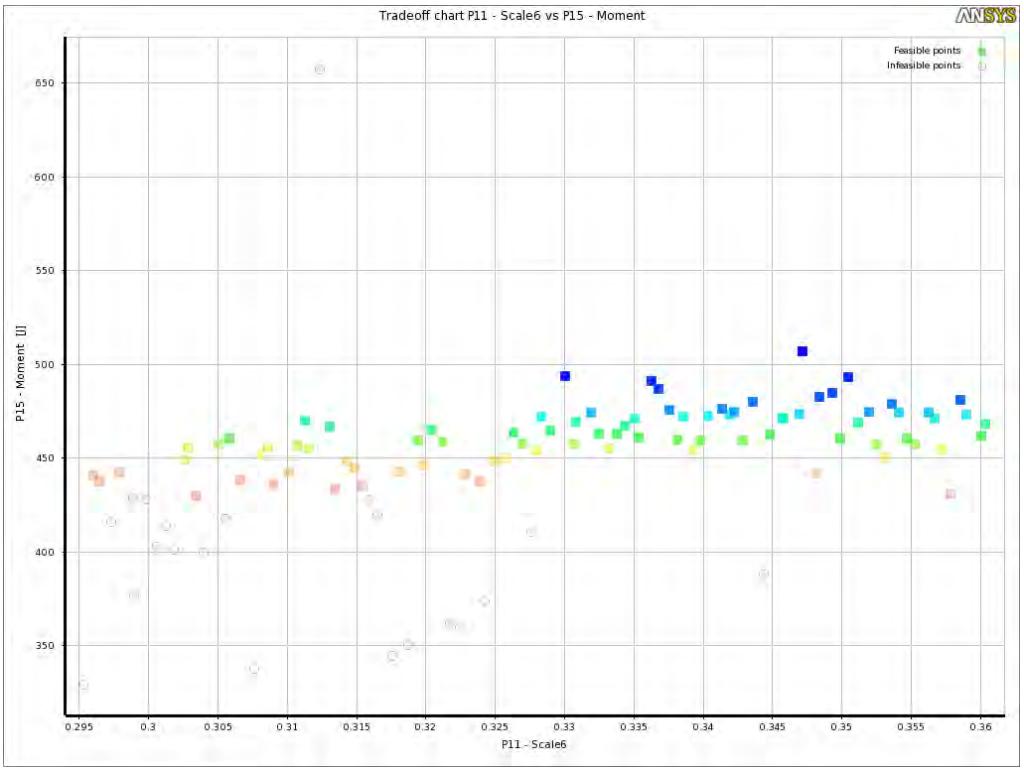

Figure 69: Tradeoff Scale 6

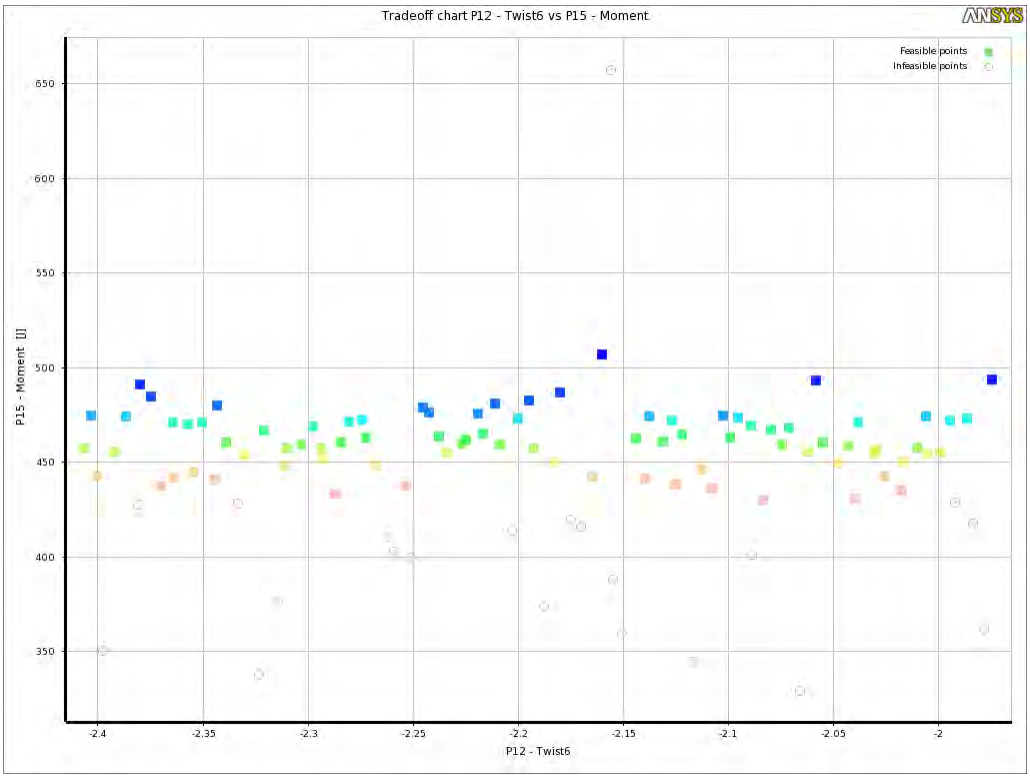

Figure 70: Tradeoff Twist 6

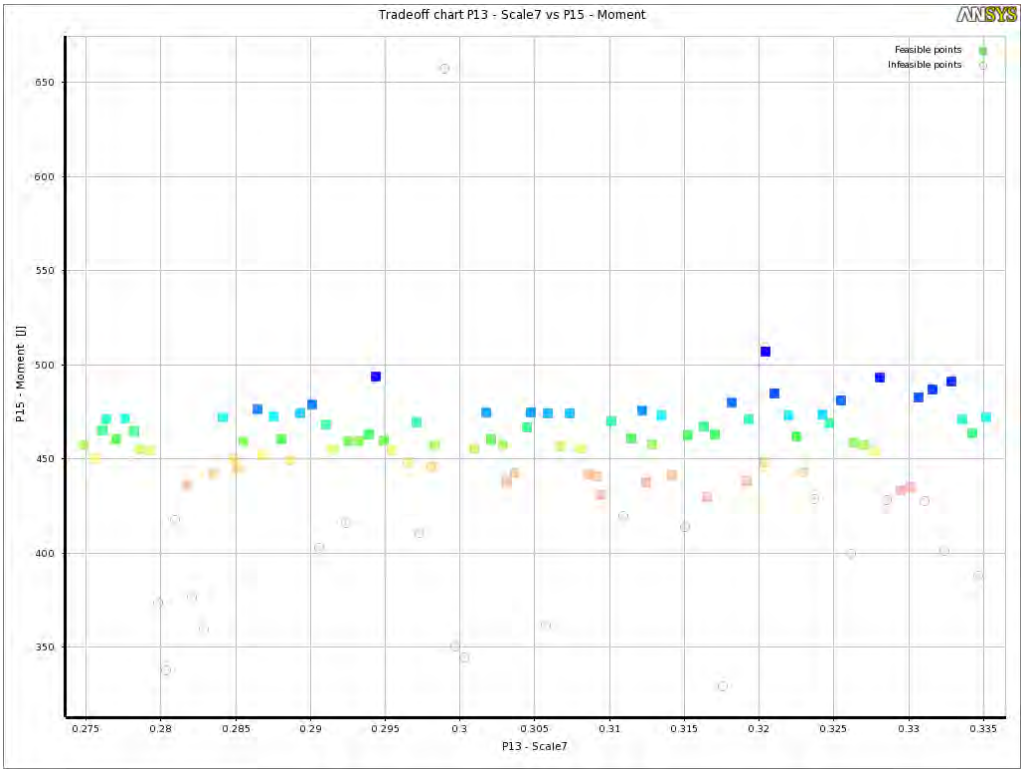

Figure 71: Tradeoff Scale 7

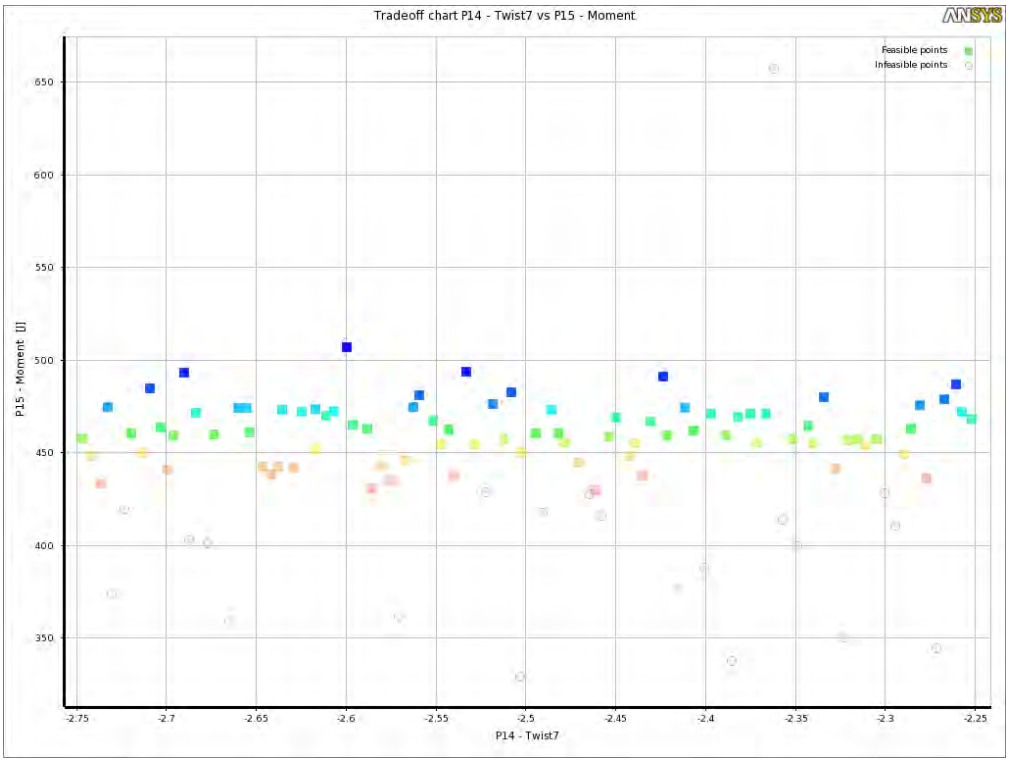

Figure 72: Tradeoff Twist 7

8.4 Optimized Geometry Model

Table 8: Best design candidate vs Original design

Station	Original		Candidate Point 1		Change (%)	
	Chord	Twist	Chord	Twist	Chord	Twist
1	0.737	20.04	0.737	20.205	0	0.8233
2	0.697	11.909	0.76406	12.851	9.621	7.9099
3	0.605	3.425	0.66326	3.3784	9.629	-1.3605
4	0.512	0.494	0.52277	0.4979	2.1035	0.78947
5	0.42	-0.92	0.4374	-1.0032	4.1452	9.04347
6	0.328	-2.191	0.34718	-2.16	5.8475	-1.4148
7	0.305	-2.05	0.32046	-2.5995	5.0688	26.8048

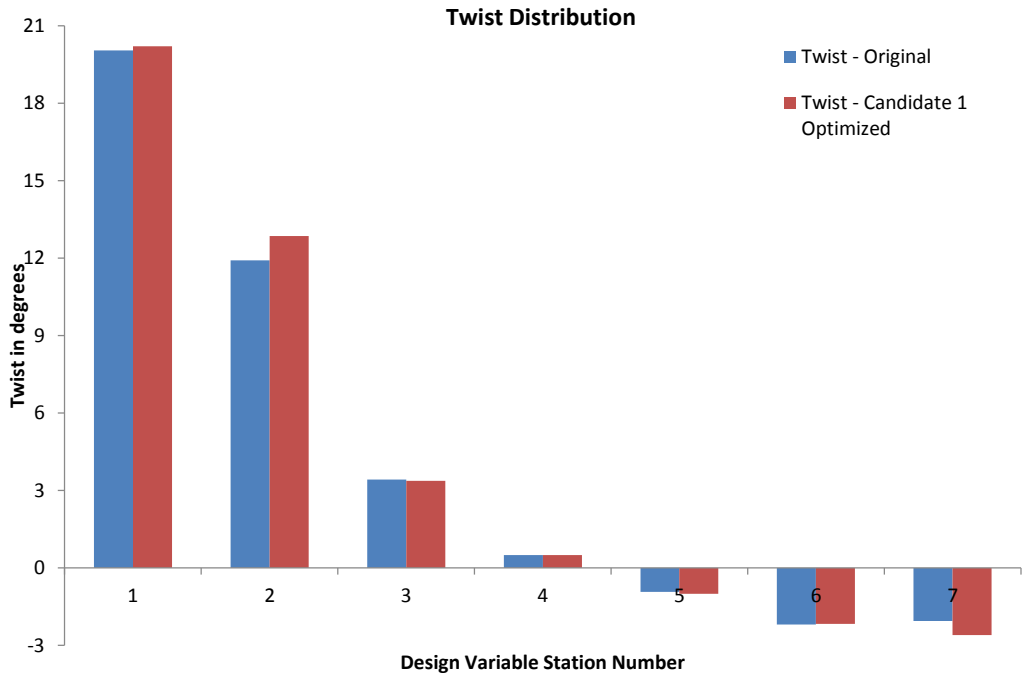

Figure 73: Twist Distribution

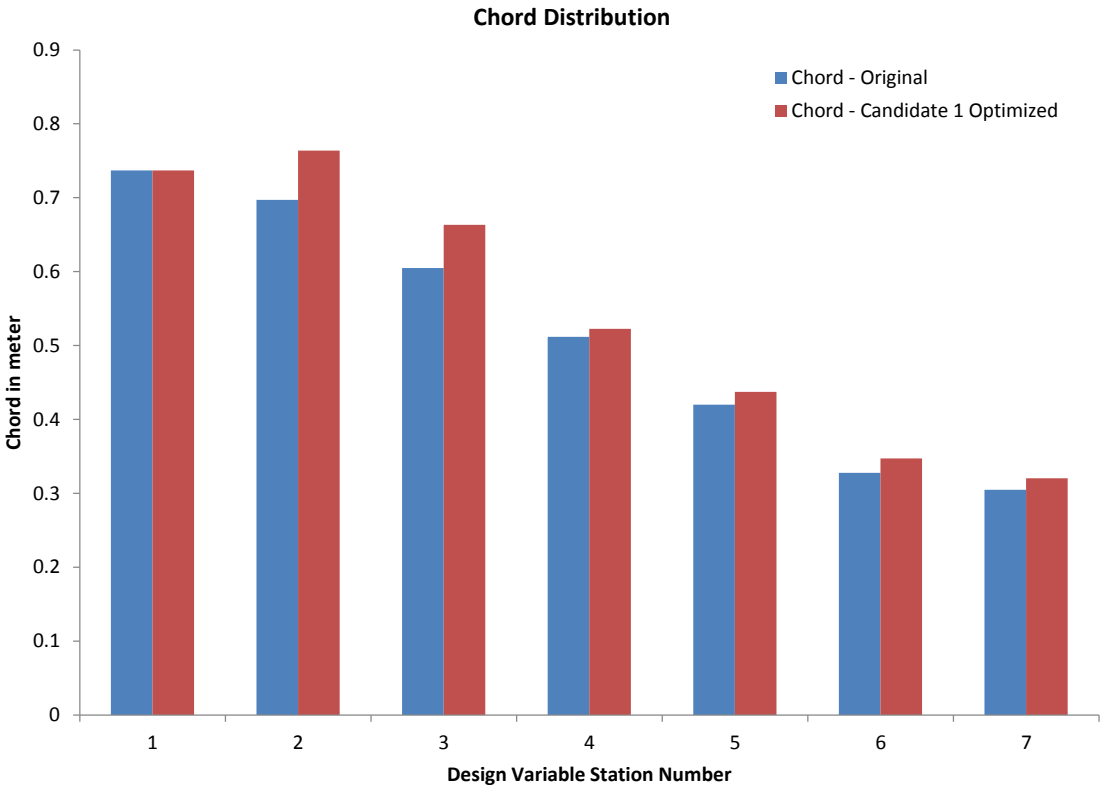

Figure 74: Chord Distribution

The process of aerodynamic optimization, especially where a global optimum search space was provided is often computationally heavy. Nonetheless, a robust use of 1 equation Spallar- Allmaras model with the aid of coarse mesh provided an effective gauge of the optimized model. To further ascertain the claim of optimized model through the use of coarse mesh and aforementioned turbulence model, a refined mesh with higher numerical scheme was used to survey the power output through a wide range of operating wind speeds. The figure below represents the optimized blade geometry using best candidate design point 1.

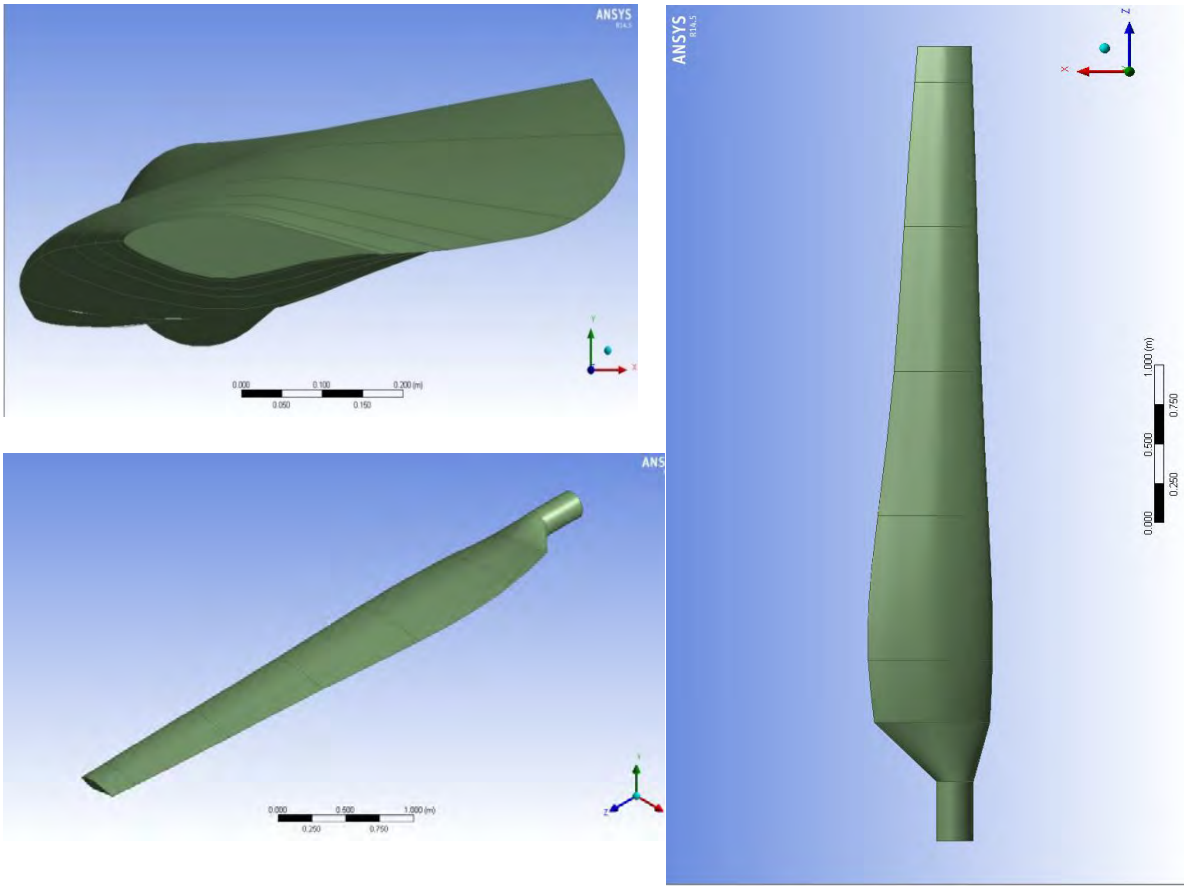

Figure 75: Optimized NREL VI Candidate 1

8.5 Results

8.5.1 Comparison of Power Output

Similar to the validation of the power generated by the baseline design for various wind speed, the optimized blade was also simulated and the power numerically computed. Since the baseline validation failed to effectively compute the power at 13.1 m/s and 15.1 m/s wind speed, the effective increment in the power output using the optimized blade will be ignored for those wind speeds. Table 9 highlights the stats of the power increment at different wind speeds. Figure 76 and 77 shows the power curve and coefficient of power curve plotted against the wind speeds. However, to effectively gauge the power

increment experimental validation is a must while CFD analysis gives only an approximation.

Table 9: Power Computed

Wind Speed	Computed Torque (N-m)		Power (KW)		Increase
m/s	Baseline	Optimized	Baseline	Optimized	(%)
5	257.64	320.46	1.942	2.416	24.38
7	756.864	802.038	5.706	6.047	5.968
10	1361.47	1487.72	10.265	11.217	9.273
13.1	899.96	1067.88	6.785	8.052	18.658
15.1	701.35	1124	5.288	8.474	60.26

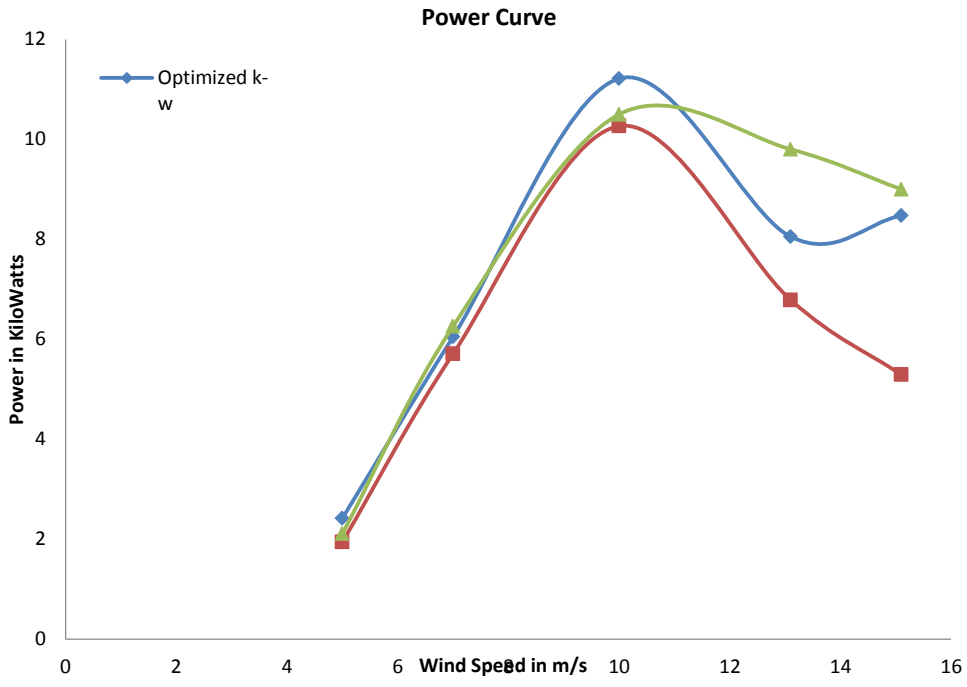

Figure 76: Power Curve Computed

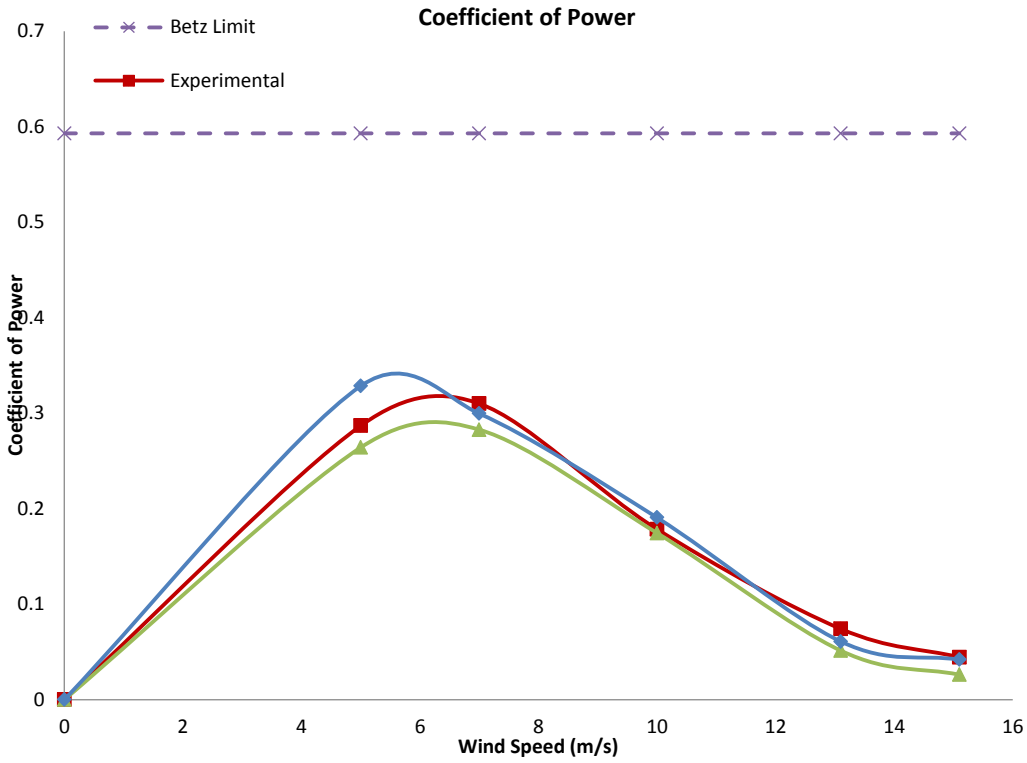

Figure 77: Coefficient of Power vs Wind Speed

8.5.2 Flow Visualization and Pressure Coefficient Distribution

The coefficient of pressure plots, pressure contours and the streamlines supports the power increment in the optimized blade. As stated earlier, due to under estimation of torque at 13.1 m/s and above, the coefficient of pressure plots will not be compared.

Figure 78, shows the pressure coefficient plots at different span location over the dimensionless chord along the x coordinate. The optimized blade model seems to have increased the local flow angle of attack. This is clearly indicated at 30% span location where pressure difference on the suction and pressure side is clearly defined. The same is not observed in the original baseline design. Moreover, in the baseline design the suction side pressure coefficient has a negative slope gradually increasing towards the trailing edge but in the optimized model, the first half of the suction side experience a positive pressure gradient with a steep negative gradient on the second half accompanied by a large pressure at the pressure side. The twist distribution at the root and the tip of the optimized blade contributes effectively for the increased power.

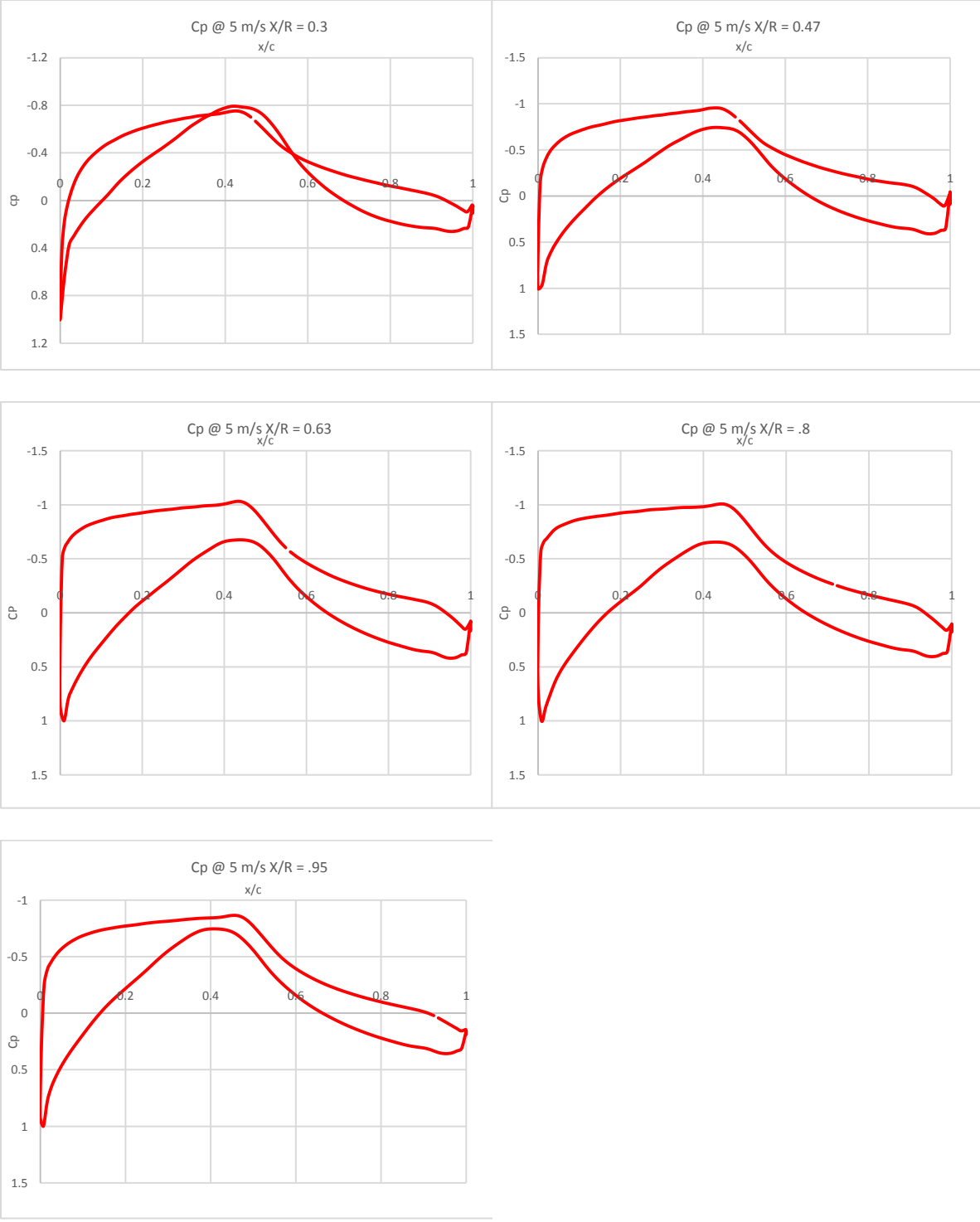

Figure 78: Coefficient of Pressure Distribution at 5 m/s

The plots and streamlines displayed in Figure 79, show fully attached flow throughout the blade span.

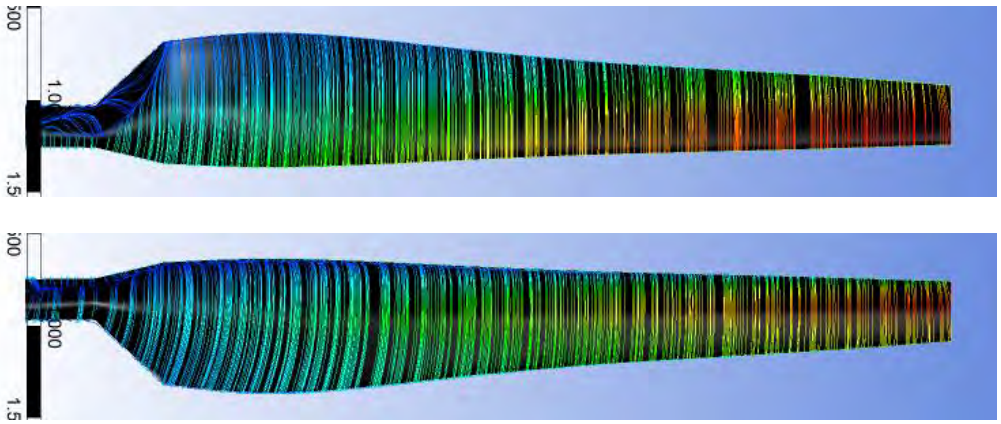

Figure 79: Velocity Streamlines 5m/s, Top - Pressure, Bottom-Suction

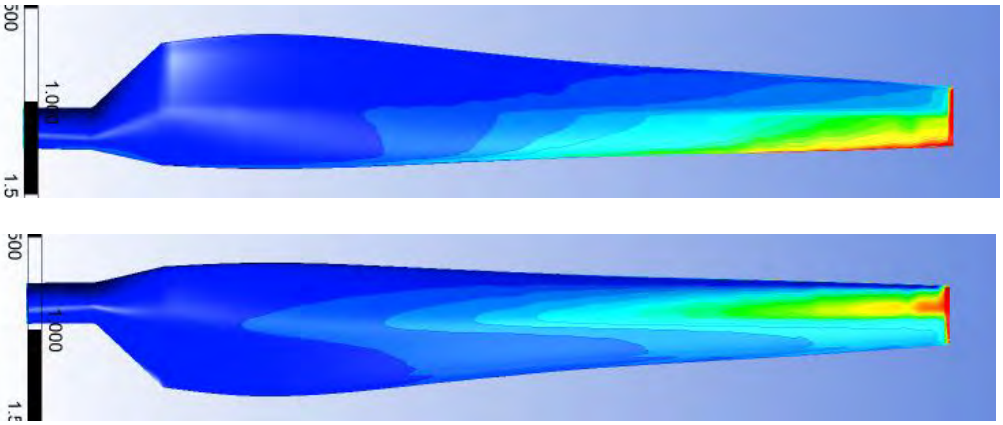

Figure 80: Turbulent Intensity5 m/s, Top - Pressure, Bottom - Suction

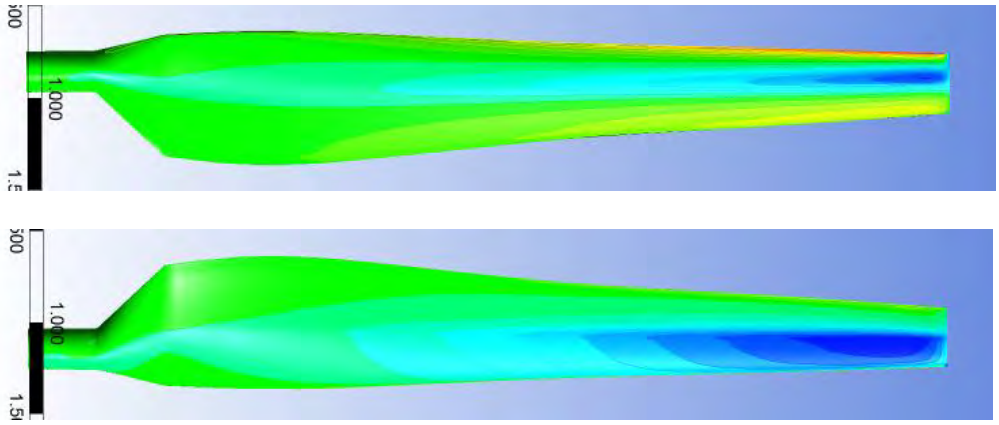

Figure 81: Pressure Contour 5 m/s, Top - Pressure, Bottom - Suction

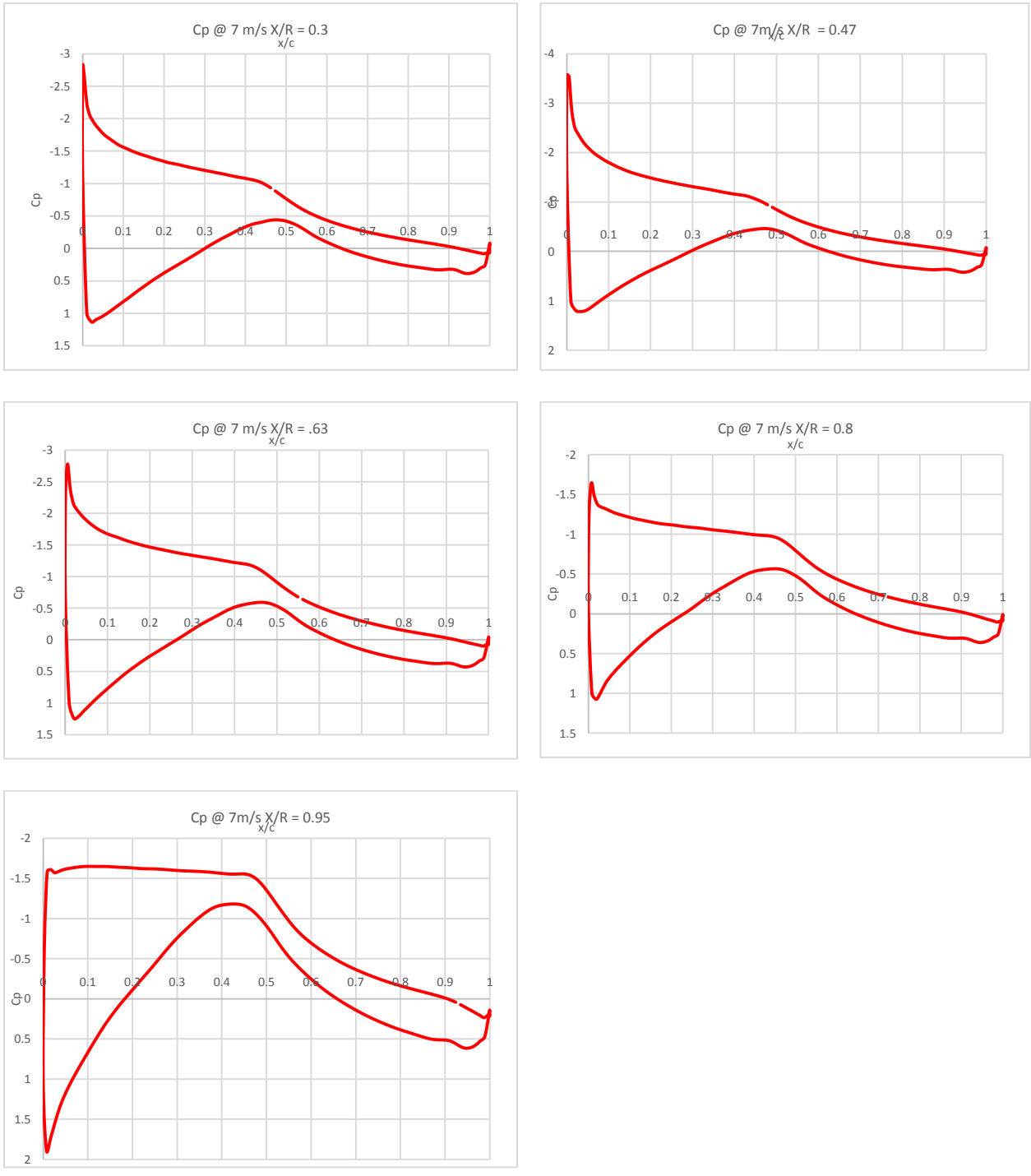

Figure 82: Coefficient of Pressure Distribution at 7 m/s

At 7 m/s the coefficient of pressure plots resemble much like the baseline plots and the power increase is also approximated to 6%. Not much of a difference is observed other than a steeper pressure gradient on the suction side of the blade. At 95%, the tip contributes more to the aerodynamic forces than the baseline design. Velocity streamlines and pressure contours with coefficient of pressure plots show fully attached flow regime.

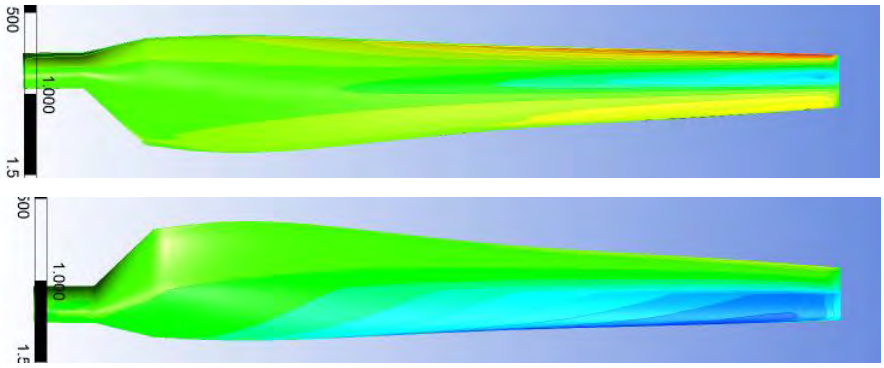

Figure 83: Pressure Contour 7 m/s, Top - Pressure, Bottom- Suction

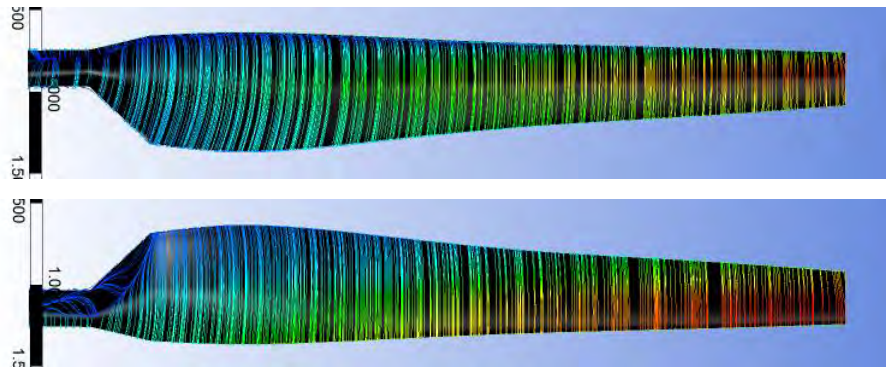

Figure 84:Velocity Streamlines 7 m/s, Top -Pressure, Bottom -Suction

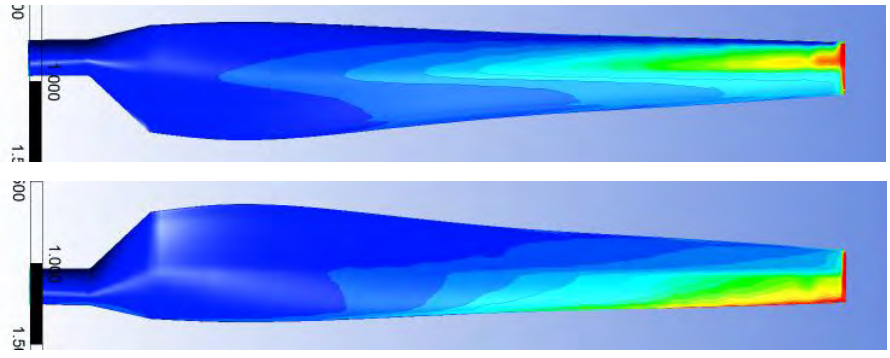

Figure 85: Turbulent Intensity 7 m/s, Top - Pressure, Bottom - Suction

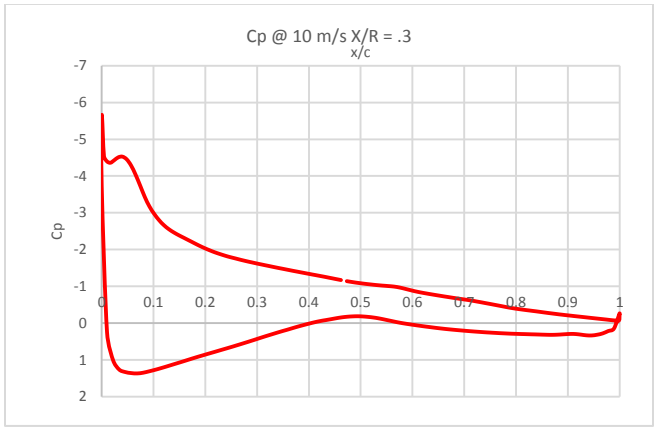

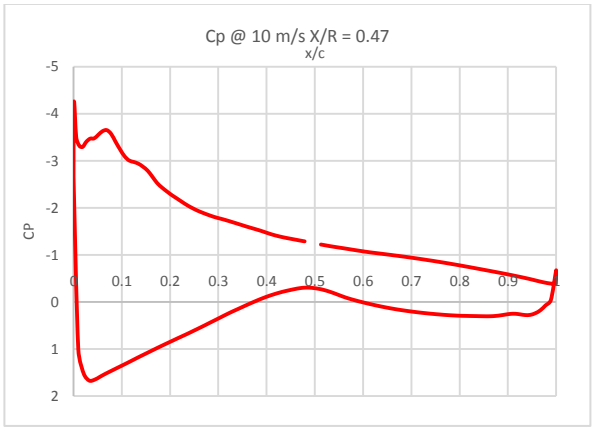

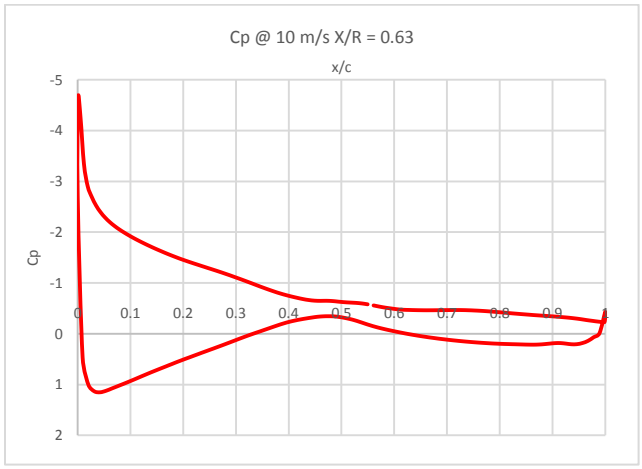

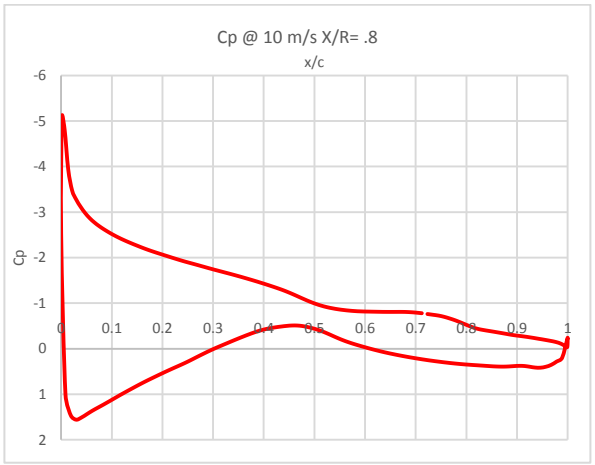

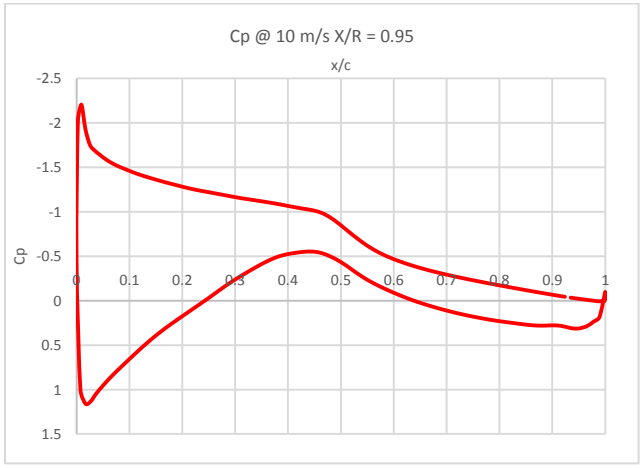

Figure 86: Coefficient of Pressure Distribution at 10 m/s

The most interesting observation seems to be at 10 m/s wind speed. Although flow separation occurs and the blade experiences the onset of stall, with cross vortex flow, the length of the blade span that experience the flow separation in now less than the baseline to just 80% of the span. At 60% the separation seems to be around the mid chord rather than quarter chord as in baseline. Above 80% span the flow is fully attached.

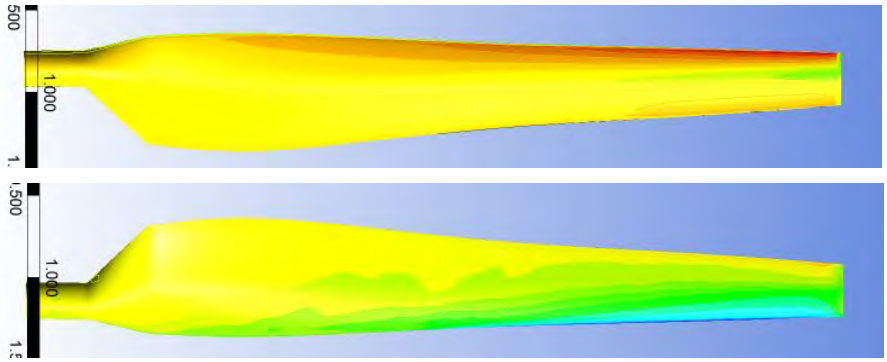

Figure 87: Pressure Contours 10 m/s, Top - Pressure, Bottom - Suction

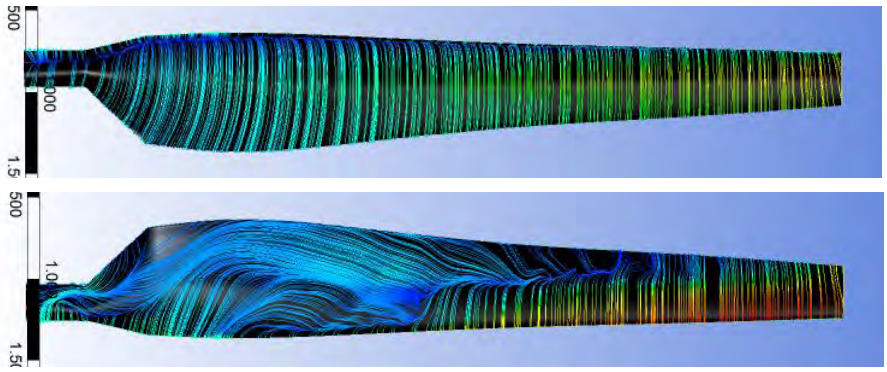

Figure 88: Velocity Streamlines 10 m/s, Top - Pressure, Bottom –Suction

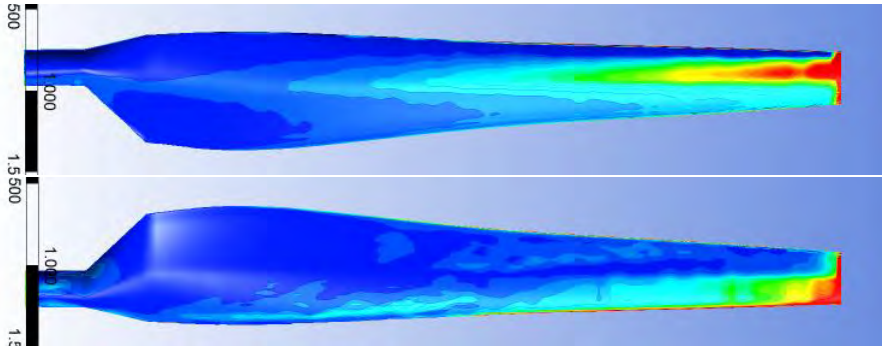

Figure 89: Turbulent Intensity 10 m/s, Top - Pressure, Bottom – Suction

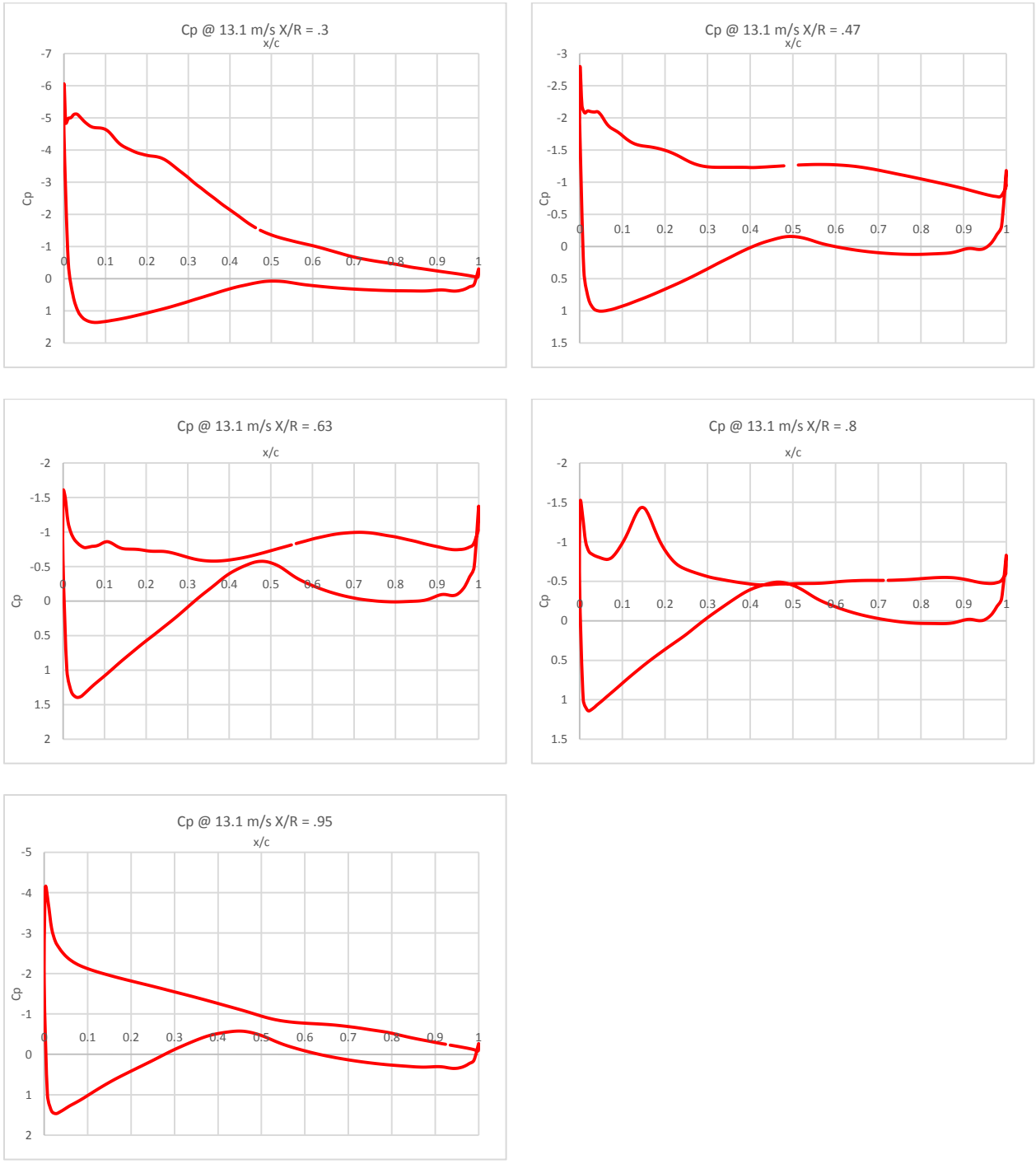

Figure 90: Coefficient of Pressure Distribution at 13.1 m/s

The pressure coefficient for 13.1 m/s show a highly turbulent flow up to the tip of the blade. From 47% to 80% of the blade length, the turbulent flow at the trailing edge seems

to be influence by flow leaving the pressure side of the blade, causing localized flow circulation or vortices. The blade is highly effected by oblique turbulent cross flows from rotation and the leading edge itself marks the region of flow separation.

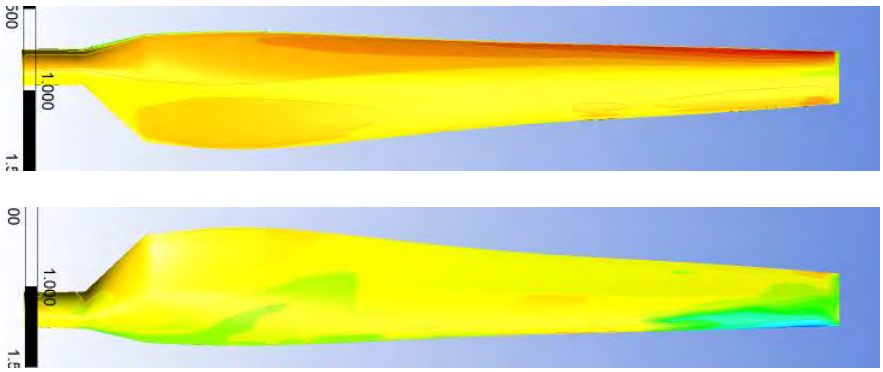

Figure 91: Pressure Contours 13.1 m/s, Top - Pressure, Bottom - Suction

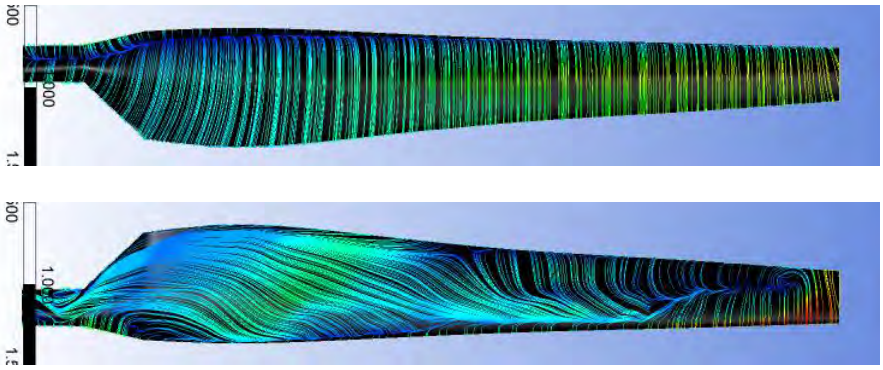

Figure 92: Velocity Streamlines 13.1 m/s, Top - Pressure, Bottom - Suction

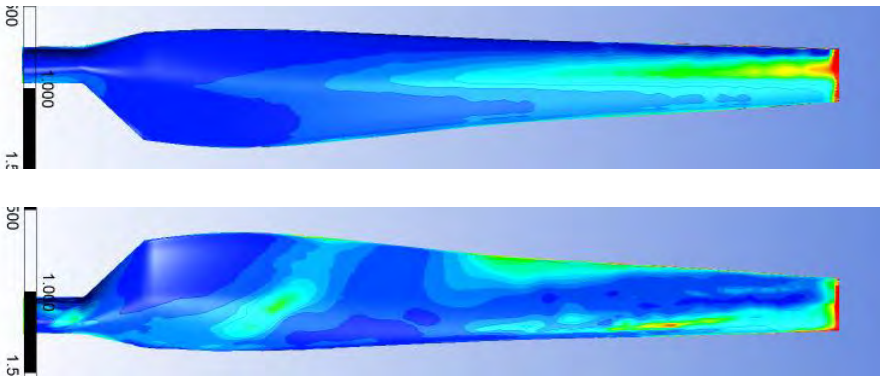

Figure 93: Turbulent Intensity 13.1 m/s, Top - Pressure, Bottom - Suction

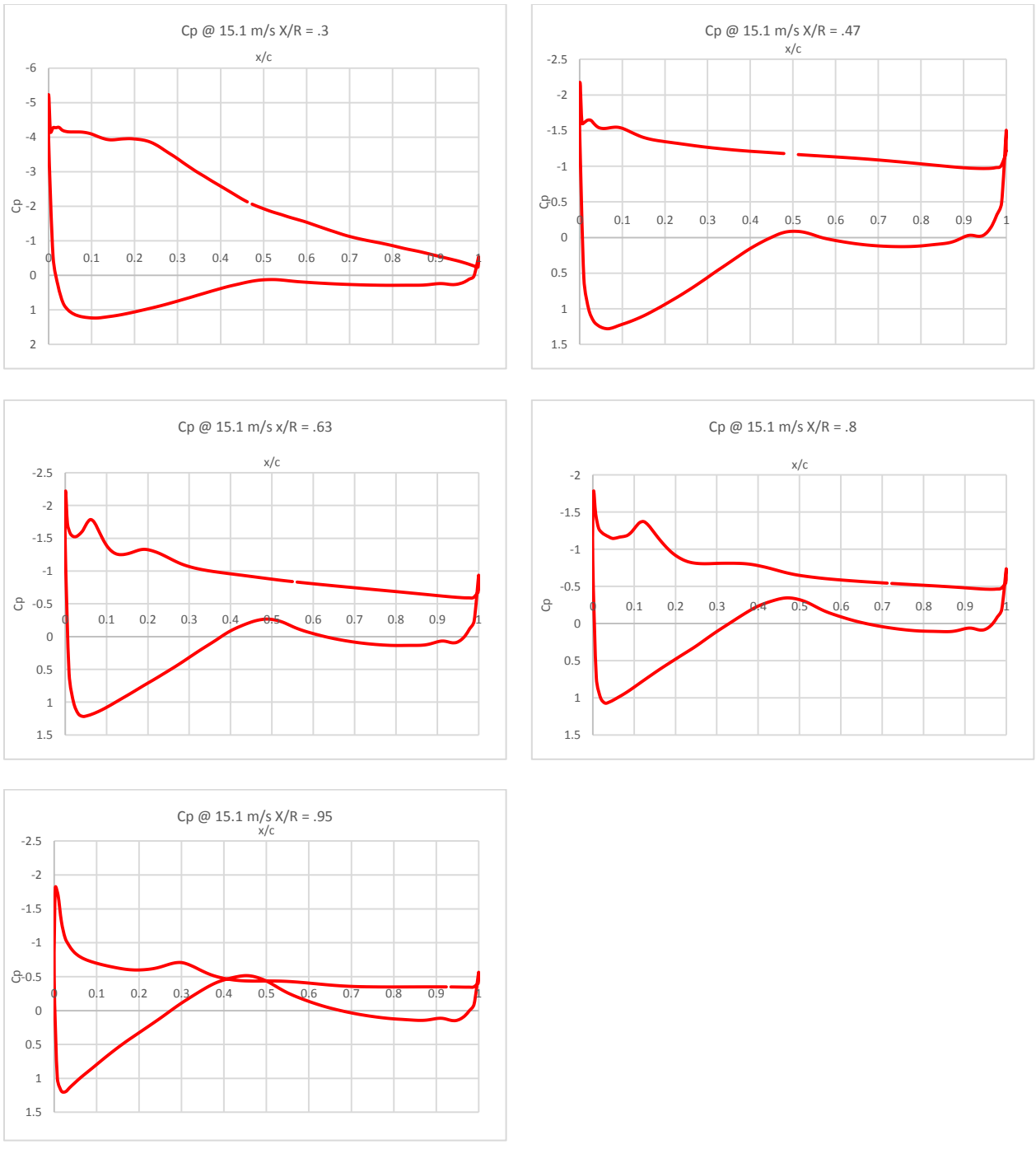

Figure 94: Coefficient of Pressure Distribution at 15.1 m/s

Fully turbulent flow is observed throughout the blade suction side. Even the tip experience flow separation unlike the previous case where the flow was attached at the

tip. The flow is highly unsteady and computations results are likely not very accurate at this speed. The use of higher numerical scheme may resolve the flow situation better.

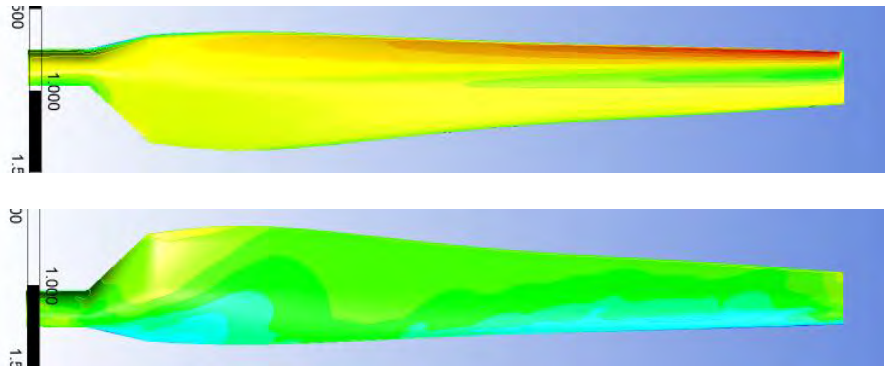

Figure 95: Pressure Contours 15.1 m/s, Top - Pressure, Bottom - Suction

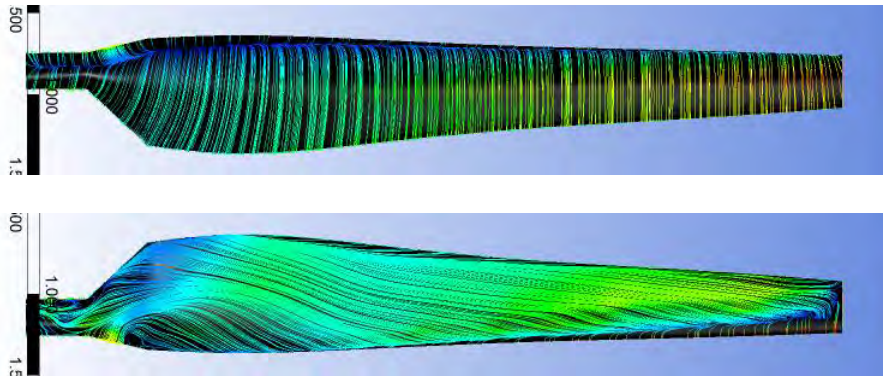

Figure 96: Velocity Streamlines 15.1 m/s, Top - Pressure, Bottom - Suction

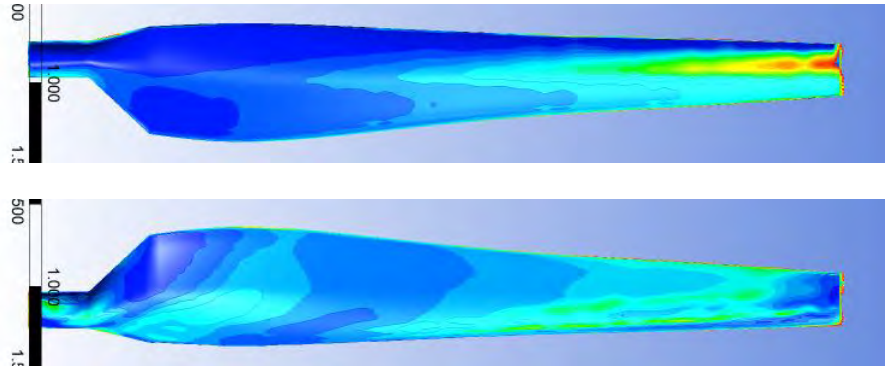

Figure 97: Turbulent Intensity 15.1 m/s, Top - Pressure, Bottom – Suction

9. Conclusion

In the process of aerodynamic optimization for increased power, a series of wind speed from Unsteady Aerodynamic Experiment Sequence S had been used to compute the power increment in the newly optimized blade. The validation of the original baseline with the same test sequence resulted in accurate solution till 10 m/s wind speed by employing k-ω SST turbulence model. Further increase in the flow speed under predicted the torque produced and lead to erroneous results.

Parameter correlation study and sensitivity analysis conducted gave an insight to how the changes in the geometry effect the objective outcome. Unlike a linear objective function and problem set up, aerodynamic optimization inclined toward the non-linear quadratic set up, clearly indicated by the scatter plots and the quadratic determination matrix. The matrix also supported the claim that 99% of the objective outcome was influenced by the geometry. Not every parameter with a positive increment had a positive impact on the objective function which was proved by the sensitivity analysis. Negative sensitivity was reported at station 5 chord and station 7 twist, where increasing these parameters resulted in decreasing torque.

The process of optimization included an Adaptive Single Objective Optimization algorithm, where by an automatic intelligent refinement of point is employed based on gradient method. After the sample space of design points were created and screening of these points concluded, the algorithm started the evaluation of these points using the intelligent refinement of points to provide a global optimum. However, due to computational burden only a shortened domain reduction and evaluations could be

employed where by the algorithm failed to achieve a global optimum within the provided bounds but a local optimum was still found. During the process of optimization a robust 1 equation Spallart – Allmaras model was employed for quicker convergence of the flow and the mesh was coarsened to reduce the computation cost. This resulted in five best candidate design. Only the best candidate point was chosen for further evaluation.

Simulations were conducted on optimized blade using k-ω SST turbulence model under similar operating conditions as the baseline and resulted in an increased objective function, power output. At 5 m/s, a reported increase of 24.38%, 5.9% for 7 m/s and 9.2% for 10 m/s were computed. The increment for higher wind speed was ignored on the grounds of failed accuracy when baseline validation was conducted.

Flow visualization and plots of coefficient of pressure through the wind speed for optimized blade showed significant contribution to the increased power output. Blade span location at 30% and 95% displayed large pressure gradient between the suction and pressure side of the optimized blade. Flow speed under 7m/s had characteristics of attached flow and localized flow separation with rotational cross flow were observed at higher velocities with 15.1 m/s having fully separated flows over the entire suction side of the blade.

At 5 m/s wind speed the optimized blade had a relatively larger angle of attack to the incoming relative wind, producing a large pressure gradient across the suction and the pressure side of the blade, this relative incident had a significant impact on the power output. A particular characteristic observation was at 10 m/s for both blades. Baseline computations showed oblique vortices and flow separation running from leading edge at 30% towards the trailing at approximately 85% blade span while optimized blade had

flow separation along the mid chord at 47% running up to 80% blade span. This could be the reason for the increased objective outcome at that wind speed due to larger section of tip being exposed to attached flow as opposed to the baseline design.

The use of k-ω SST turbulence model to capture the transition of flows is unquestionable but to better predict the computational results for fully separated flows, a use of higher numerical scheme may be more advisable. Also changing the solver scheme of the pressure may result in a better convergence at higher wind speed.

Although, the airfoil shape was constrained to the S809 for the current study, a use of ad-joint solver could further modify the shape to a more aerodynamic optimum to achieve better results. This would lead to a newer blade cross sectional shape but the application of the optimized profile for wind turbine may be compromised. However, if suitable constraints on the thickness of the profile around 21% chord length is provided, it could still maintain its application.

Appendix A

NREL VI at 5 m/s wind speed

r/R	Pressure Contour
0.3	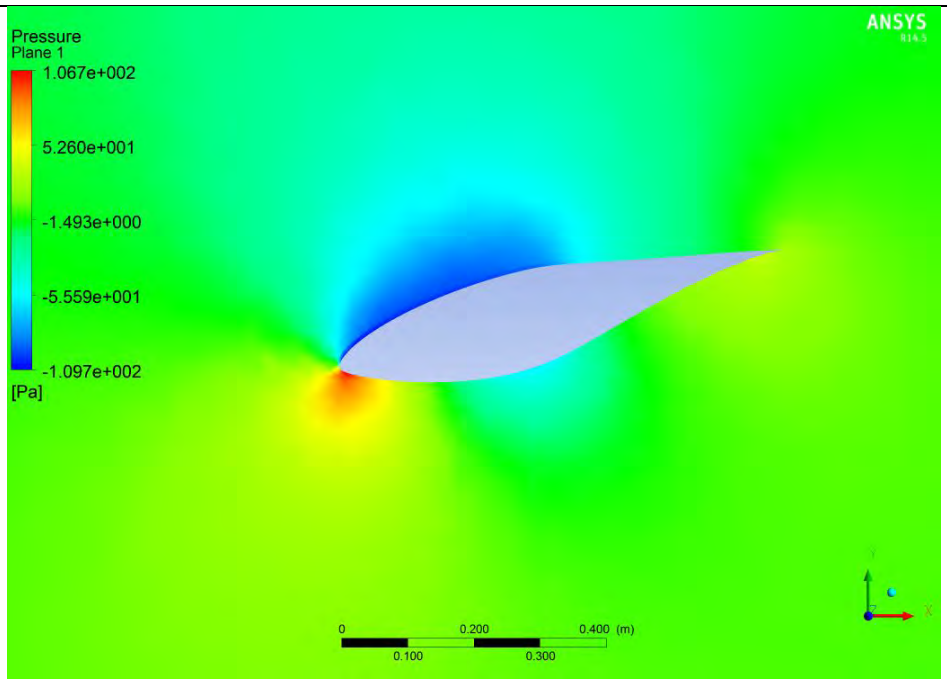
0.45	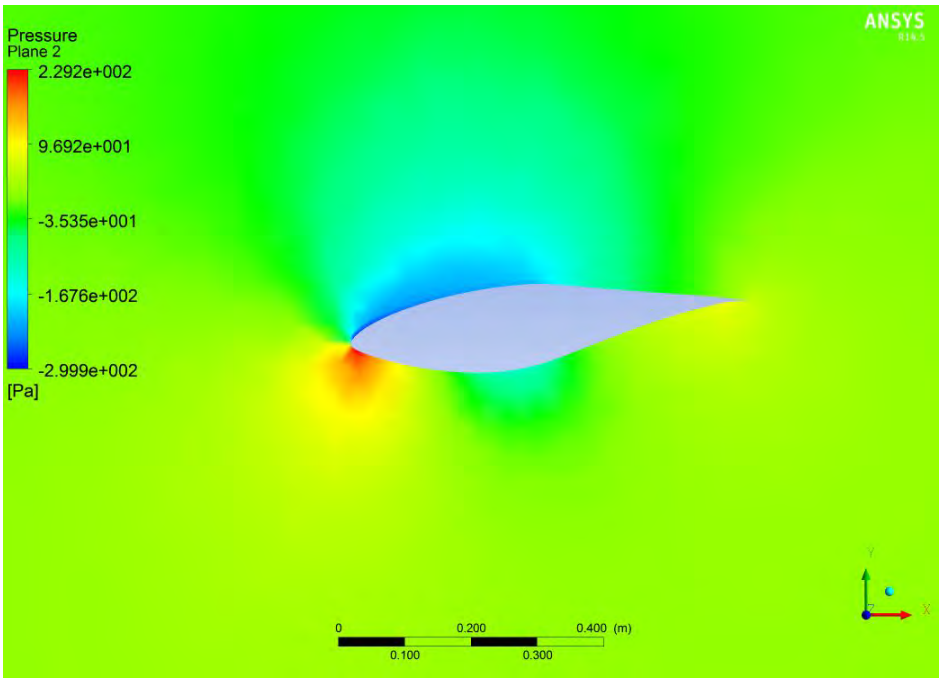

0.63

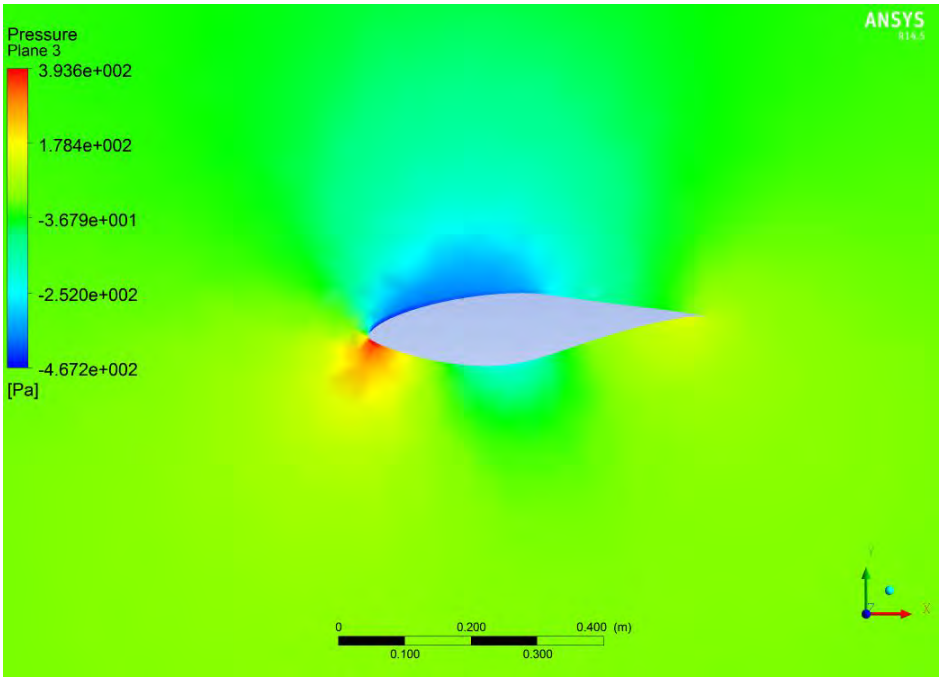
Pressure
Plane 3
3.936e+002
1.784e+002
-3.679e+001
-2.520e+002
-4.672e+002
[Pa]
ANSYS
R14.5
0
0.200
0.400 (m)
0.100
0.300

0.8

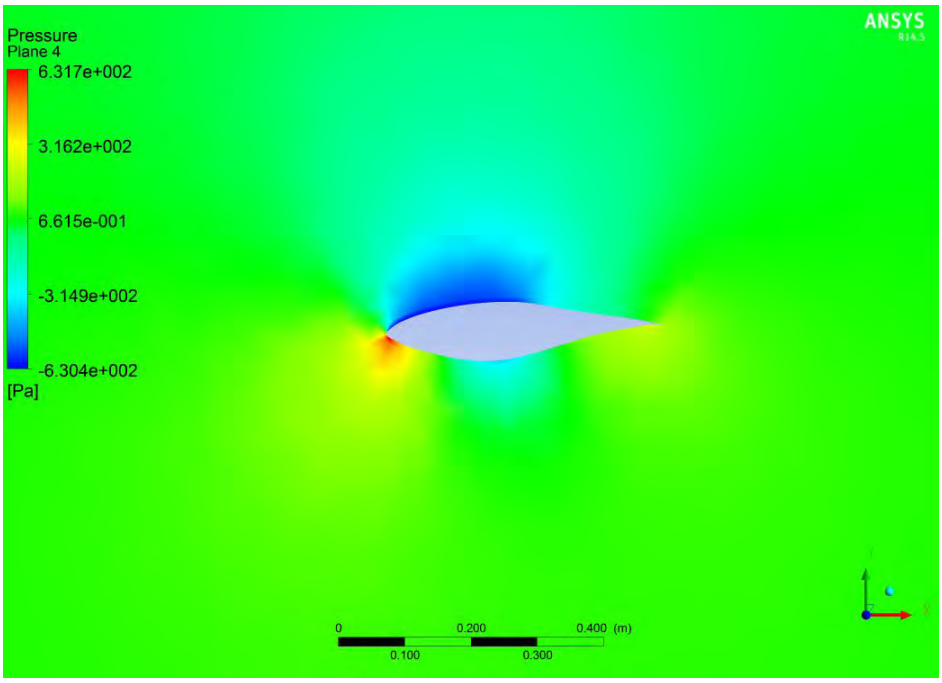
Pressure
Plane 4
6.317e+002
3.162e+002
6.615e-001
-3.149e+002
-6.304e+002
[Pa]
ANSYS
R14.5
0
0.200
0.400 (m)
0.100
0.300

0.95	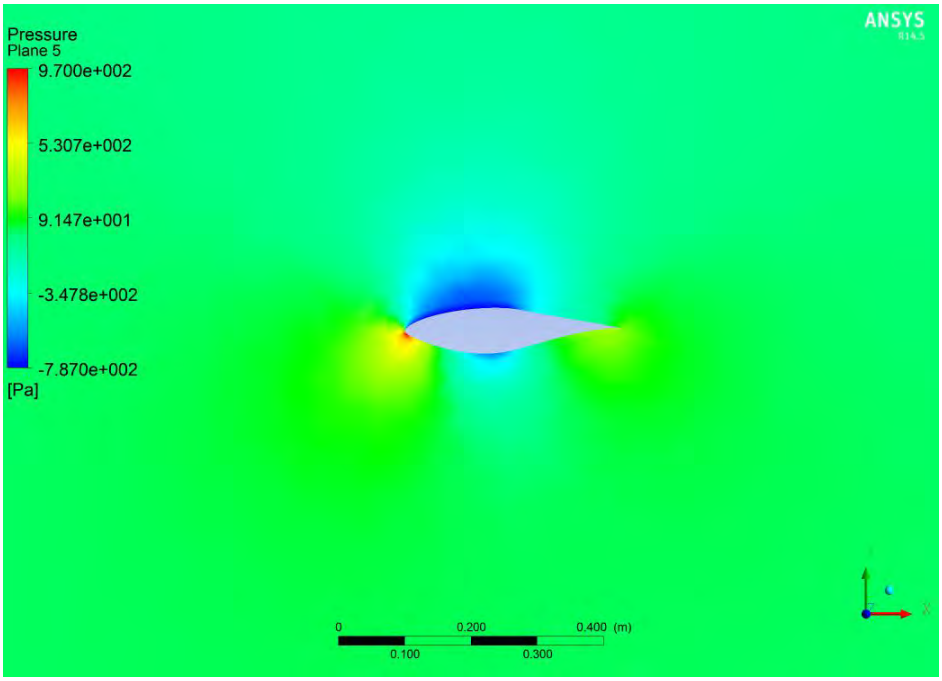

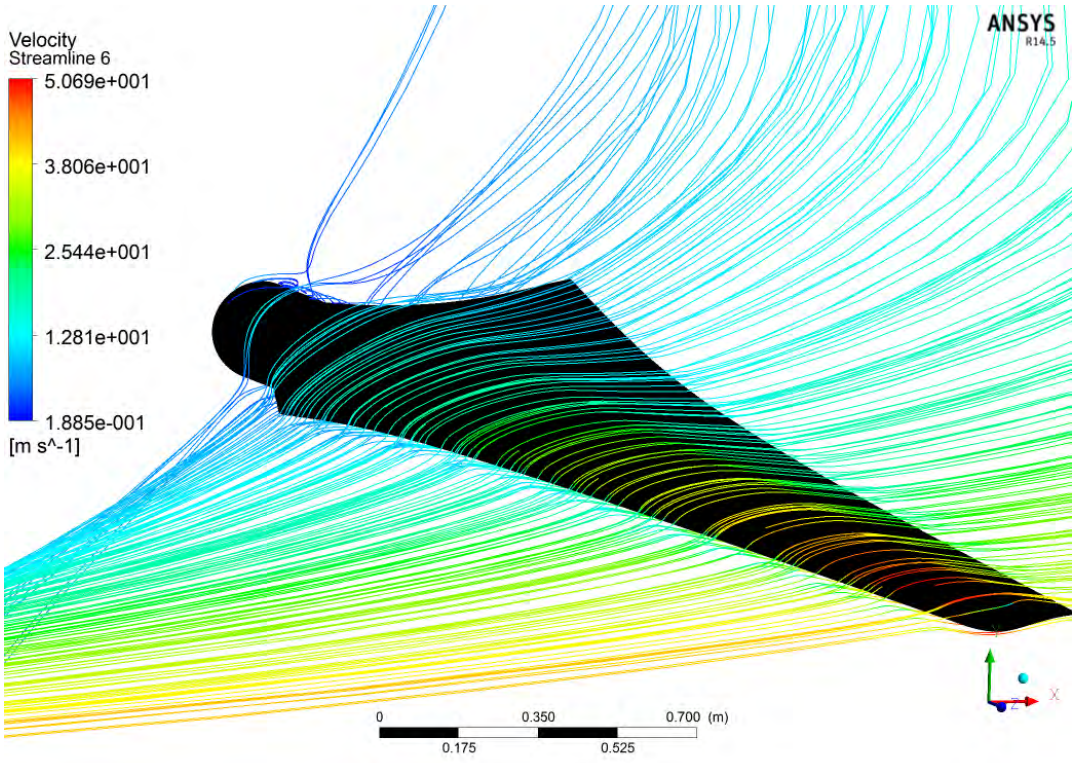

Figure 98: 3D Velocity Streamlines at 5m/s

NREL VI at 10 m/s wind speed

r/R	Pressure Contour
0.3	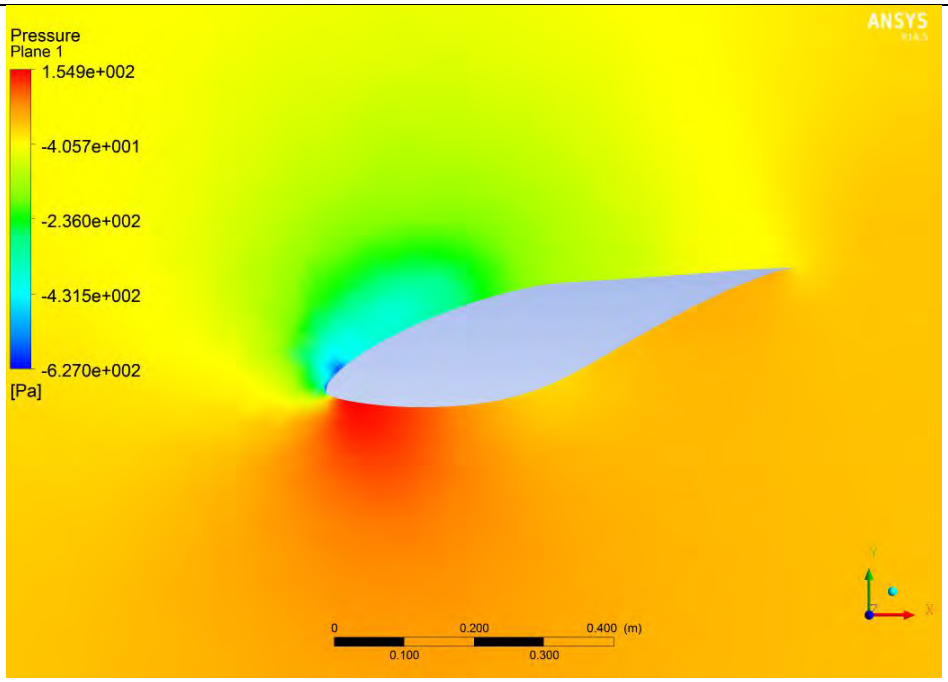
0.45	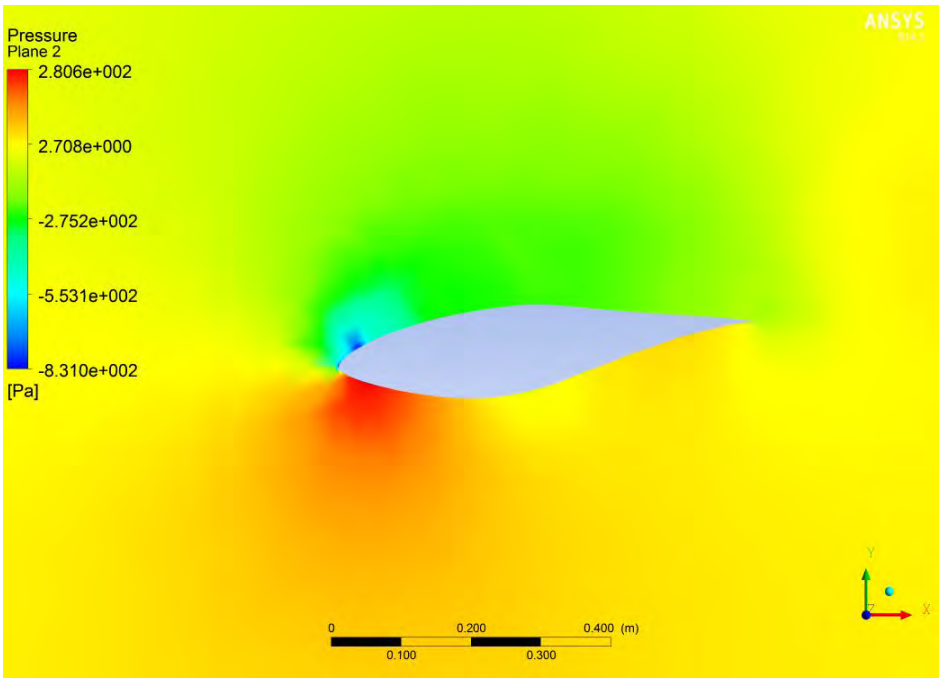

0.63

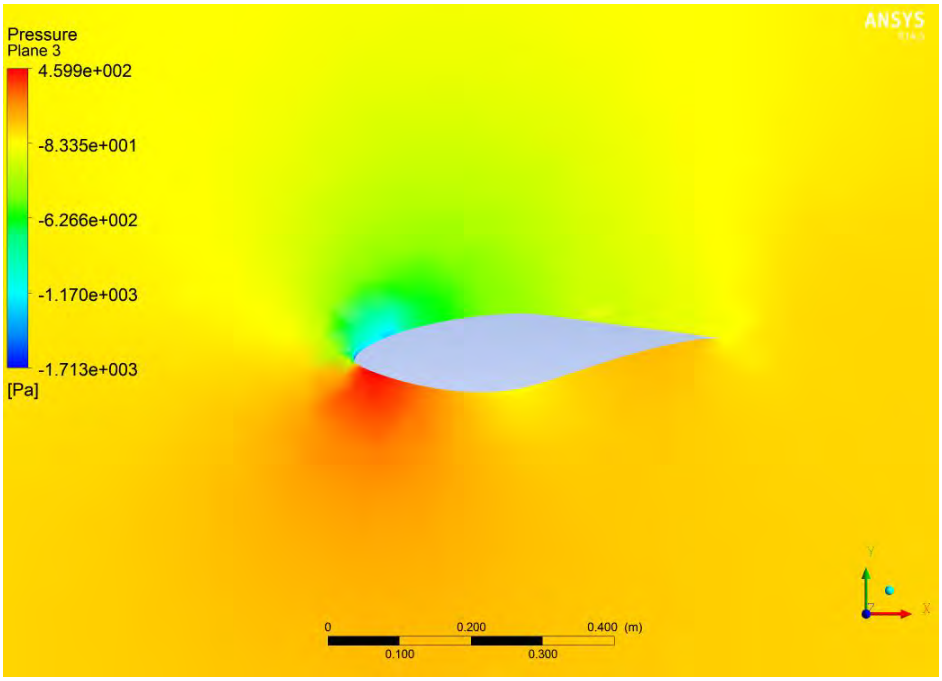
Pressure
Plane 3
4.599e+002
-8.335e+001
-6.266e+002
-1.170e+003
-1.713e+003
[Pa]
ANSYS
0
0.200
0.400 (m)
0.100
0.300

0.8

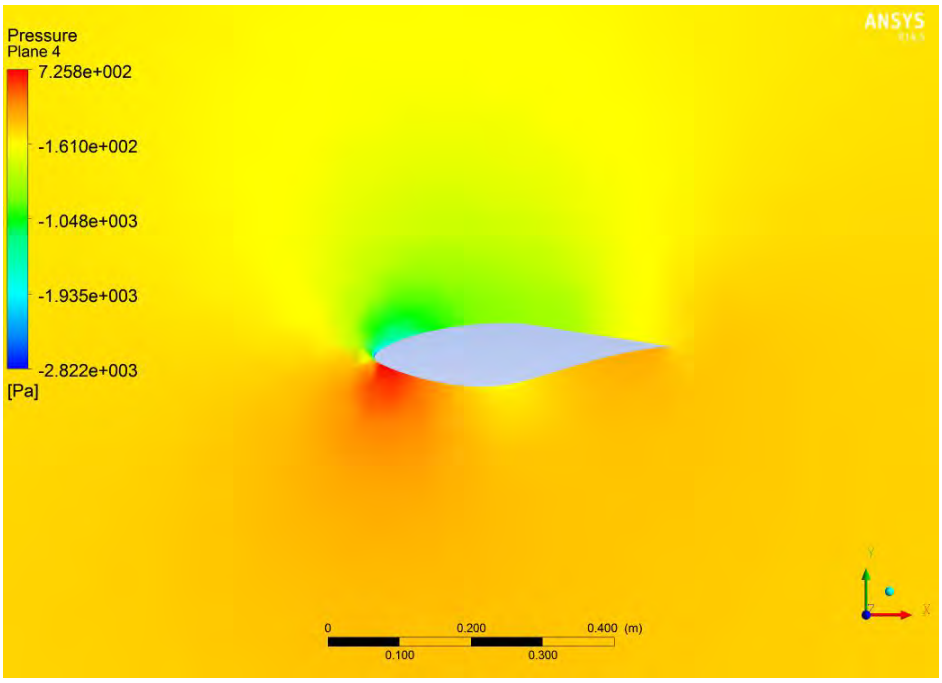
Pressure
Plane 4
7.258e+002
-1.610e+002
-1.048e+003
-1.935e+003
-2.822e+003
[Pa]
ANSYS
0
0.200
0.400 (m)
0.100
0.300

0.95

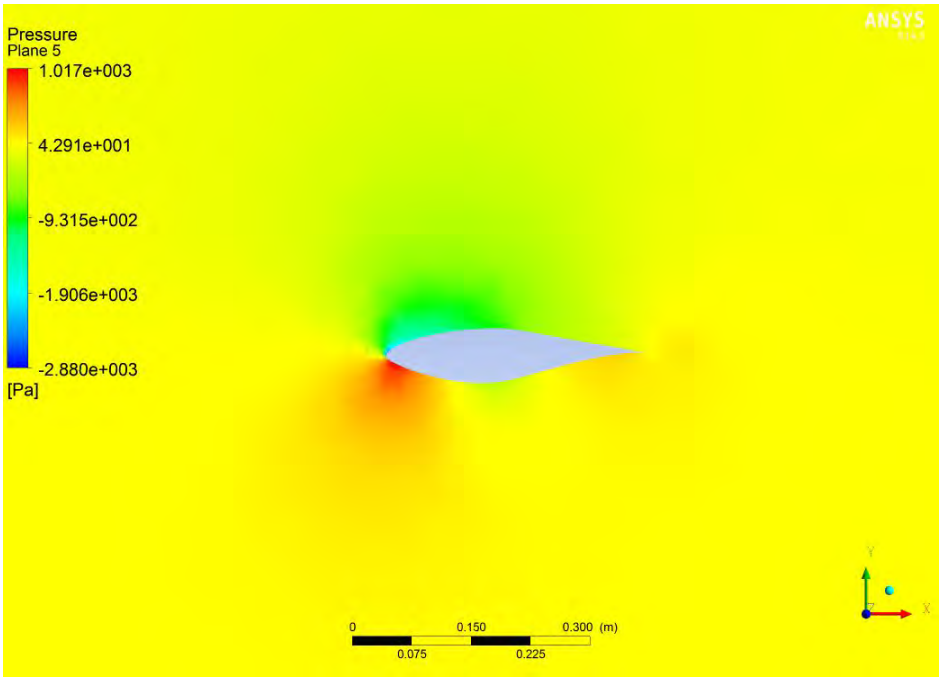

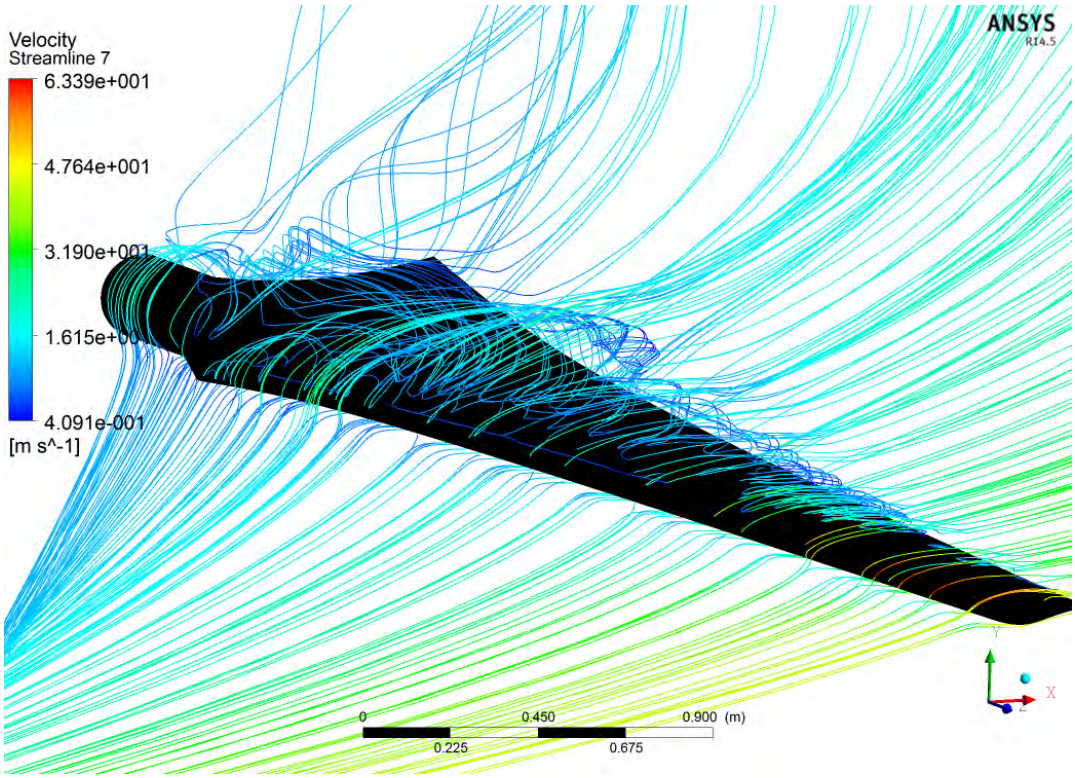

Figure 99: 3D Velocity Streamlines at 10 m/s

NREL VI at 13.1 m/s wind speed

r/R	Pressure Contour
0.3	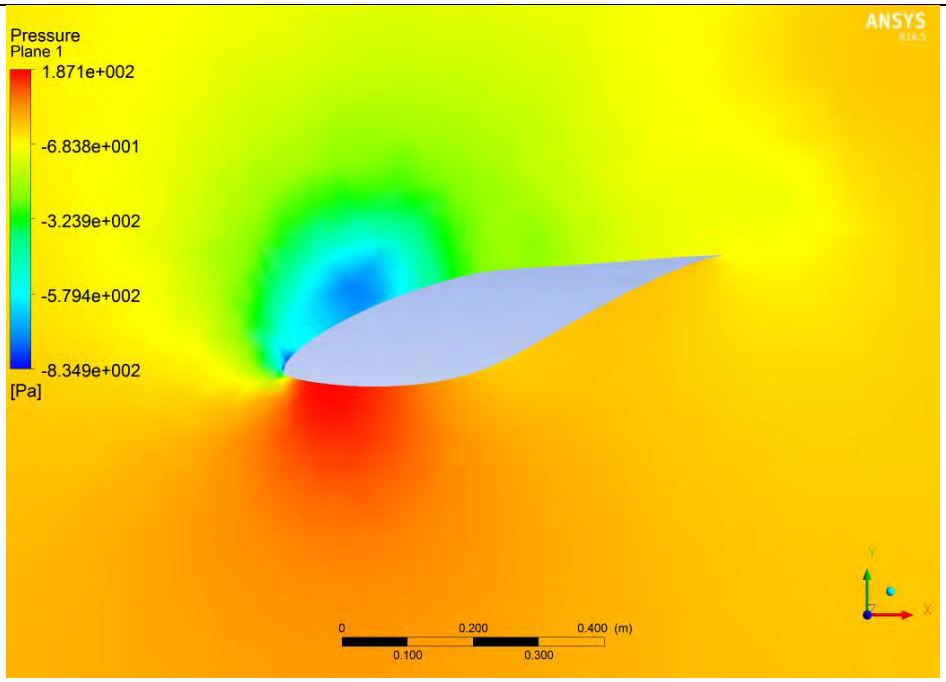
0.45	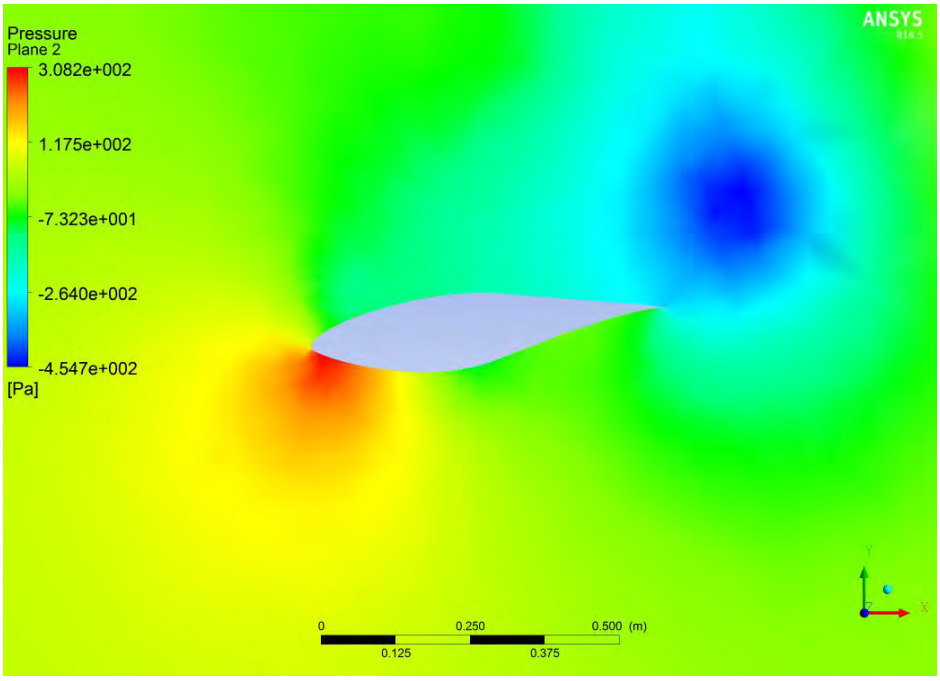

0.63

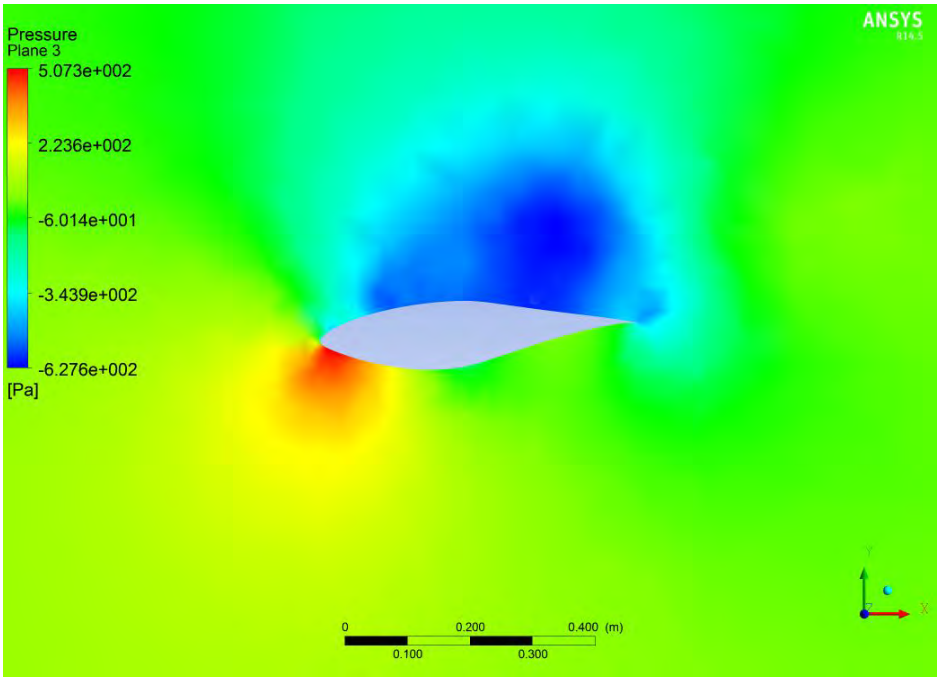
Pressure
Plane 3
5.073e+002
2.236e+002
-6.014e+001
-3.439e+002
-6.276e+002
[Pa]
ANSYS
0
0.200
0.400 (m)
0.100
0.300

0.8

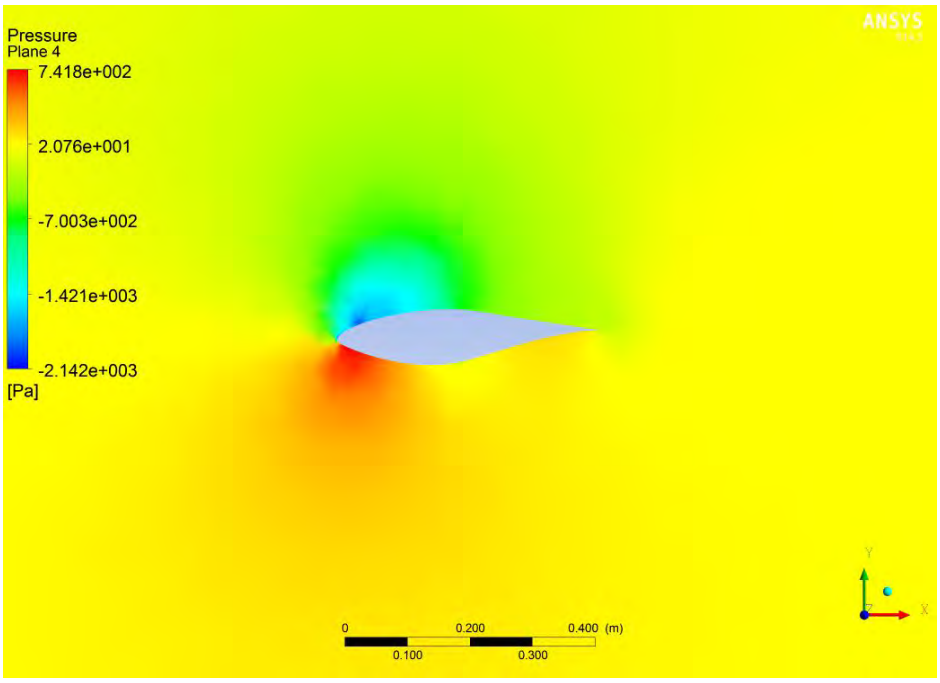
Pressure
Plane 4
7.418e+002
2.076e+001
-7.003e+002
-1.421e+003
-2.142e+003
[Pa]
ANSYS
0
0.200
0.400 (m)
0.100
0.300

0.95	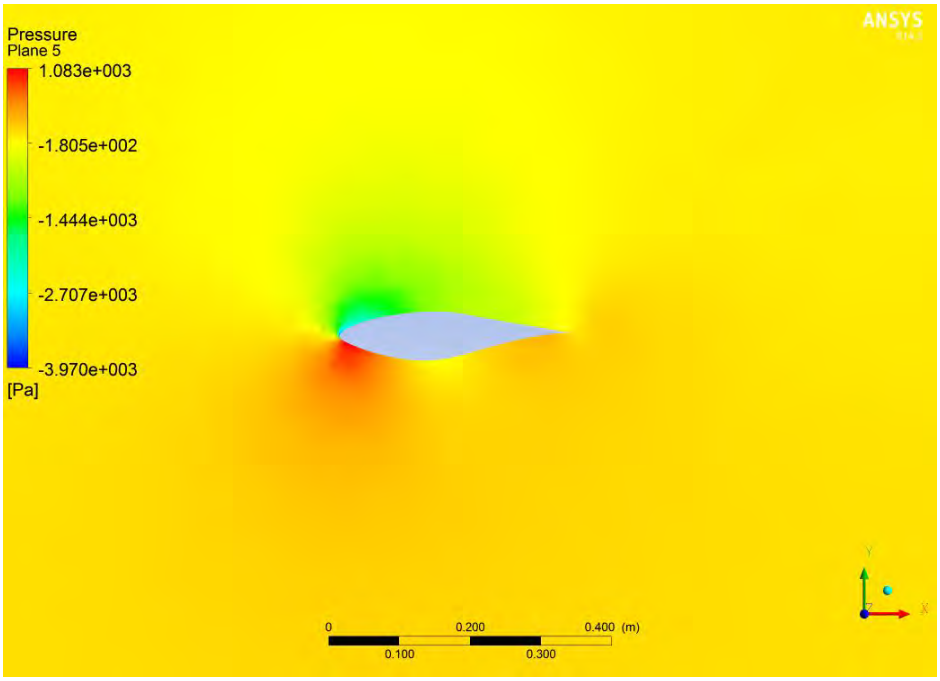

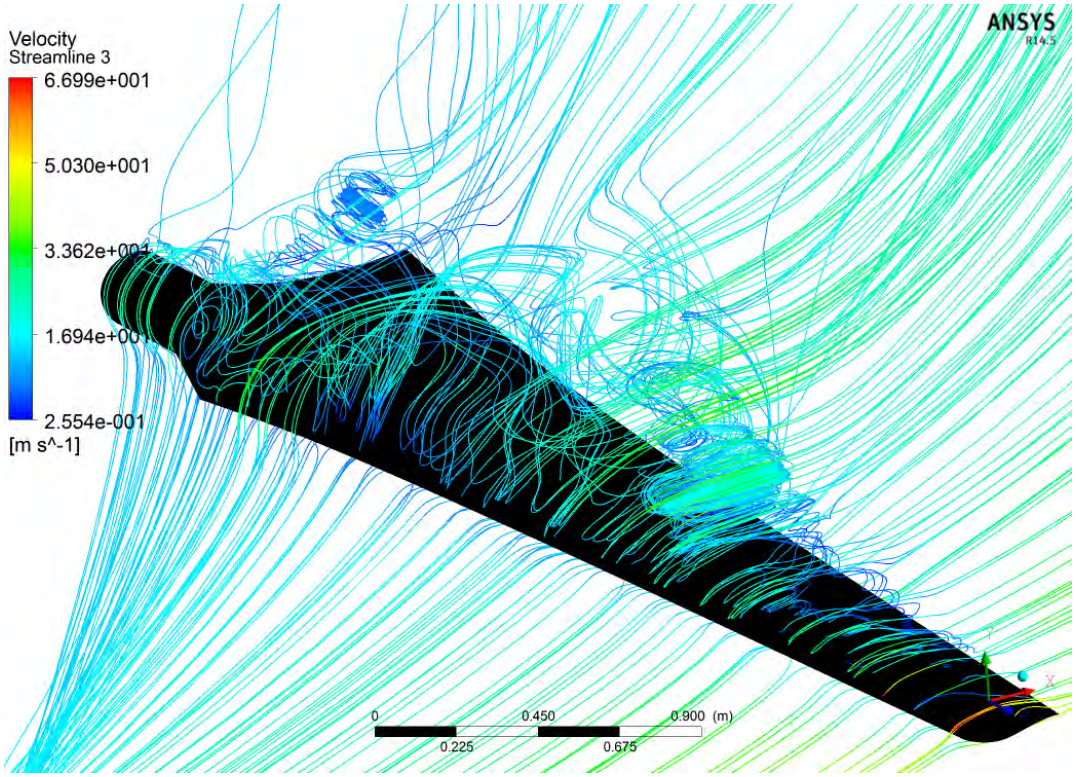

Figure 100: 3D Streamlines at 13.1m/s

Appendix B

Candidate 1 at 5 m/s wind speed

r/R	Pressure Contour
.30	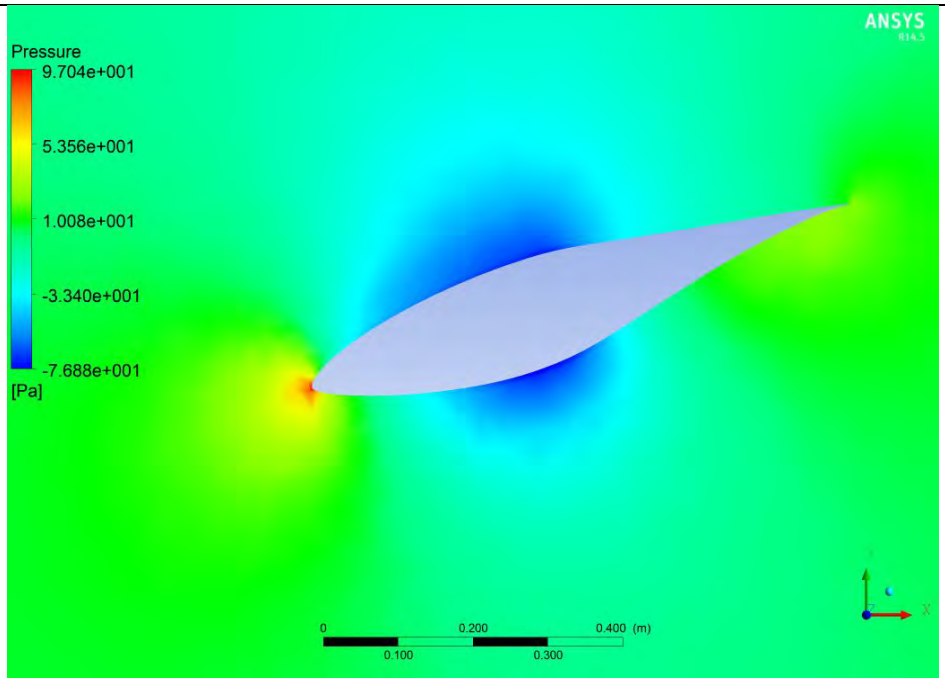
.45	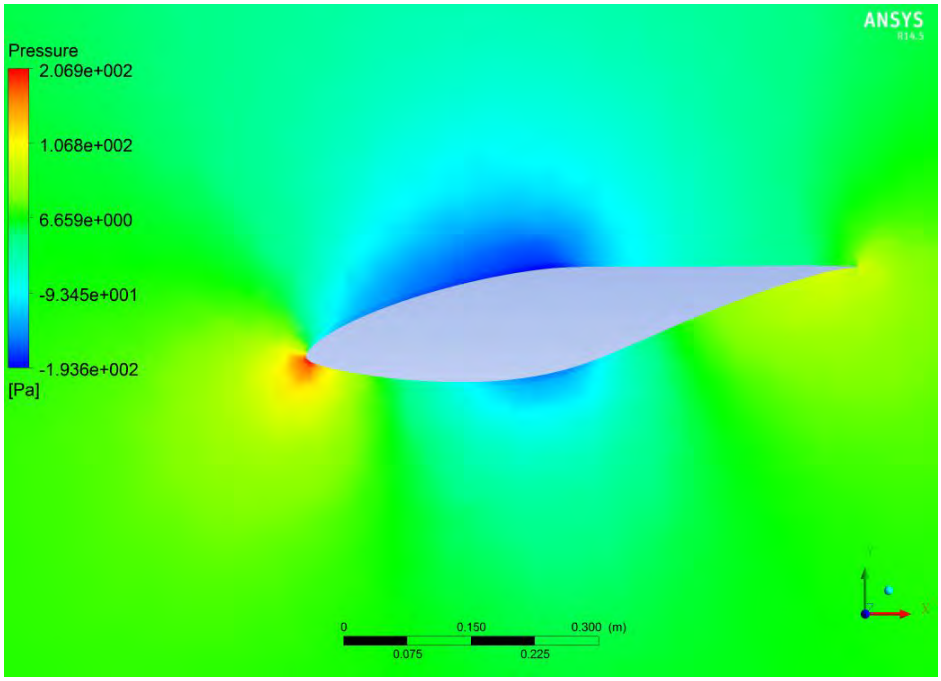

.63	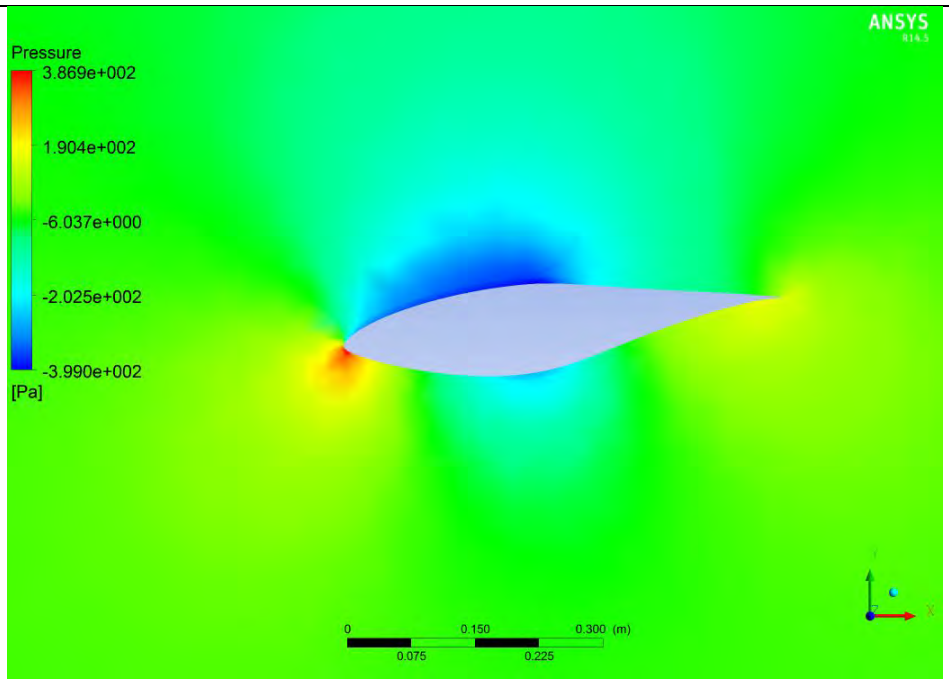 ANSYS Pressure 3.869e+002 1.904e+002 -6.037e+000 -2.025e+002 -3.990e+002 [Pa] 0 0.150 0.300 (m) 0.075 0.225
.80	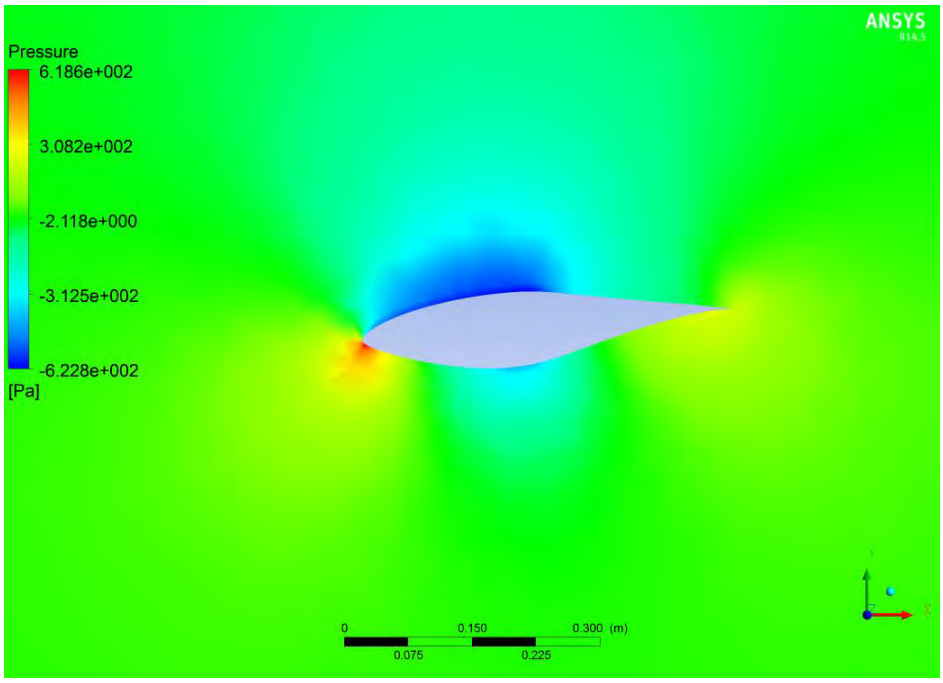 ANSYS Pressure 6.186e+002 3.082e+002 -2.118e+000 -3.125e+002 -6.228e+002 [Pa] 0 0.150 0.300 (m) 0.075 0.225

.95

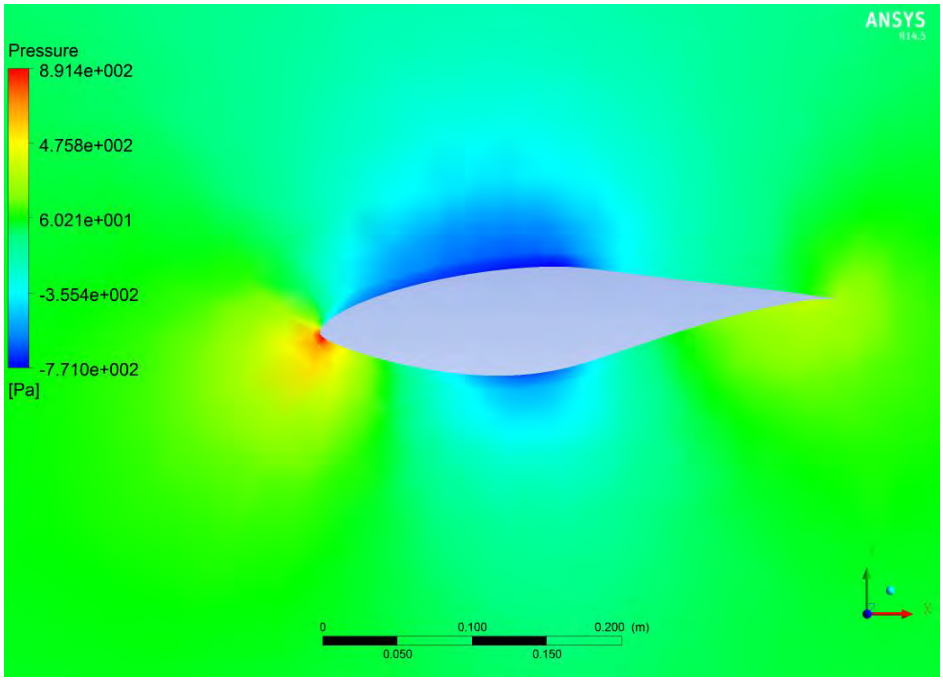

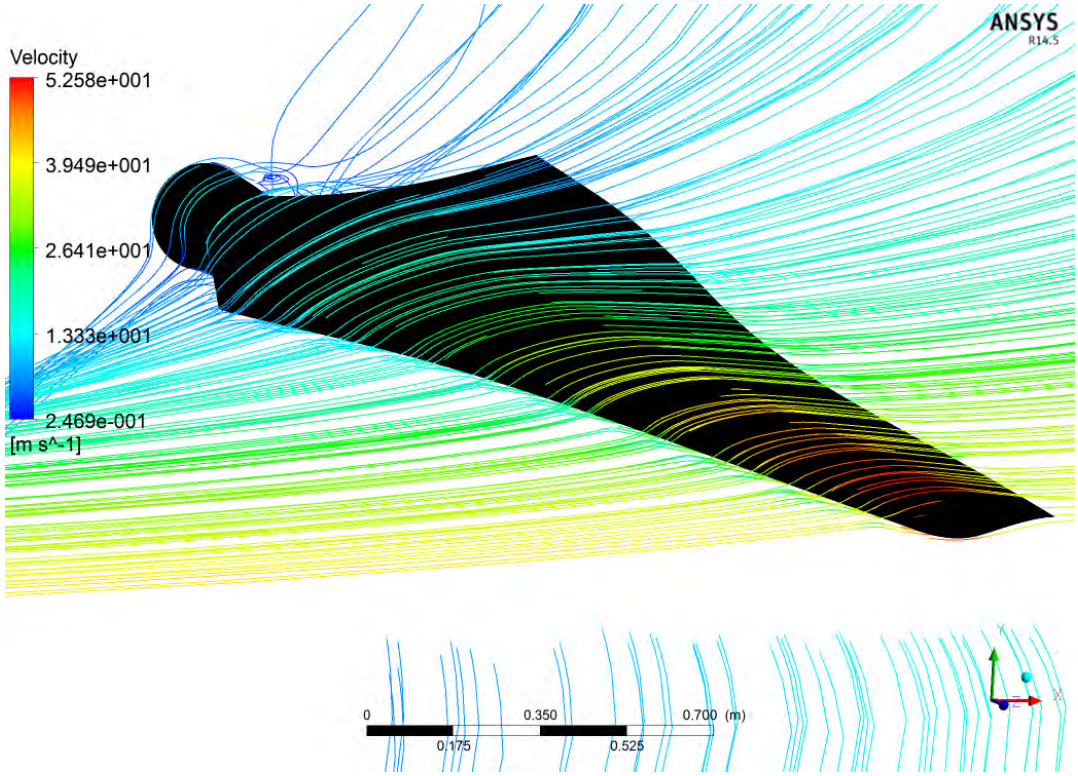

Figure 101: Velocity Streamlines at 5m/s

Candidate 1 at 10 m/s

r/R	Pressure Contour
0.3	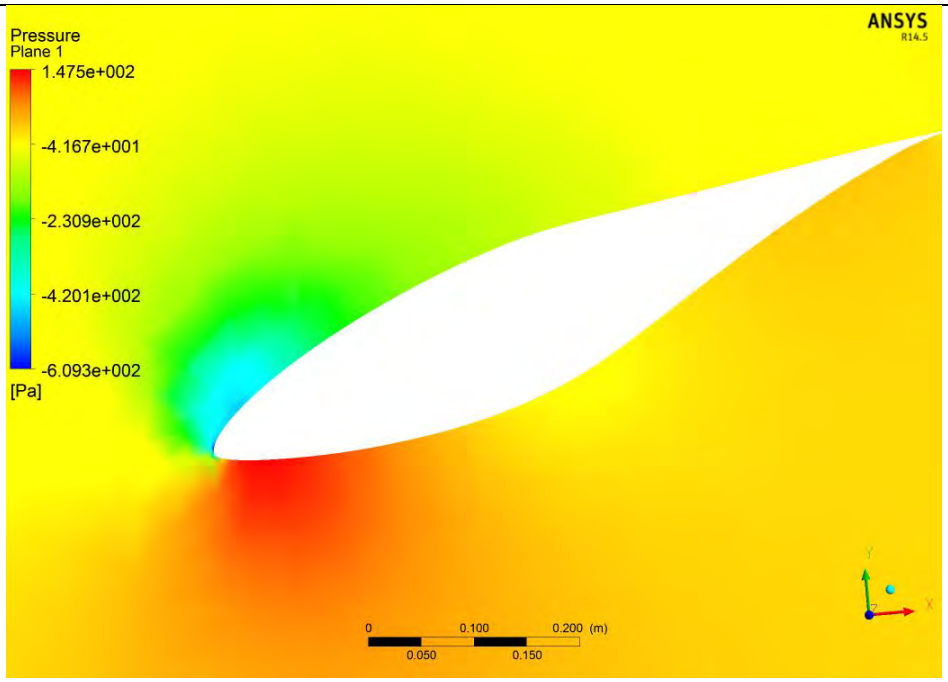
0.45	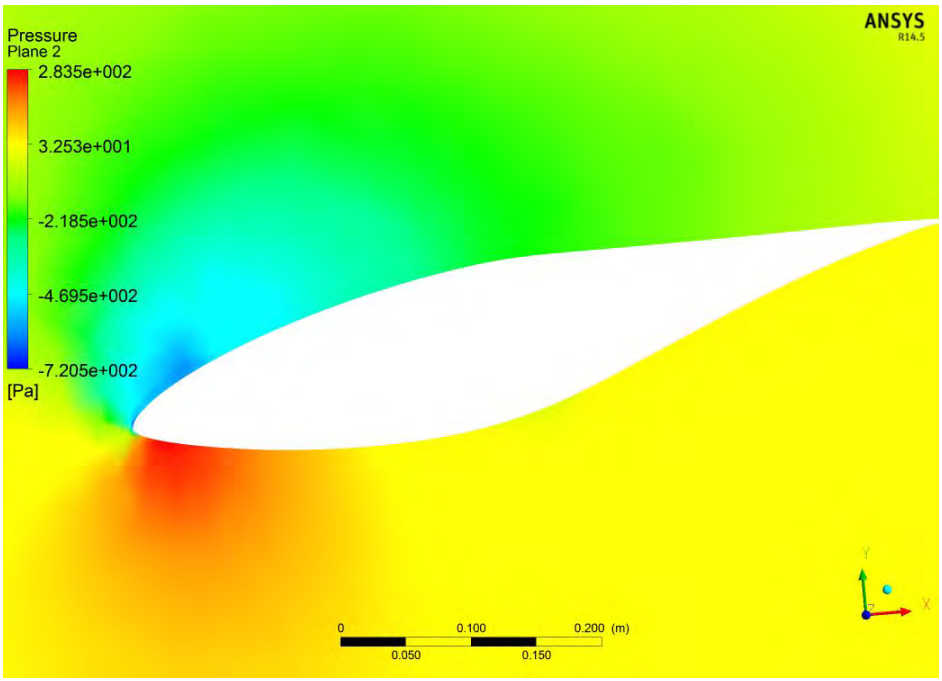

0.63

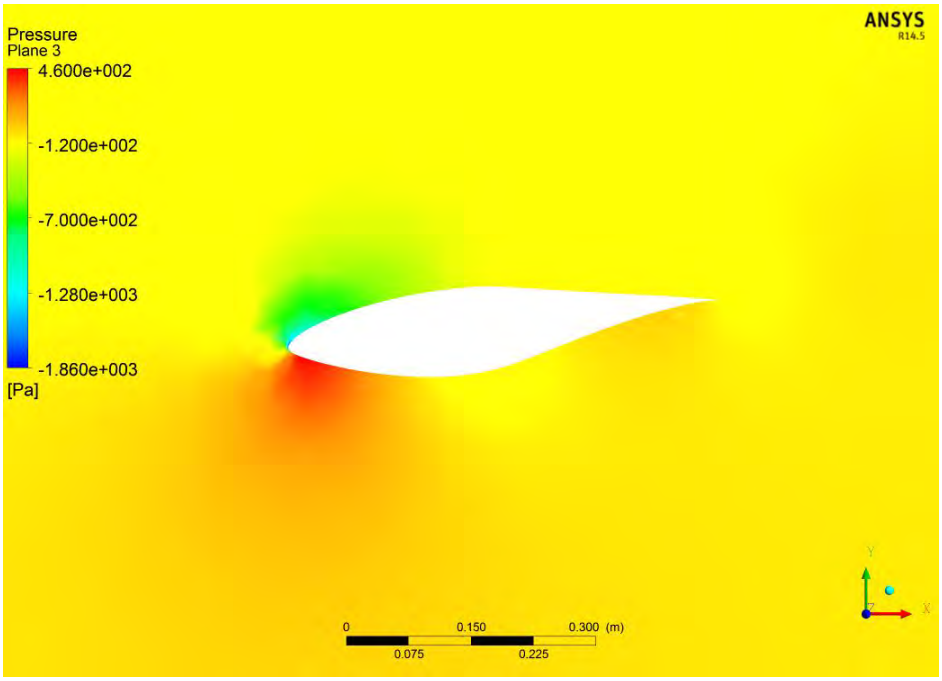
Pressure
Plane 3
4.600e+002
-1.200e+002
-7.000e+002
-1.280e+003
-1.860e+003
[Pa]
ANSYS
R14.5
0
0.150
0.300 (m)
0.075
0.225

0.8

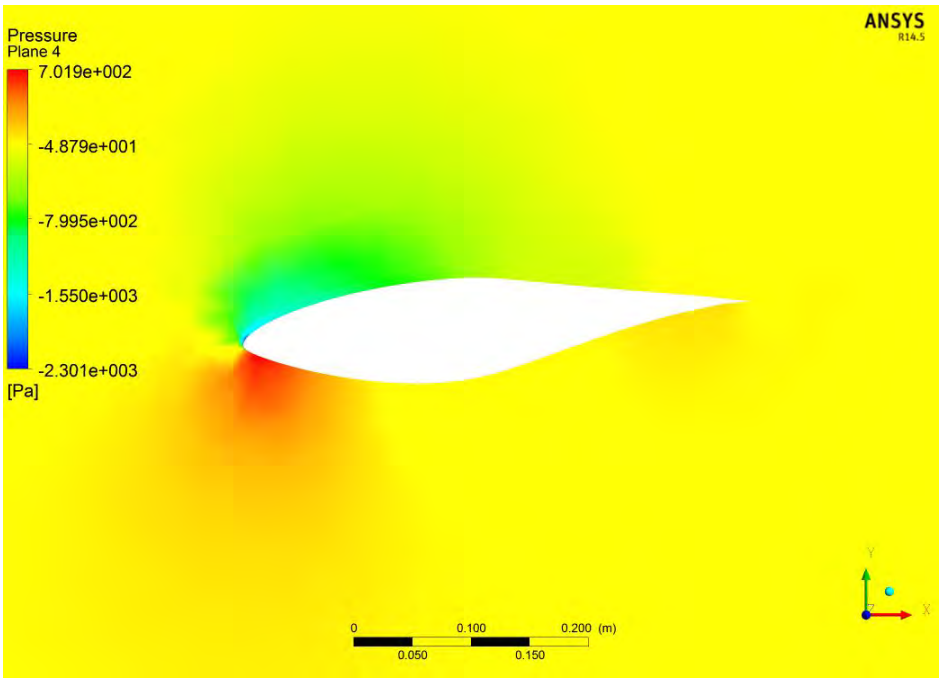
Pressure
Plane 4
7.019e+002
-4.879e+001
-7.995e+002
-1.550e+003
-2.301e+003
[Pa]
ANSYS
R14.5
0
0.100
0.200 (m)
0.050
0.150

0.95	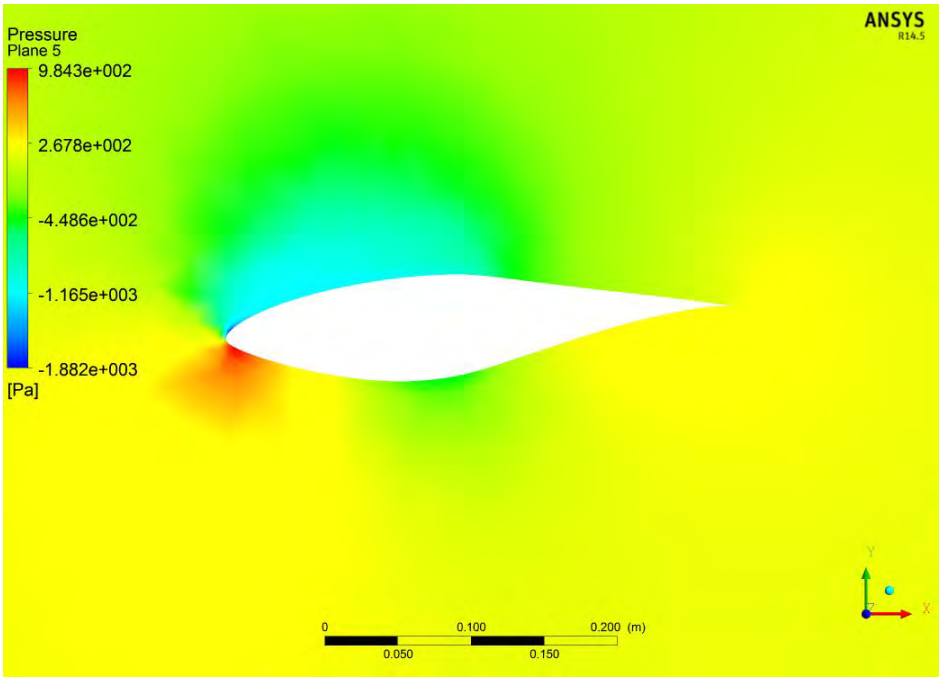

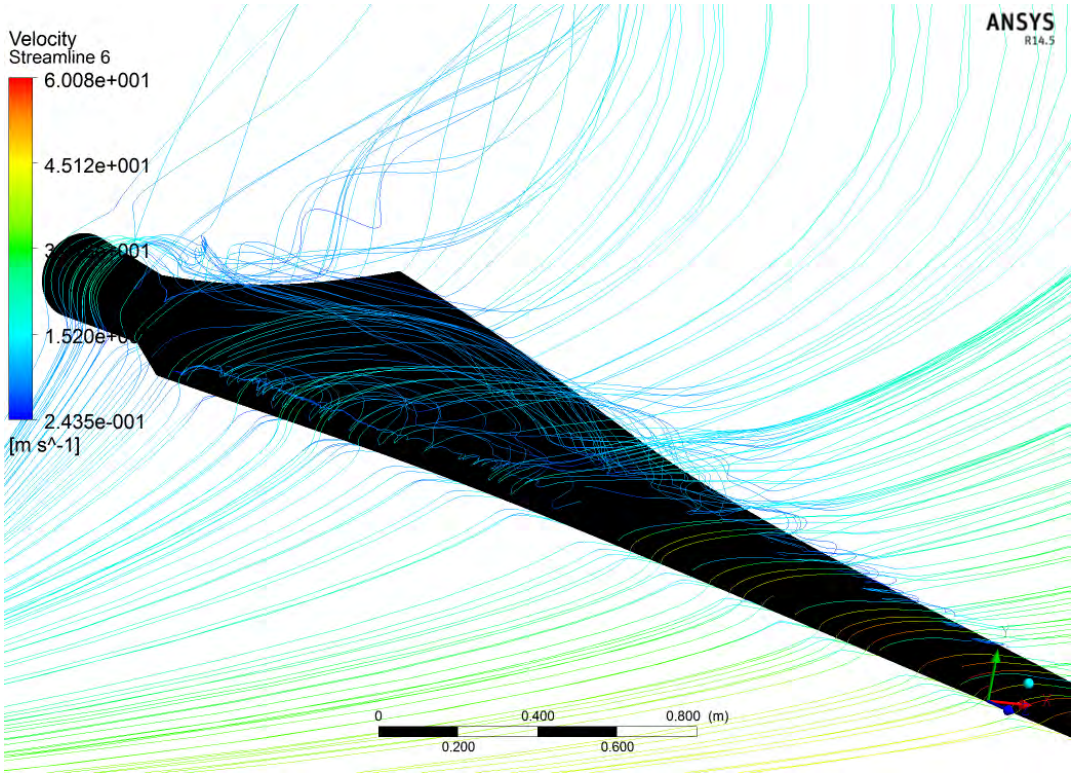

Figure 102: 3D Velocity Streamlines at 10 m/s

Candidate 1 at 13.1 m/s wind speed

r/R	Pressure Contour
0.3	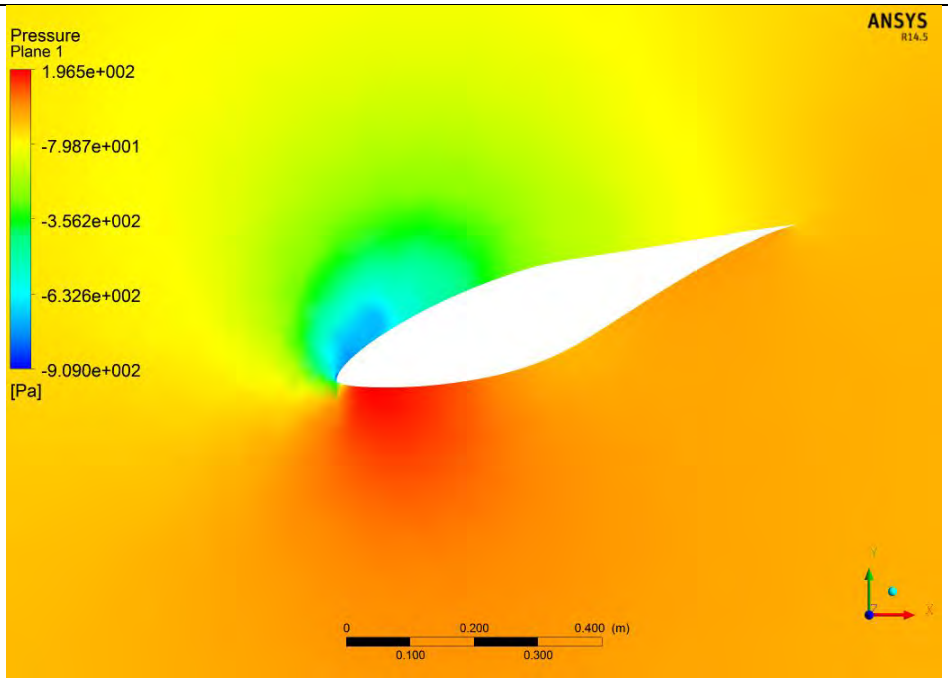
0.45	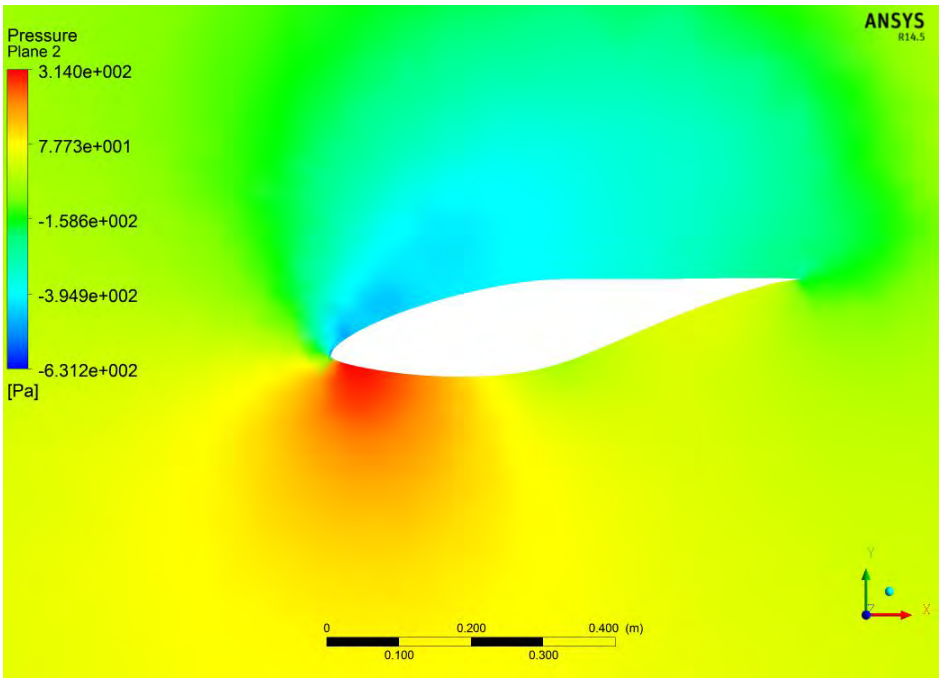

0.63

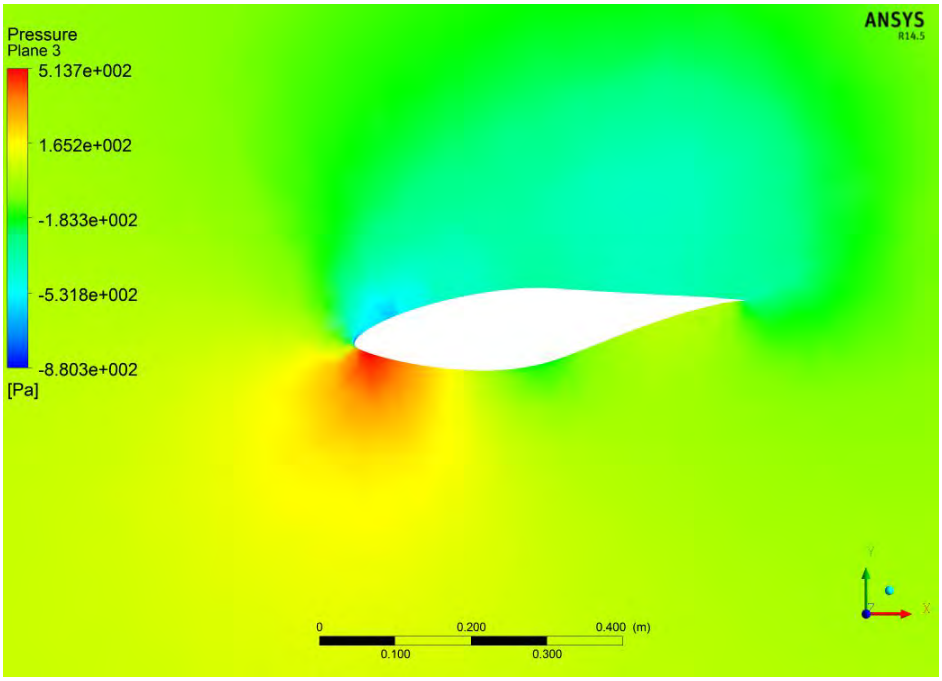
Pressure
Plane 3
5.137e+002
1.652e+002
-1.833e+002
-5.318e+002
-8.803e+002
[Pa]
ANSYS
R14.5
0
0.200
0.400 (m)
0.100
0.300

0.8

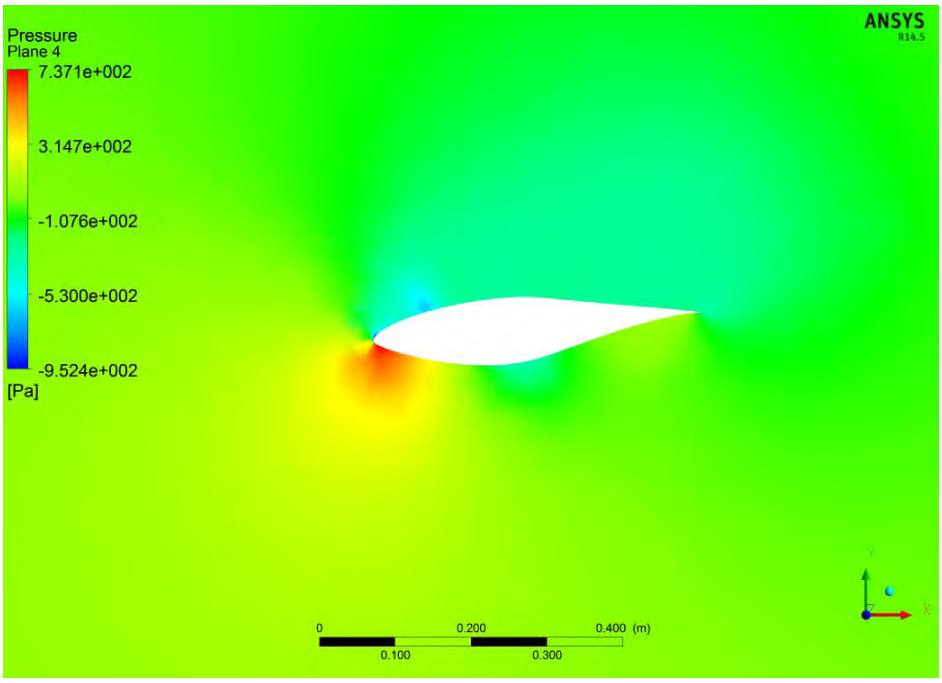
Pressure
Plane 4
7.371e+002
3.147e+002
-1.076e+002
-5.300e+002
-9.524e+002
[Pa]
ANSYS
R14.5
0
0.200
0.400 (m)
0.100
0.300

0.95	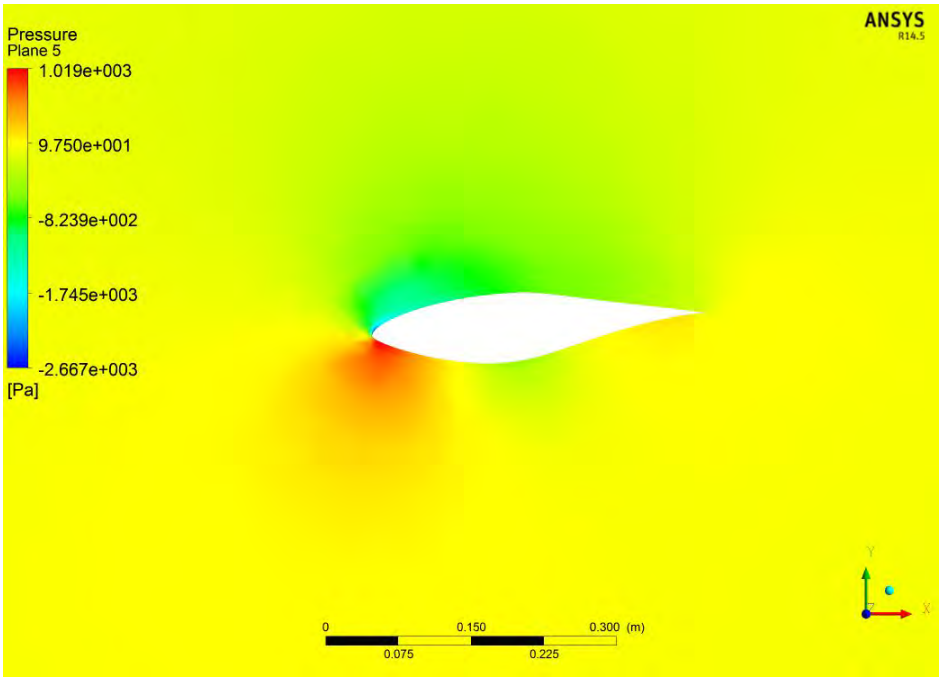

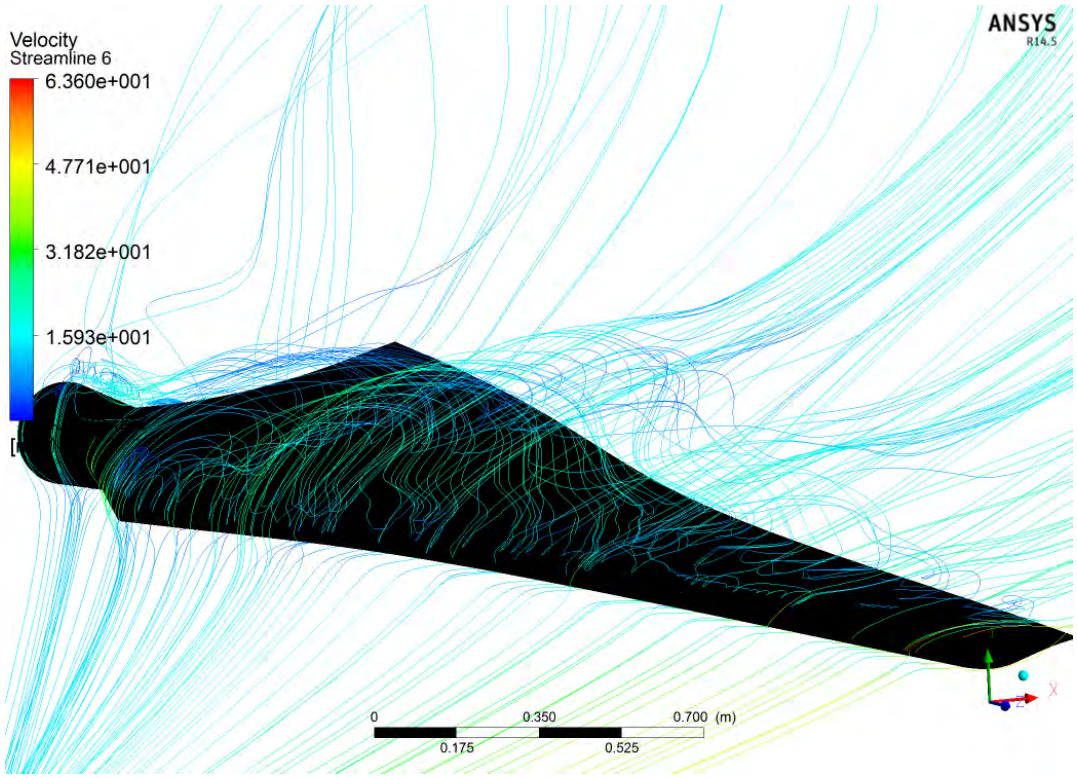

Figure 103: 3D Velocity Streamlines at 13.1 m/s

Reference

[1] INGRAM.G, "Wind Turbine Analysis Using Blade Element Momentum Theory".

[2] P. FUGLSANG and H. MADSEN, "Optimization Method for Wind Turbine Rotors," *Journal of Wind Engineering and Industrial Aerodynamics.*

[3] E. CHONG and S. ZAK, An Introduction to Optimization, Wiley Interscience Series, 2001.

[4] M. RAZVAN and F. POPESCU, "NREL VI Rotor Modeling and Simulation Using ANSYS FLUENT 12.1," *Scientific Journal - Mathematical Modelling in Civil Engineering ,* vol. V, p. 10, 2010.

[5] R. YANG and R.-n. LI, "Research of the Rotational Effects on the Aerodunamics Characteristics of Horizontal Axis Wind Turbine," *IEEE,* p. 4, 2009.

[6] M. M. YELMULE and E. R. A. VSJ, "CFD Predictions of NREL VI Rotor Experiments in NASA/AMES Wind Tunnel," *International Journal of Renewable Energy Research,* vol. 3, no. 2, 2013.

[7] R. VAN ROOIJ and E. ARENS, "Analysis of the Experimental and Computational FLow Characteristics with respect to the Augmented Lift Phenomenon caused by Blade Rotation," *Journal of Physics,* vol. 75, 2007.

[8] S. M. SALIM and S. CHEAH, "Wall y+ Strategy for Dealing with Wall-bounded

Turbulent Flows," *International MultiConference of Engineerns and Computer Scientists ,* vol. II, 2009.

[9] M. A. ELFARRA, N. SEZER-UZOL and I. S. AKMANDOR, "NREL VI Rotor Blade: Numerical Investigation and winglet design and optimization using CFD," *Wind Energy,* vol. 17, 2014.

[10] M.-C. HSU, I. AKKERMAN and Y. BAZILEVS, "Finite Element Simulation of Wind Turbine Aerodynamics: Validation Study using NREL VI Experiment," *Wind Energy,* vol. 17, 2014.

[11] F. R. MENTER, "Turbulence Modeling for Engineering Flows," ANSYS. Inc.

[12] S. SCHRECK, T. SANT and D. MICALLEF, "Rotational Augmentation Disparities in the MEXICO and UAE Phase VI Experiments," *National Renewable Energy Laboratory,* 2010.

[13] S. LARWOOD and M. ZUTECK, "Swept Wind Turbine Blade Aeroelastic Modeling for Loads and Dynamic Behavior," *Wind Power,* 2006.

[14] N. SEZER-UZOL and L. N. LONG, "3-D Time Accurate CFD Simulations of Wind Turbine Rotor Flow Fields," *AIAA,* 2006.

[15] A. M. Students, "Wind Turbine Blade Design Optimization," *AIAA*.

[16] M. JURECZKO, M. PAWLAK and A. MEZYK, "Optimization of Wind Turbine Blades," *Journal of Material Processing Technology,* 2005.

[17] G. KENWAY and J. R. MARTINS, "Aerostructural Shape Optimization of Wind Turbine Blades Considering Site Specific Winds," *AIAA/ ISSMO Multidisciplinary Analysis and Optimization Conference,* 2008.

[18] D. HARTWANGER and A. HORVAT, "3D Modelling of a Wind Turbine using CFD," *NAFEMS,* 2008.

[19] P. MORIARTY and A. HANSEN, "Aerodyn Theroy Manual," National Renewable Energy Laboratory.

[20] V. Capasso and J. Periaux, Multidisciplinary Methods for Analysis Optimization and Control of Complex Systems, Springer.